Western Graduate&PostdoctoralStudies

Western University
Scholarship@Western

Electronic Thesis and Dissertation Repository

11-25-2014 12:00 AM

Acquisition and Reconstruction Techniques for Fat Quantification Using Magnetic Resonance Imaging

Abraam S. Soliman
The University of Western Ontario

Supervisor
Charles A. McKenzie
The University of Western Ontario Joint Supervisor
Terry M. Peters
The University of Western Ontario

Graduate Program in Biomedical Engineering
A thesis submitted in partial fulfillment of the requirements for the degree in Doctor of Philosophy
© Abraam S. Soliman 2014

Follow this and additional works at: https://ir.lib.uwo.ca/etd

Part of the Biophysics Commons, and the Medical Biophysics Commons

Recommended Citation

Soliman, Abraam S., "Acquisition and Reconstruction Techniques for Fat Quantification Using Magnetic Resonance Imaging" (2014). *Electronic Thesis and Dissertation Repository*. 2526.
https://ir.lib.uwo.ca/etd/2526

This Dissertation/Thesis is brought to you for free and open access by Scholarship@Western. It has been accepted for inclusion in Electronic Thesis and Dissertation Repository by an authorized administrator of Scholarship@Western. For more information, please contact wlswadmin@uwo.ca.

www.manaraa.com

ACQUISITION AND RECONSTRUCTION TECHNIQUES FOR FAT QUANTIFICATION USING MAGNETIC RESONANCE IMAGING

(Thesis format: Integrated Article)

by

Abraam S. Soliman

Graduate Program in Biomedical Engineering

A thesis submitted in partial fulfillment
of the requirement for the degree of
Doctor of Philosophy

The School of Graduate and Postdoctoral Studies
The University of Western Ontario
London, Ontario, Canada

© Abraam S. Soliman

2014

المنارة للاستشارات

www.manaraa.com

Abstract

Quantifying the tissue fat concentration is important for several diseases in various organs including liver, heart, skeletal muscle and kidney. Uniquely, MRI can separate the signal from water and fat *in-vivo*, rendering it the most suitable imaging modality for non-invasive fat quantification. Chemical-shift-encoded MRI is commonly used for quantitative fat measurement due to its unique ability to generate a separate image for water and fat. The tissue fat concentration can be consequently estimated from the two images. However, several confounding factors can hinder the water/fat separation process, leading to incorrect estimation of fat concentration.

The inhomogeneities of the main magnetic field represent the main obstacle to water/fat separation. Most existing techniques rely mainly on imposing spatial smoothness constraints to address this problem; however, these often fail to resolve large and abrupt variations in the magnetic field. A novel convex relaxation approach to water/fat separation is proposed. The technique is compared to existing methods, demonstrating its robustness to resolve abrupt magnetic field inhomogeneities.

Water/fat separation requires the acquisition of multiple images with different echo-times, which prolongs the acquisition time. Bipolar acquisitions can efficiently acquire the required data in shorter time. However, they induce phase errors that significantly distort the fat measurements. A new bipolar acquisition strategy that overcomes the phase errors and provides accurate fat measurements is proposed. The technique is compared to the current clinical sequence, demonstrating its efficiency in phantoms and *in-vivo* experiments. The proposed acquisition technique is also applied on animal models to achieve higher spatial resolution than the current sequence.

المنارة للاستشارات
www.manaraa.com

In conclusion, this dissertation describes a complete framework for accurate and precise MRI fat quantification. Novel acquisitions and reconstruction techniques that address the current challenges for fat quantification are proposed.

Keywords: Chemical-shift imaging, water/fat imaging, fat quantification, field map estimation, bipolar acquisition, continuous max-flow.

المنارة للاستشارات
www.manaraa.com

Co-Authorship Statement

Chapter 2 is adapted from a published work in Springer Lecture Notes in Computer Sciences (LNCS) of Medical Image Computing and Computer-Assisted Intervention (MICCAI) 2012, entitled: "*A Convex Relaxation Approach to Fat/Water Separation with Minimum Label Description*" by Abraam Soliman, Jing Yuan, James White, Terry Peters, and Charles McKenzie. I provided the initial idea for the work and implemented the main framework of the technique, implemented the energy function, modified the max-flow algorithm (first stage of a two-stage method) and implemented the second stage. I also performed all the necessary testing, validation and writing of the manuscript. Jing Yuan provided the core implementation of the continuous max-flow algorithm, provided assistance in the problem formulation, and assisted in the revision of the manuscript. James White provided clinical guidance in cardiac imaging and in the validation of the results, and assisted in the revision of the manuscript. Terry Peters provided mentorship and guidance of the work, and assisted in the revision of the manuscript. Charles McKenzie provided advice in the experimental validation, data acquisition, assisted in the revision of the manuscript and mentored the work. *In-vivo* data acquisition was done by Trevor Szekeres at Robarts Research Institute, London, ON.

Chapter 3 is adapted from a published work in Magnetic Resonance in Medicine 2014, entitled: "*Max-IDEAL: a max-flow based approach for IDEAL water/fat separation.*" by Abraam Soliman, Jing Yuan, Karl Vigen, James White, Terry Peters, and Charles McKenzie. I provided the initial idea for the work and implemented the main framework of the technique, developed the energy function, modified the max-flow algorithm and implemented the second stage of the technique. I also performed all the necessary testing, validation and writing of the manuscript. Jing Yuan provided the core implementation of the continuous max-flow algorithm and assisted in writing the Theory section of the manuscript. Karl Vigen provided the cardiac IDEAL pulse sequence. James White provided clinical guidance in the

المنارة للاستشارات
www.manaraa.com

validation of the results. Terry Peters provided mentorship and guidance of the work, and assisted in the preparation of the manuscript. Charles McKenzie provided advice in the experimental validation, data acquisition, assisted in the revision of the manuscript and mentored the work.

Chapter 4 is adapted from an article completed for submission to Magnetic Resonance in Medicine, entitled: "*Fat quantification Using an Interleaved Bipolar Acquisition*" by Abraam Soliman, Curtis Wiens, Trevor Wade, Terry Peters and Charles McKenzie. Charles McKenzie and I provided the idea of the phase-corrected acquisition/reconstruction strategy. I was responsible of the main implementation of the MRI pulse sequence and the implementation of the reconstruction framework. I also performed the data acquisition, sequence testing, experimental validations, analysis of phantoms and *in-vivo* results. Curtis Wiens assisted in the pulse sequence programming, provided the implementation for the parallel imaging reconstruction and assisted in the revision of the manuscript. Trevor Wade provided guidance in pulse sequence programming, and assisted in the analysis of the data and in the revision of the manuscript. Terry Peters provided guidance and assistance in the revision of the manuscript. Charles McKenzie mentored the work, provided guidance in data acquisition and analysis, and assisted in the revision of the manuscript. *In-vivo* data acquisition was done by Trevor Szekeres at the Robarts Research Institute, London, ON.

Chapter 5 is adapted from an article in preparation to be submitted to the Journal of Magnetic Resonance Imaging, entitled: "*An Efficient Chemical-shift Encoded Acquisition for in-vivo Applications*" by Abraam Soliman, Lanette Friesen-Waldner, Kevin Sinclair, Timothy Regnault, Terry Peters and Charles McKenzie. I performed the data acquisition and reconstruction, experimental validations, data analysis and the writing of the manuscript. Lanette Friesen-Waldner, Kevin Sinclair, and Timothy Regnault assisted in the preparation and the handling of the animals. Terry Peters provided mentorship of the work. Charles McKenzie provided guidance in the design of experiments, data analysis, assisted in the revision of the manuscript and mentored the work.

المنارة للاستشارات
www.manaraa.com

Dedicated to

my Mother, Father and Brother

المنارة للاستشارات
www.manaraa.com

Acknowledgments

It was a four years' journey that would not have been completed without the help and support of many people, to whom I will always be grateful. I consider myself very fortunate to work with Dr. Charles McKenzie. Your expertise and knowledge have been invaluable throughout my PhD course; there is always something new to learn from you. Thank you for giving me this opportunity, for your help, guidance, patience and support. I am also so grateful to my co-supervisor Dr. Terry Peters for his guidance, support and encouragement since my first day here, without which I would not have accomplished my goal.

I would like to thank many people who helped me along the way: Dr. James White for the guidance and expertise that he provided in cardiac imaging, Dr. Jing Yuan for his assistance in image processing, Dr. Curtis Wiens, for helping in EPIC programming, image reconstruction and for adding much fun to the after-hours work, Dr. Lanette Friesen-Waldner for assistance in animal experiments and for sharing her unlimited source of idiomatic expressions and proverbs, and Dr. Trevor Wade for helpful discussions and for having the guts to teach everyone the EPIC course… twice! Also I would like to thank Ann Shimmakawa and Kang Wang from GE for their assistance in troubleshooting the IDEAL sequence and reconstruction.

Thanks to all the members of the McKenzie group who made the lab an enjoyable work place and have shared memorable time together: Curtis, Lanette, Trevor, Kevin, Jackie, Yifan, Colin, Bryan and Samantha. Thanks to the amazing members of Dr. Peters' group for everything. I am also thankful to many friends for their support along the way: Maged, Brandon, Cyrus, Ismail, Mariam, Punithan and Max.

I cannot thank enough my mother, father and brother, for all for their unconditional love, support, encouragement and sacrifices throughout all these years, without which I would not be here, celebrating (soon) this achievement.

المنارة للاستشارات
www.manaraa.com

Contents

Abstract ..... **ii**

Co-Authorship Statement ..... **iv**

Acknowledgments ..... **vii**

List of Figures ..... **xiii**

List of Abbreviations ..... **xix**

1 Introduction **1**

1.1 Motivation 1

1.2 Magnetic Resonance Imaging 3

1.2.1 Principles of Magnetic Resonance Imaging 3

1.2.2 Spatial Encoding 5

1.2.3 Gradient-echo sequences 7

1.3 Water/Fat Imaging 9

1.3.1 Chemical-Shift-Encoded Water/Fat Imaging 9

1.3.2 Two-Point Dixon 11

1.3.3 Three-Point Dixon 13

1.3.4 IDEAL 14

المنارة للاستشارات

www.manaraa.com

1.3.5 Characterization of Noise Performance 16
1.4 Quantitative Fat Imaging 17
1.4.1 Multi-peak Fat Spectrum 17
1.4.2 Effect of T_2^* Relaxation 19
1.4.3 T_1-related Bias 21
1.4.4 Eddy Currents 22
1.4.5 Noise-related Bias 23
1.4.6 Temperature-related Bias 23
1.5 Parallel Imaging 24
1.6 Network Optimization Problems 26
1.6.1 Terminology 26
1.6.2 Min-cut / Max-flow Problem 27
1.6.3 Continuous Max-flow 28
1.5 Thesis Outline 30
References 32

2 A Convex Relaxation Model to Water-Fat Separation With Minimum Label Description 42
2.1 Introduction 42
2.2 Theory and Methodology 46
2.2.1 Signal Equation 46
2.2.2 The Potts Model 48
2.2.3 Minimum Description Length (MDL)-Based Potts Model 49
2.2.4 A Fast Continuous Max-Flow Approach to MDL-based Potts Model 49
2.3 Experiments 50
2.4 Discussion 54
Acknowledgments 55
References 56

المنارة للاستشارات
www.manaraa.com

3 Max-IDEAL: A Max-Flow Based Approach to IDEAL Water/Fat Separation 59

3.1 Preface 59

3.2 Introduction 61

3.3 Theory 63

3.3.1 Signal Equation 64

3.3.2 Inclusion of T_2^* Effect 68

3.3.3 Adaptive Spatial Filtering (ASF) 69

3.3.4 The Potts Labeling Model 72

3.4 Methods 73

3.4.1 MR Acquisition 73

3.4.2 Pre-processing: ASF 74

3.4.3 STAGE I: A Continuous Max-flow Approach to Potts Model 74

3.4.4 STAGE II: T_2^*-IDEAL Water/Fat Separation 75

3.5 Results 76

3.6 Discussion 85

3.7 Conclusion 92

Acknowledgments 93

References 94

4 Fat Quantification With an Interleaved Bipolar Acquisition 97

4.1 Introduction 97

4.2 Theory 100

4.3 Methods 105

4.4 Results 108

4.5 Discussion 113

4.6 Conclusion 114

Acknowledgments 115

References 116

المنارة للاستشارات

www.manaraa.com

5 An Efficient Chemical-shift Encoded Acquisition for in-vivo Applications 120
5.1 Introduction 120
5.2 Methods and Experiments 122
5.2.1 MRI Acquisition 122
5.2.2 Water/Fat Reconstruction 125
5.3 Results 126
5.4 Discussion 132
5.5 Conclusion 134
References 135

6 Conclusion and Future Work 141
6.1 Summary 141
6.1.1 A Convex Relaxation Approach to Water/Fat Separation with Minimum Label Description (Chapter 2) 142
6.1.2 Max-IDEAL: A Max-Flow Based Approach to IDEAL Water/Fat Separation (Chapter 3) 143
6.1.3 Fat Quantification Using an Interleaved Bipolar Acquisition (Chapter 4) 144
6.1.4 An Efficient Chemical-shift Encoded Acquisition for in-vivo Applications (Chapter 5) 144
6.2 Future Directions 145
6.2.1 Combining Multiple Smoothness Constraints To Improve The Robustness of The Field Map Estimation 145
6.2.2 Integrating Prior Knowledge of Anatomy into Max-IDEAL 147
6.2.3 A Standardized Accuracy Metric of Field Map 148
6.2.4 Reduce The Vulnerability of the Interleaved Bipolar Sequence to Motion Artifacts 149
6.2.5 A Standardized Accuracy Metric of Field Map 149

المنارة للاستشارات
www.manaraa.com

6.3 Conclusion 150
References 151

Ethics Approval 155

Letters of Permissions 157

Curriculum Vitae 168

المنارة للاستشارات
www.manaraa.com

List of Figures

Figure 1.1: A generic SPGR pulse sequence diagram. Here an RF pulse with α flip angle is applied. GSS is the slice-encode gradient; GPE is the phase-encode gradient and GFE is the frequency-encode gradient. TE is the echo-time of the acquired signal; TR is the repetition time. Spoilers are indicated at the end of the TR 8

Figure 1.2: A representative frequency spectrum of the MRI signal, showing two main peaks for water and fat, separated by 3.5 ppm 10

Figure 1.3: The two-point Dixon method reconstructs water and fat images by adding and subtracting in-phase and out-of-phase images, respectively 12

Figure 1.4: Illustration of the IDEAL water/fat separation process 15

Figure 1.5: Frequency spectrum of knee subcutaneous fat showing 6 peaks, with the main peak located at ~420 Hz (3.5 ppm) – Figure adapted from [50] 18

Figure 1.6: Illustration of the 6-point T2*-IDEAL proposed by Yu et al. [50, 54] 20

المنارة للاستشارات
www.manaraa.com

Figure 1.7: Three readout gradients are applied in one TR to acquire 3 echoes 22

Figure 1.8: (a) A knee image obtained from the Fourier transform of a fully-sampled k-space. (b) Undersampling the k-space results in an aliased image. (c) The image is reconstructed from the undersmapled k-space using Parallel Imaging reconstruction 25

Figure 1.9: Left: A discrete flow network problem with a min-cut solution. Right: A Continuous flow network problem. 28

Figure 2.1: Water/fat swaps appearing in field map (top), water (left) and fat components (right) 44

Figure 2.2: Left column: axial abdominal slice, Right column 4-chambers cardiac view. Top to bottom: the coarse estimate of field map from the max-flow stage, final field map after the second stage, water and fat components 52

Figure 2.3: Comparison between our approach (left column) and the region-growing method (right column) on a short-axis cardiac image. Yellow arrows indicate the locations of water/fat swaps that have clearly avoided by our method 53

Figure 3.1: (a) A point is selected on a 2D axial cardiac image. (b) Neglecting the effect of T2* decay (i.e. R2* = 0), the variation of the signal residuals $\Gamma v(\varphi)$. (c) By assigning φv to its optimal value (-41.5 Hz) and the aliased value (-486 Hz), the variation of $\Gamma v(R2*)$ is drawn with different R2* values 67

Figure 3.2: (a) Field map, η, obtained from Eq.5 before applying the adaptive spatial filter (ASF); (b) the output of ASF after the first iteration, $F(1)$, from Eq.6; (c) A thresholded version of (b), producing a binary mask for the vulnerable

المنارة للاستشارات
www.manaraa.com

locations of water/fat swaps; (d) the final output of the ASF, showing less water/fat swaps than (a) 71

Figure 3.3: Fat water separation in a 4-chamber cardiac slice acquired from a healthy volunteer. (a) Output of the labeling stage showing a coarse estimation of the field map, (b) Final field map after the second stage, (c) Water component, (d) Fat component 77

Figure 3.4: Reconstructed data from a 2-chamber cardiac. (a) The labeled field map from the first stage, (b) final field map, (c) fat fraction map and (d) R2* map 78

Figure 3.5: Reconstructed data from an axial abdominal slice. (a) The labeled field map from the first stage, (b) final field map, (c) fat fraction map and (d) R2* map 79

Figure 3.6: The reconstruction of the failure case using Max-IDEAL (a), the graph-cut method (b) and the FLAME technique (c). Left to right: field map, water, fat and fat fraction map 80

Figure 3.7: Reconstruction of a selected slice from a case provided by the ISMRM 2012 challenge with the labeling approach in [15] (a) and the proposed method (b) 81

Figure 3.8: Comparisons between Max-IDEAL (a, c) and the graph-cut method (b, d) using two cases from the ISMRM 2012 challenge. The proposed approach can resolve strong B0 variations while the spatial smoothness constraint employed in graph-cut fails. Left to right: initial field map (a and c only), final field map, water, fat and fat fraction map 83

المنارة للاستشارات
www.manaraa.com

Figure 3.9: A comparison with the FLAME technique on a short-axis cardiac slice. (a) Results from Max-IDEAL; (b) results of FLAME method. Top to bottom: field map, water, fat and fat fraction map 84

Figure 3.10: Reconstruction of a case from ISMRM 2012 challenge with (a) T2* applied in both stages of the approach, and (b) T2* incorporated only in the second stage (T2*-IDEAL). The reconstruction fails in case T2* decay is not considered in the labeling stage 87

Figure 3.11: An example of the boundary artifact appearing in an axial abdominal slice. This artifact is induced around the bowels where very low signal is received..... 89

Figure 3.12: The effect of applying different smoothness levels on the reconstruction of a case from ISMRM 2012 challenge: (a) β=0.2 was insufficient to remove water/fat swaps; successful reconstruction can be achieved in (b) β = 0.5 and (c) β = 2; (d) Oversmoothed initial field map with β = 4 causes water/fat artifacts as noted by the arrow. The ASF was not applied in this reconstruction in order to solely examine the effect of the smoothness parameter 91

Figure 4.1: (a) A representative diagram of the unipolar sequence. All echoes are acquired with the same readout gradient polarity (positive). Here all echoes are acquired in a single TR (single shot). (b) A representative diagram of the conventional bipolar sequence. Odd echoes are acquired with positive polarities while even echoes have negative polarities. The bipolar acquisition in (b) necessitates employing post-processing phase and magnitude correction algorithms before water/fat separation 103

Figure 4.2: The proposed interleaved bipolar acquisition: Two bipolar schemes are employed, where scheme 1 has opposite polarity to scheme 2. The odd lines

المنارة للاستشارات
www.manaraa.com

are acquired with scheme 1 while the even lines are acquired with scheme 2. The centre lines are fully-acquired with both schemes 104

Figure 4.3: The reconstruction pipeline for the interleaved bipolar acquisition. The centre of k-space acquired with a positive polarity is used in the self-calibrated parallel imaging reconstruction of the positive lines, and vice-versa for the negative lines 105

Figure 4.4: Fat fraction images (ranging from 0% to 5%) of a pure-water phantom from unipolar (a) and interleaved bipolar (b) axial acquisitions. Phase errors from the readout gradient cause fat fraction bias in the unipolar acquisition, while the errors were negligible in the interleaved bipolar results 109

Figure 4.5: Results from a coronal acquisition of the phantom set. (a) Fat fraction map of the phantom set with the locations of the 5 vials of different fat fractions indicated. (b) Differences between the true and the measured values from the two sequences, demonstrating accurate fat quantification obtained using the interleaved bipolar compared to the unipolar sequence 109

Figure 4.6: Water and fat images of a volunteer's knee were obtained with the interleaved bipolar (upper row) and the unipolar sequence (lower row). SNR efficiency maps in (b) and (d) are scaled from [0, 1]. The 2 ROIs in (e) were used for the fat quantification results reported in the text, and demonstrated that accurate fat fractions were obtained with the 2 sequences. However, the SNR efficiency maps (b and d) show that higher SNR efficiency was obtained with the bipolar sequence 110

Figure 4.7: (a) Water, (b) fat and (c) fat fraction maps of a whole-liver acquisition from the interleaved bipolar (upper row) and the unipolar (lower row)

المنارة للاستشارات
www.manaraa.com

sequences, respectively. The ROIs selected in the liver in (c) were used for the fat quantification results reported in the text, and demonstrated that accurate fat fraction was obtained with the interleaved bipolar sequence 111

Figure 4.8: SNR maps of the 2nd echo (a), the water (b) and the fat (c) images from the interleaved bipolar (upper row) and the unipolar (lower row) sequences, respectively. Higher SNR was obtained in all the images with the proposed bipolar sequence 112

Figure 5.1: The water component (upper row) and its corresponding SNR efficiency map (lower row) from the four sequences. The interleaved bipolar sequences (B and D) demonstrate higher SNR efficiency compared to the corresponding unipolar sequences (A and C) 127

Figure 5.2: The fat component (upper row) and its corresponding SNR efficiency map (lower row) from the four sequences. The interleaved bipolar sequences (B and D) demonstrate higher SNR efficiency compared to the corresponding unipolar sequences (A and C) 128

Figure 5.3: The fat fraction images from the four sequences. (A) Unipolar, (B) Interleaved bipolar, (C) Accelerated unipolar, (D) High resolution interleaved bipolar. Accurate fat fraction was obtained with the interleaved bipolar sequences compared to their corresponding unipolar sequences 129

Figure 5.4: Fat fraction, water and fat images from 2 different slices are shown. For each example, the top image is an axial reformat of a fat fraction map from the unipolar sequence. A zoomed view of the region highlighted inside the red box is shown. The arrows indicate the anatomical structures that were clearly identified in the high resolution interleaved bipolar images, while they are not clearly depicted in the unipolar results 131

المنارة للاستشارات
www.manaraa.com

List of Abbreviations

2D	Two dimensional
3D	Three dimensional
BW	Acquisition bandwidth
EPI	Echo-planar imaging
ETL	Echo-train length
FLAME	Fat-likelihood analysis for multi-echo signals
FOV	Field of view
FT	Fourier transform
GE	Gradient-echo sequence
GRAPPA	Generalized auto-calibrating partially parallel acquisitions
GPGPU	General-purpose computing on graphics processing unit
GPU	Graphics processing unit

المنارة للاستشارات
www.manaraa.com

Hz	Hertz
IDEAL	Iterative decomposition of water and fat with echo asymmetry and least-squares
MDL	Minimum description length
MRI	Magnetic resonance imaging
NEX	Number of excitations
NSA	Number of signal averages
R_2^*	Effective transverse relaxation time
RF	Radio frequency
ROI	Region of interest
SE	Spin-echo sequence
SENSE	Sensitivity encoding (parallel imaging reconstruction)
SNR	Signal to noise ratio
SPGR	Spoiled gradient-recalled echo
ΔTE	Inter-echo spacing
T	Tesla
T_1	Longitudinal relaxation time
TE	Echo-time
TR	Repetition Time

المنارة للاستشارات
www.manaraa.com

"A journey of a thousand miles begins with a single step"
- Laozi (Chinese philosopher)

Chapter 1

Introduction

1.1 Motivation

Fat is an important diagnostic marker in many clinical applications, including liver [1], cardiac [2, 3], musculoskeletal system [4, 5], kidney [6], bone marrow [7, 8], measurement of total body fat [9], quantifying visceral adipose tissue [10], as well as distinguishing between white and brown adipose tissue [11, 12]. In liver applications for example, non-alcoholic fatty liver disease (NAFLD), one of the most common chronic liver conditions, is characterized by fatty infiltration of the liver [13, 14], and quantification of fat is necessary in the diagnostic process. Fat signal is also a relevant diagnostic marker of cardiac diseases such as myocardial fatty infiltration [15], which is associated with sudden cardiac death [16], arrhythmogenic right ventricular dysplasia (ARVD) [17] and chronic myocardial infarction [18]. Additionally, interest in measuring the epicardial and intra-thoracic fat has markedly increased in the last decade [2, 19], with some studies suggesting

المنارة للاستشارات
www.manaraa.com

such fat deposits to be strongly correlated with the presence of coronary artery disease [20].

Among different medical imaging modalities, Magnetic Resonance Imaging (MRI) is well suited for fat quantification for its ability to separate the signals from water and fat in the human body. Uniquely, MRI can exploit small differences in the frequency of signals received from different chemical species to generate individual images of each species. Water and fat are the main sources of signal in MR images for most clinical applications. MRI can distinguish between water-based and fat-based tissues producing fat-suppressed (water-only) and water-suppressed (fat-only) images, which are commonly needed in clinical diagnosis.

Fat quantification is usually performed in terms of *fat fraction*, which is the ratio of the fat signal to the total signal from both water and fat. A typical example is the measurement of liver fat in NAFLD patients, where the fat fraction of healthy liver should not exceed 5% [13]. Therefore, accurate and precise fat measurement is required. Several confounding factors can bias the fat fraction measure and must be considered during signal acquisition and reconstruction. These factors include, but not limited to, the tissue-specific relaxation times (such as T_1 and T_2^*) and the inhomogeneities of the main magnetic field.

In this dissertation we will propose novel acquisition and reconstruction techniques to address the limitations that hinder the process of accurate and precise fat quantification. In this chapter we will revisit the basics of MRI and the gradient-echo pulse sequence. Then we will introduce water/fat imaging with all the confounding factors that need to be addressed for quantitative fat imaging. In the following chapters, will we first propose new techniques to estimate the magnetic field inhomogeneities, which are the main obstacle for successful water/fat separation. We will then propose a new acquisition strategy for water/fat imaging and then demonstrate it for *in-vivo* applications in animals and humans.

المنارة للاستشارات
www.manaraa.com

1.2 Magnetic Resonance Imaging

1.2.1 Principles of Magnetic Resonance Imaging

MRI relies on a strong magnetic field, B_0, which polarizes the nuclear spins in parallel and anti-parallel directions with respect to the main magnetic field. In the presence of an external magnetic field, the nuclear spins are polarized along the main field, leading to a net magnetization in the parallel direction. The precession frequency of the nuclear spins can be described by the Larmor equation as follows:

$$\omega_0 = \gamma B_0 \tag{1.1}$$

where ω_0 is called the Larmor frequency and γ is the gyromagnetic ratio of the nucleus being imaged. Most of the clinical MRI scans targets the Hydrogen proton ^{1}H as it is the dominant nucleus in the human body. For ^{1}H, γ is equal to 2.68x10^8 rad/s/Tesla. The commonly used value is $\bar{\gamma} = \gamma/(2\pi) = 42.6$ MHz/Tesla.

The net magnetization, M, resulting from the polarized spins cannot be detected as long as it aligns along the direction of the main magnetic field. Hence, an additional magnetic field, B_1, is applied to tilt the magnetization away from the B_0 direction. This process can be described through the Bloch equation as follows:

$$\frac{d\vec{M}}{dt} = \vec{M} \times \vec{B} \tag{1.2}$$

where

$$\vec{B} = \overrightarrow{B_0} + \overrightarrow{B_1} \tag{1.3}$$

Equation 1.2 is a simplified version of the Bloch equation where the relaxation times are neglected. The B_1 magnetic field is generated by a radiofrequency pulse (RF pulse) applied through a 'transmit' coil tuned at the Larmor frequency. In equilibrium, M is aligned with B_0 along the longitudinal ($\hat{z}$) direction. As of Equation 1.2, once the RF pulse is applied along $\hat{x}$ or $\hat{y}$ direction, the magnetization vector M is tipped with an angle α away from the longitudinal axis towards the transverse

المنارة للاستشارات
www.manaraa.com

plan (x-y plan). The tipping (or flip) angle is determined by the magnitude of the RF pulse, B_1, and its duration τ, such that:

$$\alpha = \gamma \int_0^{\tau} B_1(t) \tag{1.4}$$

Following the RF excitation both the longitudinal and transverse components of the magnetization start to relax via two mechanisms: First the longitudinal relaxation described by the time constant T_1, where the magnetization starts to relax back to its equilibrium state along the $\hat{z}$ direction. This is called the spin-lattice relaxation as it results from the interaction between the spins and the surrounding lattice. The second relaxation process is a transverse relaxation resulting from the interactions between spins, hence called the spin-spin relaxation. It results from the 'dephasing' of the spins and is governed by a time constant T_2. The two relaxation processes can be described through the Bloch equation:

$$\frac{d\vec{M}}{dt} = \vec{M} \times \vec{B} - \frac{M_x\,\hat{x} + M_y\,\hat{y}}{T_2} - \frac{(M_z - M_0)\,\hat{z}}{T_1} \tag{1.5}$$

Shortly after the RF excitation, the signal is sampled at a time 'TE' (or echo time) and detected through a 'receiver' coil. The detected signal is proportional to the magnitude of the transverse component of the magnetization, M_{xy}, and can be derived from the Bloch equation above (Equation 1.5). For example, if a pulse with $\pi/2$ flip angle is applied, the initial magnetization M_{init} will be fully tipped to the transverse plan. Ideally, immediately after the RF pulse at time $t = 0$, the magnetization vector $M_z(0) = 0$ and $M_{xy} = M_{init}$. The magnetization vectors at time t can be then derived from Equation 1.5, resulting in the following components:

$$M_z(t) = M_{init}\left(1 - e^{-t/T_1}\right) \tag{1.6}$$

$$M_{xy}(t) = M_{init}\,.\,e^{-i\omega_0 t}.\,e^{-t/T_2} \tag{1.7}$$

المنارة للاستشارات
www.manaraa.com

Hence the magnitude of the detected signal at time 'TE' will be proportional to $M_{init}.e^{-TE/T_2}$. If we started from the equilibrium state, then $M_{init} = M_0$. The received signal is therefore proportional to the bulk spin density, ρ, in the excited volume.

1.2.2 Spatial Encoding

So far we have introduced two sources of magnetic fields, the main magnetic field, B_0, and the RF pulse. In order to 'encode' the spatial position of received signal, additional magnetic fields, called gradients, are employed. A gradient is a linearly varying magnetic field added to the static field to distinguish the spins along a certain direction. For example in the x-direction it is given by:

$$B(x,t) = B_0 + x\, G_x(t) \tag{1.8}$$

where G_x is a constant gradient in the x-direction. The precession frequency will therefore vary along the x-diretion. Demodulating the Larmor precession, the phase accrual occurring due to the applied gradient is given by:

$$\varphi_x(x,t) = -\gamma x \int_0^t G_x(t')\, dt' \tag{1.9}$$

Similarly, a gradient is added in the y-direction, also causing an accumulation of phase along this direction. For a 2D acquisition, the received signal is now the product of the excited spin density with the gradients-induced phase terms along the two directions:

$$S(x,y) \propto \iint \rho(x,y) e^{-i\left(\varphi_x(x,t) + \varphi_y(y,t)\right)} dx\, dy \tag{1.10}$$

Defining k_x and k_y as the spatial frequencies in the x- and y- directions respectively, Equation 1.10 can be written as follows:

$$S(k_x,k_y) \propto \iint \rho(x,y) e^{-i2\pi\,(k_x\,x + k_y\,y)} dx\, dy \tag{1.11}$$

المنارة للاستشارات
www.manaraa.com

where

$$k_x = \frac{\gamma}{2\pi}\int_0^t G_x(t')\,dt' \tag{1.12}$$

$$k_y = \frac{\gamma}{2\pi}\int_0^t G_y(t')\,dt' \tag{1.13}$$

Neglecting the relaxation terms, Equation 1.11 is the form of a 2D Fourier transform (FT) of the spin density $\rho(x, y)$. Hence, an inverse 2D FT of the encoded signal will be a representation of the distribution of the underlying spin density, i.e. $\rho(x, y) = FT^{-1}[S(k_x, k_y)]$.

Equation 1.11 shows that MRI spatial encoding is achieved in terms of k_x and k_y, i.e. the signal data is a representation of the spatial frequencies of the spin density, and is therefore called k-space. The k_x direction is called the frequency encode or the readout direction, while the k_y is called the phase encode direction. For a 3D acquisition, another phase encode direction, k_z, is employed through the linear gradient G_z. Most of the clinical scans follow a Cartesian trajectory during the acquisitions, where one phase-encode line is acquired at each repetition time (TR). Before acquiring the signal at each line, the y- gradient is modified one step (Δk_y) to target a new spatial location in the phase-encode direction. The x-gradient, however, is turned on during the signal acquisition to capture the samples in the readout direction. The length of the readout for one echo depends on the receiving bandwidth and the number of samples in the frequency-encode direction, where the receiving bandwidth defines the number of samples collected per unit time.

For any type of acquisition, a pulse sequence is used to describe the magnitudes and the timings of the gradients waveforms, the RF pulses as well as the data acquisition. There exist a wide variety of MR pulse sequences, mainly categorized in two branches: gradient-echo sequences (GE) and spin-echo sequences (SE). For the purpose of this dissertation, we describe next the concepts of GE sequences.

المنارة للاستشارات
www.manaraa.com

1.2.3 Gradient-echo Sequences

Although water/fat imaging can be performed with SE-based sequences, GE-based sequences are usually used as they are generally faster, particularly for 3D imaging [21]. In contrast to SE, GE sequences do not employ RF refocusing pulses (π-pulse) and hence shorter TRs can be achieved as there is no need to wait for the T_1 recovery time. The TR is directly proportional to the scan time, so shorter acquisitions are achieved with GE. This is particularly important when time-restricted water/fat acquisitions are required, for example whole-liver fat quantification in a single breath-hold (~20s).

As refocusing pulses are not applied, B0 field inhomogeneities cause an additional source of dephasing, in addition to the spin-spin relaxation. In other words, the time constant T_2 in the signal equation will be replaced by T_2^*, such that:

$$1/T_2^* = 1/T_2' + 1/T_2 \tag{1.14}$$

where T_2' is the relaxation factor resulting from the local field inhomogeneities. In contrast to T_2 relaxation which is an intrinsic property of the tissue, T_2' depends on different factors including: the shimming of the magnet as well as variations in the magnetic susceptibility of the tissues within the patient [22, 23]. Measuring T_2^* is useful in various clinical applications, for example, detecting hemorrhage [24] and assessing the iron overload in liver diseases [25]. However, as T_2^* relaxation is shorter than T_2, the transverse magnetization decays faster. This makes GE images more prone to signal loss artifacts than spin-echo sequences [21, 23].

In order to understand the image produced by a GE acquisition, we must consider how the pulse sequence affects signal intensity. There is a single RF pulse in each TR of the sequence. All the RF pulses have the same flip angle α. After a number of excitations, the longitudinal magnetization reaches a *steady state*. Assuming that the transverse magnetization is zero at the beginning of each RF excitation, the GE signal can be described as follows:

المنارة للاستشارات
www.manaraa.com

$$S = M_0 \frac{\left(1 - e^{-TR/T_1}\right)}{\left(1 - \cos\alpha \,.\, e^{-TR/T_1}\right)} . e^{-TE/T_2^*} . \sin\alpha \qquad (1.15)$$

In order to achieve zero transverse magnetization before each RF pulse, '*spoiling*' the signal from previous excitations is necessary. The sequence is therefore called spoiled gradient-echo or SPGR. RF spoiling is a commonly used spoiling technique; it employs different phases for the RF pulse at each TR. Another spoiling approach is to apply additional gradient lobes on the 3 axes at the end of the TR to ensure the spoiling in all the directions. This requires that the area of any of the 3 gradients must not vary from TR to TR; otherwise the spoiling will be spatially dependent. The pulse sequence diagram of SPGR is shown in Figure 1.1

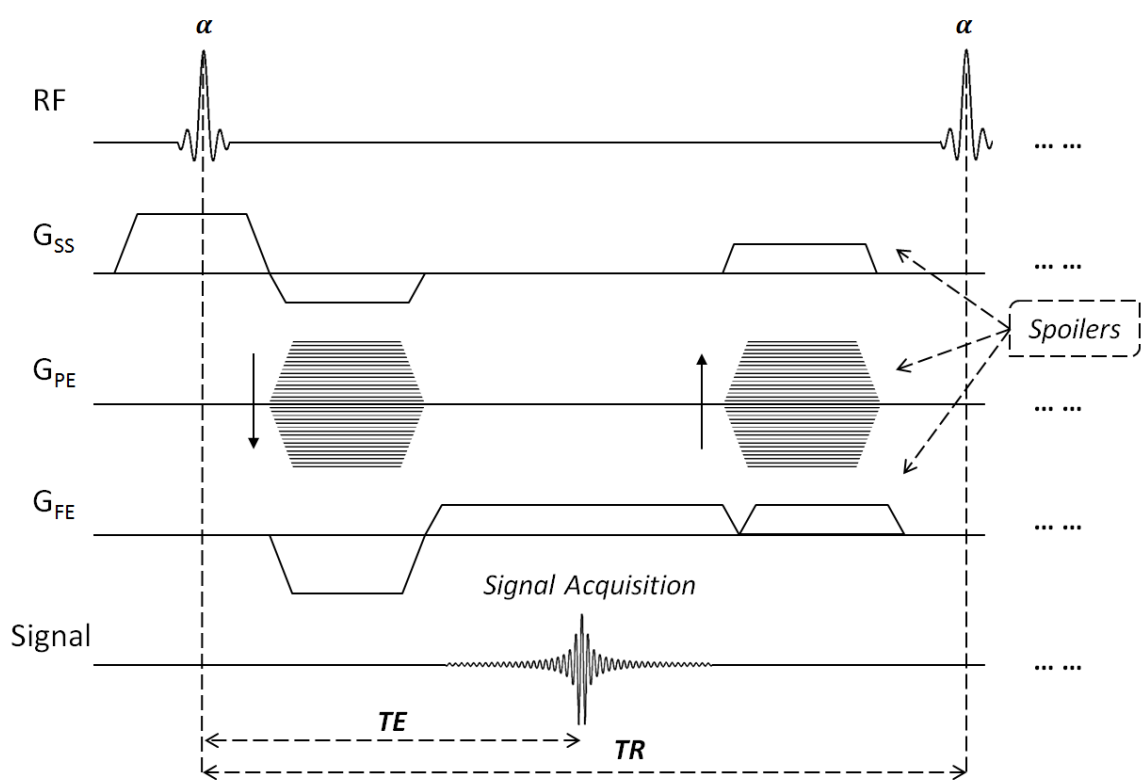

Figure 1.1: A generic SPGR pulse sequence diagram. Here an RF pulse with α flip angle is applied. G_{SS} is the slice-encode gradient; G_{PE} is the phase-encode gradient and G_{FE} is the frequency-encode gradient. TE is the echo-time of the acquired signal; TR is the repetition time. Spoilers are indicated at the end of the TR.

المنارة للاستشارات
www.manaraa.com

1.3 Water/Fat Imaging

Water and fat protons are the main sources in ^{1}H proton MR images. The suppression of fat signal is desirable whenever it obscures the underlying pathology as in breast imaging [26], head and neck imaging [27] or cardiac imaging [28]. On the other hand, detection of the fat signal is of a clinical interest in other applications such as the quantification of liver fat deposition in non-alcoholic fatty liver diseases (NAFLD) [14, 25, 29], diagnosis of myocardial fatty infiltration [15] and detection of renal angiomyolipoma [6]. In such applications, suppressing the water signal is instead required. Uniquely, chemical-shift-encoded water/fat imaging allows the separation of water and fat, while preserving both signals. It provides a water-only (fat-suppressed) and fat-only (water-suppressed) images, which makes it useful for a wide variety of clinical needs.

1.3.1 Chemical-Shift-Encoded Water/Fat Imaging

This technique exploits the frequency spectrum of fat and water signals. Because of the difference of electronic shields, the protons of fat molecules 'see' different magnetic field than what is observed by the protons in water molecules. This gives rise to a difference in the spectral components of the MR signal, with the main peak of the fat signal separated by approximately 3.5 parts-per-million (ppm) – Figure 1.2. This difference is termed the chemical-shift and is equal to ~210 Hz at 1.5 Tesla or ~420 Hz at 3 Tesla.

Chemical-shift-encoded imaging or Dixon methods [30] takes advantage of the chemical shift difference in the precession frequencies of fat and water. The protons in the fat molecules precess slower than water protons. Once the two species are simultaneously excited, a relative phase difference between fat and water protons starts to accumulate with time. Consequently, signal acquired at different time-points will exhibit different phases between water and fat due to the chemical shift difference. Hence, if we acquire multiple images at different TEs, we can solve out

المنارة للاستشارات
www.manaraa.com

the problem for the two unknown species and obtain an independent image for each species.

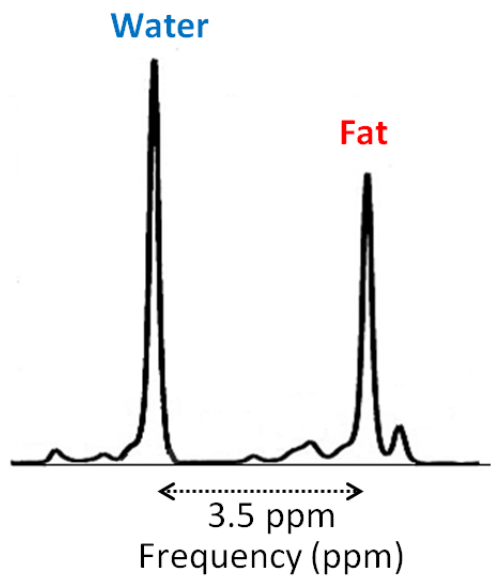

Figure 1.2: A representative frequency spectrum of the MRI signal, showing two main peaks for water and fat, separated by 3.5 ppm

Chemical-shift imaging can be combined with any pulse sequence including steady-state free-precession (SSFP) [31], fast spin-echo (FSE) [27, 32]and spoiled gradient-echo (SPGR) [33]. Also, its ability to generate fat-only and water-only (fat suppressed) images is a key advantage that made it widely used for water/fat imaging. In general, this approach can be described by a simplified model as follows:

$$S_v(t_n) = \rho_{w,v} + \rho_{f,v}\, e^{i2\pi\,\delta\, t_n} \tag{1.16}$$

where $S_v(t_n)$ is the signal acquired at voxel v at time t_n where $n = 1,..N$; $\rho_{w,v}$ represents the water component and $\rho_{f,v}$ is the fat component; δ is the chemical-shift difference (~420 Hz at 3T). This model has neglected other factors as T_2^* effect and the multi-peak frequency spectrum of fat.

المنارة للاستشارات
www.manaraa.com

In the last decade, extensive research has been conducted on Dixon-based methods showing its robustness in separating water and fat, offering unique advantages over other approaches. The next sections we will describe different Dixon-based methods in further detail.

1.3.2 Two-Point Dixon

Dixon first proposed his method by acquiring 2 images at 2 different TEs [34]. The first TE is adjusted to acquire an "in-phase" image where water and fat have the phase value. The second acquisition is an "out-of-phase" one where water and fat exhibit a π phase difference. Water and fat components can be therefore obtained by simply adding and subtracting the two acquired images - Figure 1.3, leading to:

$$\hat{\rho}_w = \frac{1}{2}\left|S(t_{ip}) + S(t_{op})\right| \tag{1.17}$$

$$\hat{\rho}_f = \frac{1}{2}\left|S(t_{ip}) - S(t_{op})\right| \tag{1.18}$$

where t_{ip} and t_{op} are the TE values where fat and water are in-phase and out-of-phase, respectively. The original work was done using spin-echo sequence, where the TE shift was performed by shifting the refocusing pulse by ΔTE/2. However, it can be also achieved with GE sequence where two readout gradients are played out at the prescribed TEs [33]. This method assumes that the main magnetic field is homogenous, which is difficult to achieve in practice due to tissue susceptibility differences, even if perfect shimming was attained. As the field inhomogeneities disrupt the phase information, sophisticated phase unwrapping techniques are therefore required to correct water/fat errors. Recently, Ma *et al.* [35] proposed a region-growing scheme to address this problem by using the magnitude and phase information of neighboring voxels . However, due to the complexity of the phase unwrapping methods needed to correct for field inhomogeneities, three-point Dixon methods were proposed instead.

المنارة للاستشارات
www.manaraa.com

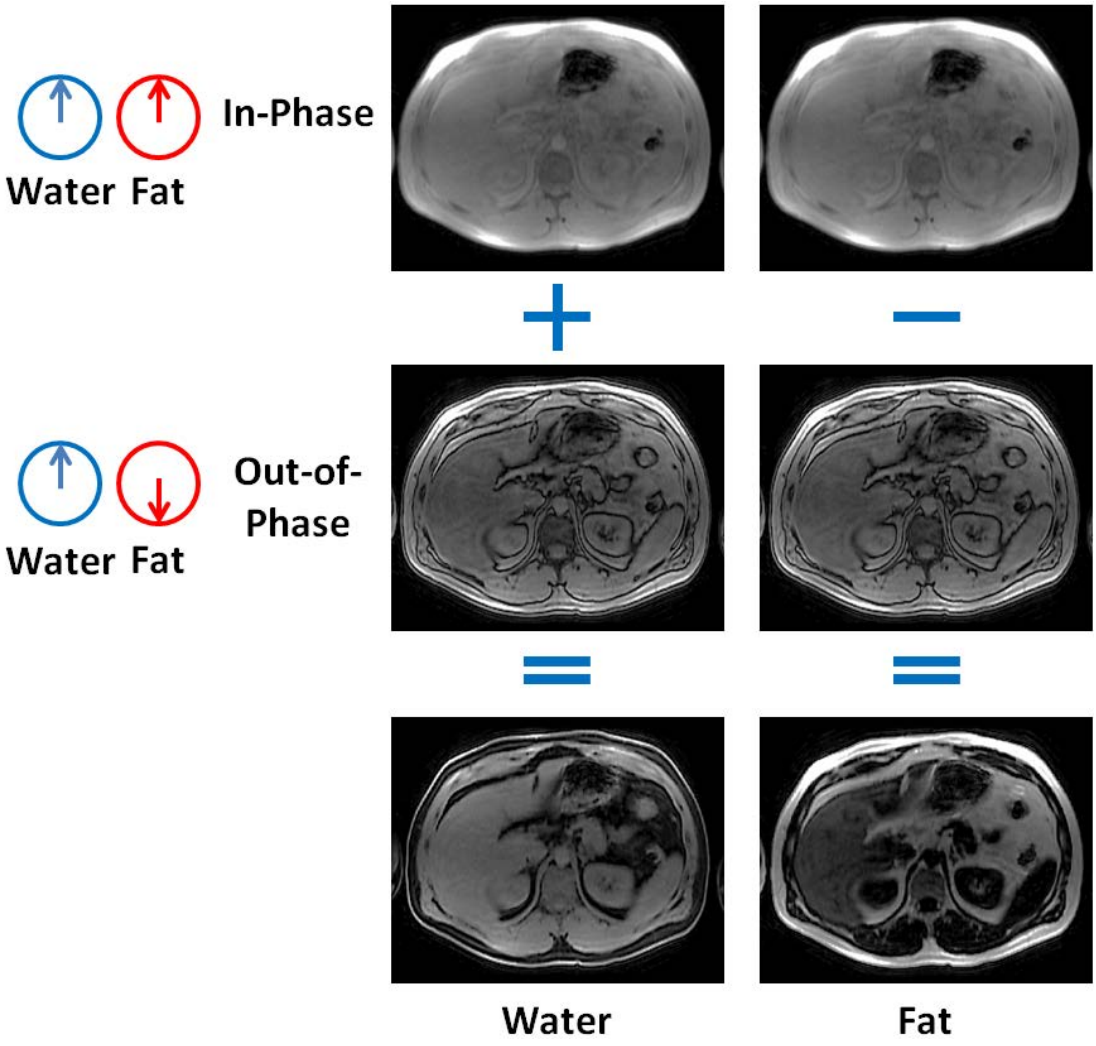

Figure 1.3: The two-point Dixon method reconstructs water and fat images by adding and subtracting in-phase and out-of-phase images, respectively.

المنارة للاستشارات
www.manaraa.com

1.3.3 Three-point Dixon

Glover and Schneider proposed the three-point Dixon method to estimate the magnetic field inhomogeneities [36]. Using a spin-echo sequence, they acquire three images at 3 different TEs where fat and water exhibit relative phase-shifts of $-\pi$, 0 and π. The signal model from the 3 acquisitions can be described as follows:

$$S(t_{-\pi}) = \left(\rho_w - \rho_f\right) e^{i(\theta_0 - \theta)} \tag{1.19}$$

$$S(t_0) = \left(\rho_w + \rho_f\right) e^{i\theta_0} \tag{1.20}$$

$$S(t_\pi) = \left(\rho_w - \rho_f\right) e^{i(\theta_0 + \theta)} \tag{1.21}$$

where θ_0 is an unknown systematic phase offset, while θ is the unknown phase term resulting from the field inhomogeneities. After demodulating θ_0 of all the 3 acquisitions using Equation 1.20, water and fat components can be derived as follows:

$$\rho_w = \frac{\left(S'(t_0) + \beta\sqrt{S'(t_\pi)\,.\,S'(t_{-\pi})}\right)}{2} \tag{1.22}$$

$$\rho_f = \frac{\left(S'(t_0) - \beta\sqrt{S'(t_\pi)\,.\,S'(t_{-\pi})}\right)}{2} \tag{1.23}$$

where S' is the signal after omitting θ_0 and $\beta = \pm 1$ is a switch function for sign of the complex square root. However, in order to assign the correct β sign, a phase unwrapping algorithm is required. The main limitation of Glover and Schneider's technique is that it restricts the acquisition to $-\pi$, 0 and π. A more flexible version of the three-point Dixon was proposed by Xiang and An [37] where the 3 acquisitions are acquired at uniformly-spaced TE shifts. The field inhomogeneity φ is then estimated through a quadratic equation in the phasor term $e^{-i2\pi\varphi\Delta t}$. Similar to Glover and Schneider's [36], two possible solutions can be obtained from the solution of the quadratic equation. The ambiguity in assigning the correct sign will lead to errors in the estimated water and fat components.

المنارة للاستشارات
www.manaraa.com

1.3.4 IDEAL

A novel perspective to the three-point Dixon was introduced by Reeder *et al.* [38] based on a maximum likelihood estimation of the signal. They introduced the "Iterative Decomposition of water and fat with Echo Asymmetry and Least-squares estimation" (IDEAL) where a nonlinear least-squares fitting is performed at each voxel. A general description of the acquired signal at voxel, v, can be given by re-writing Equation 1.16 as follows:

$$S_v(t_n) = \left(\sum_{c=1}^{C} \rho_{c,v} \, e^{i2\pi \, \delta_c \, t_n} \right) . \, e^{i2\pi \, \varphi \, t_n} \tag{1.24}$$

Where C is the number of species, $\rho_{c,v}$ is a complex-valued chemical species with δ_c representing its chemical-shift from the main water-peak (in Hz) and φ is a map of the field inhomogeneities, so called *field map*. The key point of IDEAL is solving the problem in an iterative linearization procedure of the signal equation – Figure 1.4. The approach can be summarized:

a. An initial estimate is given to φ. Usually it is set to zero.
b. The chemical species can be then estimated directly through solving a linear least-squares problem.
c. The estimates $\{\hat{\varphi}, \hat{\rho}_{c,v}\}, c = 1, .., C$ are then fed into a linearized signal model, where $e^{i2\pi \, \Delta\varphi \, t_n}$ is approximated through Taylor expansion by $1 + i2\pi \, \Delta\varphi \, t_n$.
d. The signal residues from these estimates are then calculated
e. A new value for the field map is calculated $\varphi_{i+1} = \varphi_i + \Delta\varphi$, where i is the iteration number.
f. Step (b-e) are repeated until $\nabla\varphi$ converges (e.g. < 1 Hz).
g. Calculate the final estimates of φ and $\rho_{c,v}$ for all chemical species.

An additional spatial smoothing filter can be added after step f. on the field map to improve the noise performance.

المنارة للاستشارات
www.manaraa.com

IDEAL has several advantages over previous approaches: 1) it can be used with arbitrary TEs; 2) it can be combined with any imaging sequence; 3) it works for any number of chemical species i.e. not restricted to water/fat applications; 4) complex-valued chemical species are estimated, which enhances the effective number of signal averages (NSA) of the reconstruction (refer to 1.3.5 for more details). On the other hand, a major drawback of IDEAL is the initial value required for the field map φ; If not correctly estimated for each voxel, the algorithm will converge into local minima and wrong estimates of water/fat will be obtained. Hence, IDEAL will fail in cases where large inhomogeneities are encountered as it does not enforce any global solution to the iterative procedure. Several techniques have been proposed to resolve the large variations in the field map [9, 39-46]. Although some methods have demonstrated the ability to address challenging cases, an ultimate solution to the field map estimation problem has yet to be explored. In Chapters 2 and 3 we will propose new methods to overcome the drawbacks of IDEAL.

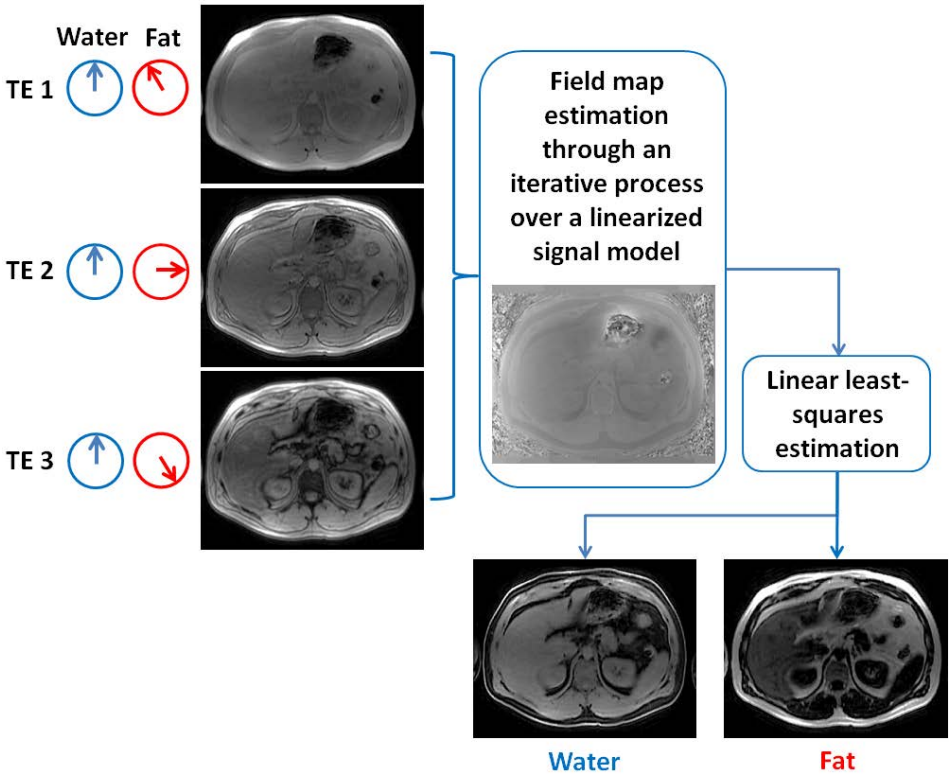

Figure 1.4: Illustration of the IDEAL water/fat separation process.

المنارة للاستشارات
www.manaraa.com

1.3.5 Characterization of Noise Performance

The noise performance of water/fat separation methods rely on multiple of acquisition and reconstruction parameters [47]. The common metric to evaluate the noise performance is the effective number of signal averages (NSA) given by

$$NSA = \frac{\sigma^2}{\sigma_p^2} \tag{1.25}$$

Here σ^2 and σ_p^2 are the variance of the noise in the source image and the reconstructed fat (or water) image, respectively. The minimum achievable σ_p^2 is calculated using the Cramér-Rao bound, which is defined as the lower bound on the variance of an unbiased estimate. Hence it can be used to optimize the acquisition parameters to attain the highest noise performance. Pineda *et al.* [47] showed that for 3-point Dixon, echo-shifts of $(\frac{\pi}{6} + \pi K, \frac{\pi}{2} + \pi K, \frac{7\pi}{6} + \pi K)$ achieves best theoretical performance using the signal model of Equation 1.24 for water and fat species. In theory, the maximum achievable NSA for n-point acquisition is n. NSA depends mainly on a number of factors: the number of echoes, the first echo, the echo-shifts and the number of unknown parameters to be estimated in the reconstruction [47, 48]. The type of the reconstruction (magnitude-based or complex-based) also affects the noise performance, as discussed later in 1.4.4.

المنارة للاستشارات
www.manaraa.com

1.4 Quantitative Fat Imaging

Fat quantification is usually performed in terms of fat fraction, which is the ratio of the fat signal to the total signal from both water and fat. Several confounding factors can bias the fat measurement and must be considered in the reconstruction. Once these factors are addressed, the fat fraction will be equivalent to what is referred to as *proton density fat-fraction* (PDFF) which is defined as the ratio of density of mobile protons from fat to the total density of mobile protons from fat and water. PDFF is currently considered the most practical and meaningful MR-based biomarkers for fat quantification [49]. Current research is seeking its standardization for clinical diagnosis.

1.4.1 Multi-peak Fat Spectrum

The signal model presented in Equation 1.16 and Equation 1.24 assumes that fat exhibits one peak in the frequency spectrum of the MR signal. However due to the complex nature of fat molecule, its protons vary in their precession frequencies. It was shown that the fat spectrum can have up to 6 peaks with different amplitudes – Figure 1.5. A significant bias in the fat fraction measurements will occur if only the main peak is considered [50]. Therefore, a multi-peak fat spectrum is included in the signal equation as follows:

$$S_v(t_n) = \left(\rho_{W,v} + \rho_{F,v} \cdot \sum_{m=1}^{M} \alpha_m . e^{i2\pi\, \delta_m\, t_n}\right) . e^{i2\pi\, \varphi_v\, t_n} \tag{1.26}$$

where M is the number of fat peaks; δ_m is the frequency of the m-th peak with its corresponding amplitude α_m (Hz), such that $\sum_{m=1}^{M} \alpha_m = 1$.

المنارة للاستشارات
www.manaraa.com

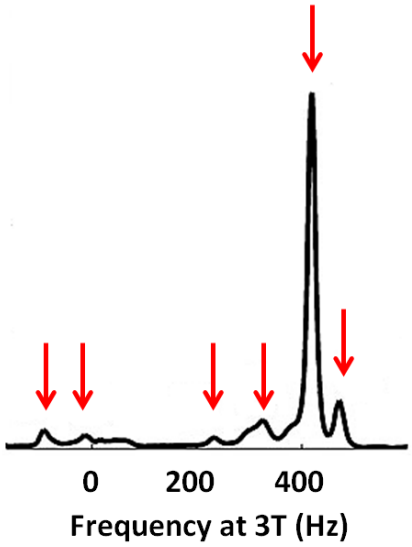

Figure 1.5: Frequency spectrum of knee subcutaneous fat showing 6 peaks, with the main peak located at ~420 Hz (3.5 ppm) – Figure adapted from [50].

Equation 1.26 now includes additional 2M unknowns: frequencies and amplitudes of the fat peaks. Fortunately, the frequencies are well documented in the literature [51-53] and can be assumed to be constant. There are two approaches to obtain the amplitudes: self-calibrated and pre-calibrated methods. In the self-calibrated method different fat peaks are treated as different chemical species and hence large number of echoes (images) are required to solve Equation 1.26. For instance Yu *et al*. [50] used 16 echoes in order to obtain an accurate fit for all the peaks. On the other hand, the pre-calibrated approach assumes predetermined amplitude values for the fat peaks and hence it leads to the same number of unknowns. Several studies have shown that including the multi-peak fat spectrum improves the accuracy of estimating the fat fraction compared to the single peak approach [14, 25, 29, 48, 49].

المنارة للاستشارات
www.manaraa.com

1.4.2 Effect of T_2^* Relaxation

In Equation 1.24 and Equation 1.26, T_2^* decay was assumed to be negligible. However, this assumption can lead to substantial errors in the fat fraction estimate [14, 54, 55], particularly with rapid T_2^*. Additionally, T_2^* itself might be of diagnostic interest in some cases, such as hepatic iron overload, as R_2^* ($1/T_2^*$) is strongly correlated to the iron deposition. Likewise, the presence of fat can lead to wrong T_2^* estimates. Therefore, methods that consider single-T_2^* [54] and dual-T_2^* [56] decays during water/fat reconstruction have been introduced. The latter approach estimates two T_2^* values for water and fat respectively, while the single-T_2^* approach ignores that difference and a single combined decay is deduced at each voxel. In theory, fat fraction bias should decrease with dual-T_2^*[55]; however, the noise performance significantly degrades as more unknown parameters are included in the reconstruction process [48]. Consequently dual-T_2^* models result in noisy estimates of fat fraction. In practice, studies have shown that single-T_2^* modeling is more accurate than dual-T_2^* model for fat quantification, even with high fat concentration [57].

Yu *et al.* [50, 54] has extended the 3-point IDEAL method (sec 1.3.4) to consider the T_2^* decay together with an accurate spectral modeling of fat (sec 1.4.1). They extended the signal model to include a single T_2^* decay per voxel, and simultaneously estimate a T_2^* map and the field map in the iterative IDEAL process. Pre-calibrated and self-calibrated spectral models of fat were used in the signal model. Six-point acquisition with pre-calibrated fat spectrum was therefore recommended as a good compromise between acquisition time and accurate mapping of the T_2^* decay. Figure 1.6 illustrates the extended T_2^*-IDEAL method for 6-point acquisition.

المنارة للاستشارات
www.manaraa.com

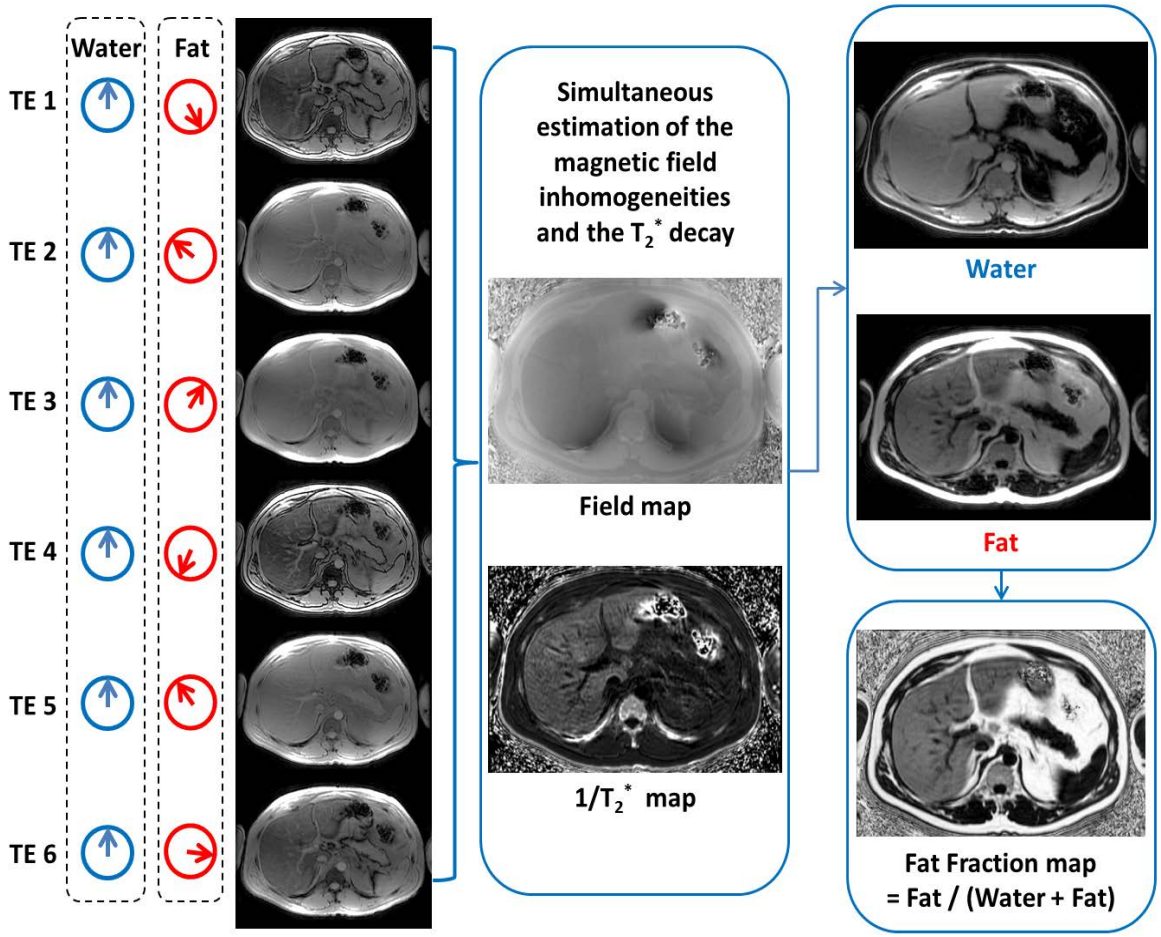

Figure 1.6: Illustration of the 6-point T_2^*-IDEAL proposed by Yu *et al.* [50, 54]

المنارة للاستشارات
www.manaraa.com

1.4.3 T_1-related bias

Fat has shorter T_1 relaxation time than water. This may result in a dissimilar weighting between water and fat signals in the acquired image, as the signal received from fat protons is higher compared to that received from water. Consequently, significant bias in the fat fraction measurements can occur [58]. Accurate PDFF quantification necessitates the correction of T_1-related bias [49, 58, 59].

In SPGR-based Dixon acquisitions, The T_1-weighting of the acquired signal changes with the flip angle (Equation 1.15). Therefore, applying RF pulses with small flip angles will minimize the T_1-related bias in the PDFF estimates [14]. The main drawback is the loss of SNR which increases the standard deviation of fat fraction measurements. Another approach is the dual-flip angle T_1 correction [60]. In contrast to small flip angle approach, this method finds a definitive analytical solution by performing two consecutive acquisitions with different flip angles, and then derives T_1-corrected water and fat images. Although it eliminates the T_1 effect, it doubles the acquisition time. Recently another approach was proposed by Yang *et al*. [61] where a relatively high flip angle is used (8°), followed by a T_1-bias correction of the reconstructed water and fat images, where pre-determined T_1 values of each species are used. This technique has the advantage of higher SNR while the T_1-bias is also corrected. However, this method requires mapping the flip angle variations (so called flip angle map) to enhance the resultant fat fraction estimates. In general, a small flip angle of ~3° is usually used in clinical practice, as it provides a good compromise between T_1-bias correction and SNR [62]. It was shown that flip angles 3°-5° would cause < 2% bias over 0-100% fat fractions and < 1% bias for low fat concentrations, while preserving good SNR quality [60]. Moreover, it does not require any additional acquisitions. In this dissertation, T_1-bias will be minimized using the small flip angle approach.

المنارة للاستشارات
www.manaraa.com

1.4.4 Eddy Currents

To shorten the acquisition time, multi-point chemical-shift-encoded sequences perform multiple readout gradients in each TR – Figure 1.7. Eddy currents are generated at each time the gradients are switched 'on' and 'off' producing phase errors in the acquired signals. In a multi-echo SPGR acquisition, the gradient waveform preceding the first readout is different from the waveforms preceding the other echoes. Hence, the generated eddy currents and subsequently the resulting phase errors are different in the first echo from the rest of the echoes. These asymmetric phase errors affect the water/fat separation process, leading to fat-fraction bias. To address this problem, magnitude-based reconstruction is used, where the phase information is omitted. This leads to significant noise amplification in the fat fraction image compared to the complex-based reconstruction where the complex signals are considered [48].

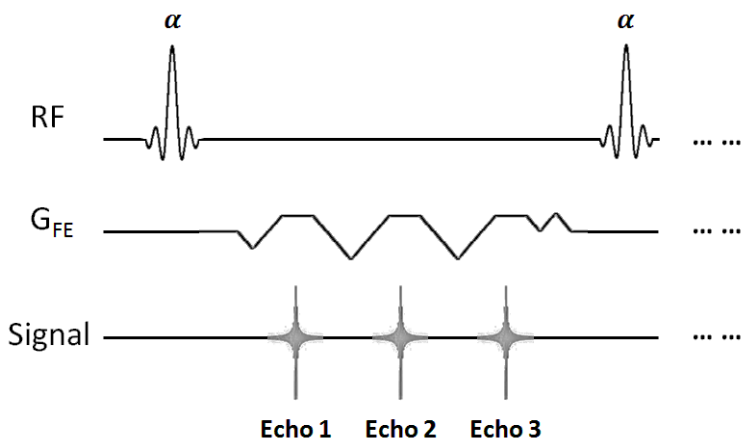

Figure 1.7: Three readout gradients are applied in one TR to acquire 3 echoes.

Yu *et al.* [63] have addressed this problem by performing a hybrid fit where the magnitude-based and complex-based reconstructions are combined together with different weights. This has improved the noise performance compared to the magnitude-based approach. Another method is the mixed magnitude/complex fitting proposed by Hernando *et al.* [48] where only the phase of the first echo is neglected, while the complex signals in all the subsequent echoes are considered.

المنارة للاستشارات
www.manaraa.com

This method has led to further SNR improvement over the hybrid method. Recently Wade *et al*. [64] suggested modifying the waveforms of the readout gradient to generate similar eddy currents at the first echo as the rest of the echoes. This will compensate for the fat fraction bias as the phase errors will be approximately the same at all the echoes. However, SNR loss might occur from the insertion of an additional waveform before the first echo. We address the eddy currents-induced fat fraction bias with our new acquisition strategy proposed in Chapter 4.

1.4.5 Noise-related bias

Fat fraction bias might also occur when one of the species is at very low concentrations, due to noise amplification. Liu *et al.* [60] addressed this problem by using the 'phase-constrained' hypothesis where fat and water are assumed to have same phase at TE=0. Hence, instead of using the magnitude of fat and water signals to calculate the fat fraction, complex values will be used, such that $FF = S_f/(S_f + S_w)$ for fat-dominant-pixels and $FF = 1 - (S_w/(S_f + S_w))$ for water-dominant pixels, where S_f and S_w are the complex signals of fat and water, respectively. This approach has shown to overcome the bias occurring at very low and very high fat concentrations.

1.4.6 Temperature-related bias

In contrast to fat protons, the proton resonant frequency of the water is dependent on temperature [65]. Hence, the chemical-shift between fat and water is altered, causing unexpected bias in the fat fraction. Magnitude-based reconstructions are largely affected by the temperature change, and can cause significant bias. However, complex reconstructions are more robust to temperature-dependent bias, particularly at room temperature (~20°C) and body temperature [65]. Although the signal model can be modified to account for the temperature-dependent chemical-shift frequency, the additional parameter will reduce the NSA.

المنارة للاستشارات
www.manaraa.com

1.5 Parallel Imaging

In general, water/fat imaging requires lengthy acquisitions. Hence, for time-restricted applications, accelerated data acquisition is required. The most common acceleration technique in clinical practice is parallel imaging [66-70].

For a 2D acquisition the scan time is calculated as $t = NSA\,.N_y\,.TR$, where NSA is the number of signal averages and N_y is the number of phase encodes. Hence for a prescribed TR, the fewer phase encodes the shorter the acquisition time will be. However, this will violate Nyquist criterion in k-space, causing *aliasing* artefacts in the image domain - Figure 1.8(b). Parallel imaging techniques address this problem by recovering the missing data from subsampled *k*-space and hence allow aliasing-free accelerated acquisitions. Reconstruction techniques can either recover the omitted data in *k*-space (e.g. GRAPPA) [66, 67, 69], or un-fold the aliased images in image-domain (e.g. SENSE) [70, 71] – Figure 1.8. For 3D imaging, acceleration can be achieved in both the phase and the slice directions by acquiring fewer slice/phase encodes and recovering them in the reconstruction. This will allow even shorter acquisition times.

The key for parallel imaging is taking advantage of a phased-array of coils. In fact, each coil has a non-uniform receive profile - known as coil sensitivity - which is used as calibration data in the reconstruction. Parallel imaging reconstruction techniques, therefore, employ the calibration data to recover the missing slice/phase encodes, whether in *k*-space or image-domain.

The drawback of acceleration by parallel imaging is the reduction of signal-to-noise (SNR). The SNR loss is equal to the square-root of the acceleration factor multiplied by the so-called "*g*-factor". The g-factor describes an additional spatially-variant noise amplification in the reconstruction [71] and varies depending on the geometry and the number of the coils [68, 71].

المنارة للاستشارات
www.manaraa.com

In chapter 4 of this dissertation we will use conjugate-gradient SENSE for parallel imaging reconstruction [71]. This is an image-based reconstruction technique that uses an iterative approach to un-alias the acquired undersampled data.

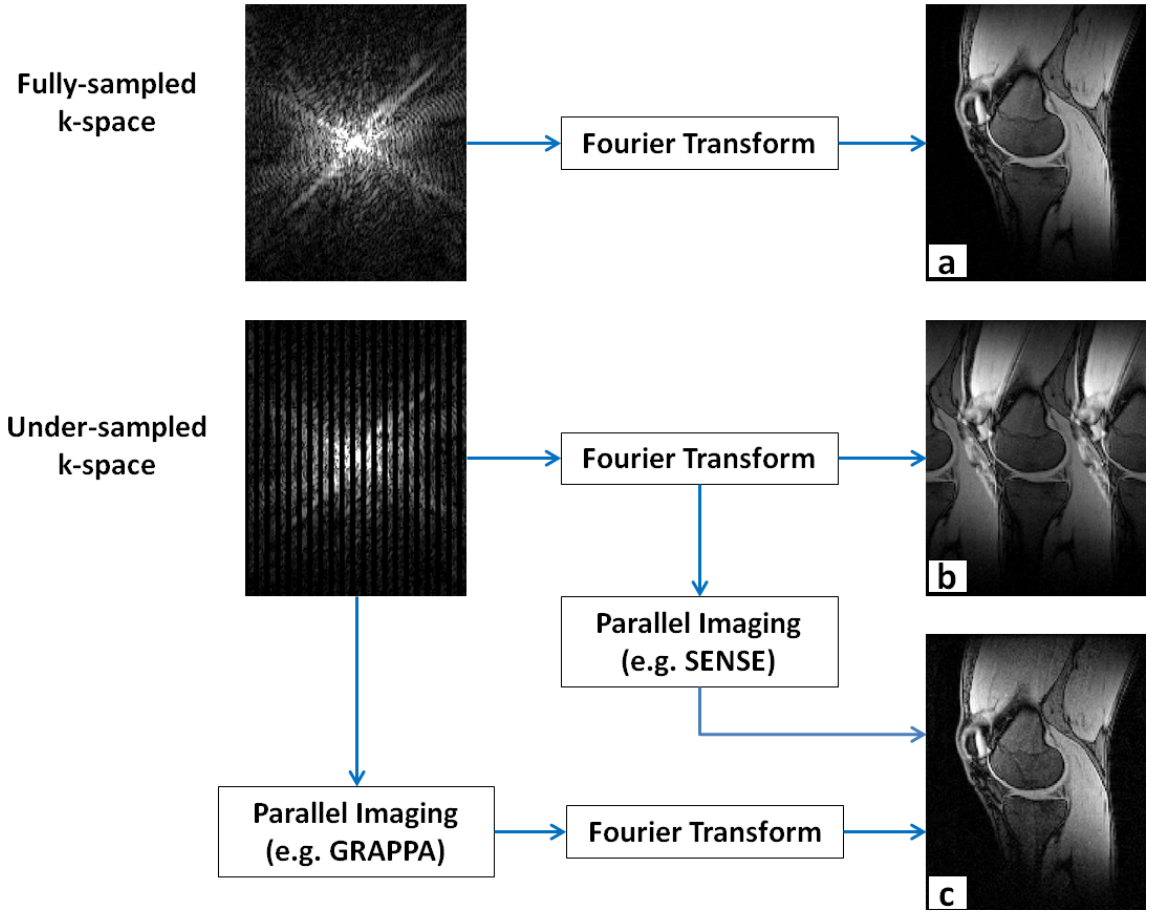

Figure 1.8: (a) A knee image obtained from the Fourier transform of a fully-sampled k-space. (b) Undersampling the k-space results in an aliased image. (c) The image is reconstructed from the undersmapled k-space using Parallel Imaging reconstruction.

المنارة للاستشارات
www.manaraa.com

1.6 Network Optimization Problems

Resolving the correct field map inhomogeneities in Equation 1.26 is a challenging problem that becomes even more complicated when the confounding factors mentioned above are included in the signal equation. To address this problem, sophisticated optimization techniques can be employed. One of the main branches of mathematical optimization is network optimization techniques, which are employed in Chapters 2 and 3 to estimate the magnetic field inhomogeneities.

1.6.1 Terminology

Basically, a network is defined as a graph constituted of two main objects: nodes and edges. For instance if an image is mapped through a network, each pixel is represented by a node, while *weighted* edges connect each pixel to other pixels in a local neighbourhood. Moreover, two special nodes are added, a sink node and a source node. The source and sink nodes are connected to all the other nodes in the graph – Figure 1.9.

A *flow* in a network is simply a quantity that is flowing in an edge from one node to another. Mathematically, a flow of an edge is just a scalar number added on it. A flow can have negative values, where in this case it flows in the opposite direction to the edge. There are two main constraints on the flows of the network: *capacity constraints* and *flow conservation*. To define them let's assume we have a graph (V, E), where $V$and E are the nodes and the edges, respectively. The grid also has two terminal nodes, a sink t and a source s. There are three sets of flows: source flows, ρ_s, from the source node s to each node in the grid; sink flows, ρ_t, from each node into the sink node t; and spatial flows q between the nodes of the grid. The capacities constraining the flows in the network are defined as follows:

- Capacity of source flows, ρ_s, from s to node $v \in V\backslash\{s,t\}$: $0 \leq \rho_s(v) \leq C_s(v)$
- Capacity of the sink flows, ρ_t, from node $v \in V\backslash\{s,t\}$ to t: $0 \leq \rho_s(v) \leq C_t(v)$
- Capacity of spatial flows, q, for the edges of the grid $e \in E$: $|q(v)| \leq C(v)$;

المنارة للاستشارات
www.manaraa.com

where $C_s(v)$, $C_t(v)$ and $C(v)$ are the capacities of the corresponding flows. When a spatial flow $q(e)$ over the edge $e \in E$ reaches its maximum capacity, it is called a 'saturated' flow.

The other constraint is the flow conservation, which is defined at node $v \in V\backslash\{s,t\}$ as follows:

$$\left(\sum_{e \in I(v)} q_e(v)\right) - \rho_s(v) + \rho_t(v) = 0 \tag{1.27}$$

where $I(v) \subset E$ is the set of the neighbour edges of the node v. In other words, this constraint states that the total flow departing from the node must be balanced by the arriving flow at the node. By definition, only the source and sink nodes are exempted from this constraint. The flow conservation and the capacity constraints are important conditions that will control the solution of max-flow problems, described next.

1.6.2 Min-cut / Max-flow problem

In a graph network, each edge has a cost. A *cut* that separates the source node from the sink node will have a total cost equal to the sum of all the edges it passed through. The *minimum-cut* (min-cut) problem consists of finding the cut that has the lowest cost – Figure 1.9. Finding the optimal solution of an optimization problem corresponds to finding the min-cut of its graph-network. The graph-cut algorithm by Boykov *et al.* [72, 73] is a widely used algorithm to explore the min-cut of a network. Equivalent to the min-cut solution is finding the maximum-flow of the network. In fact, *min-cut/max-flow* theorem is very popular in network optimization. In max-flow we try to maximize the flow from the source node, while maintaining the capacity and the flow conservation constraints, i.e.

$$\max_{\rho_s} \sum_{v \in V\backslash\{s,t\}} \rho_s(v) \tag{1.28}$$

المنارة للاستشارات
www.manaraa.com

subject to the constrains mentioned above. The path that allows the maximum flow divergence out of the source node is equal to the minimum cut that separates the source from the sink. There are a growing number of medical applications that rely on min-cut/max-flow approaches as efficient optimization methods.

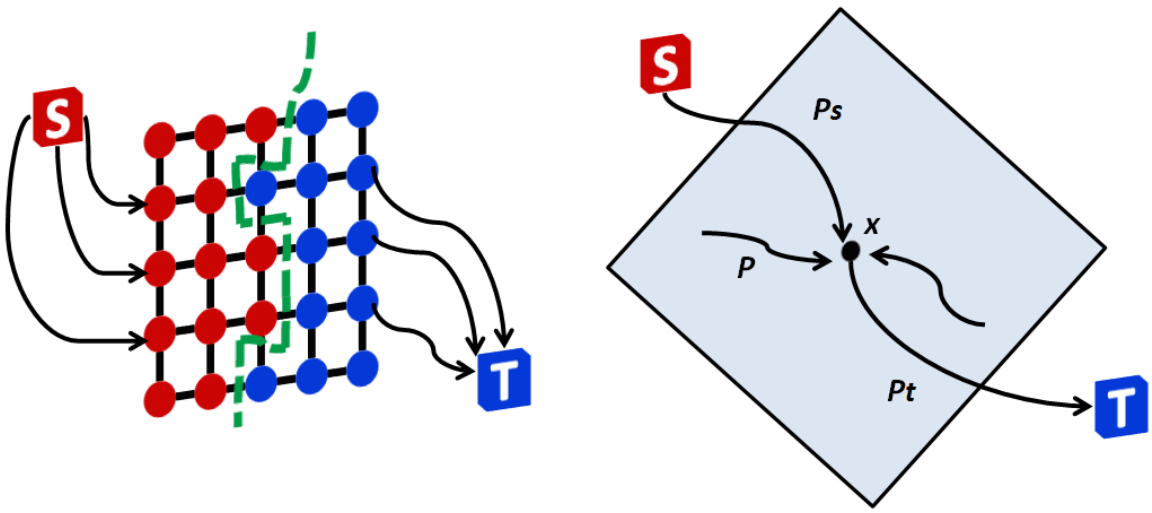

Figure 1.9: Left: A discrete flow network problem with a min-cut solution. Right: A Continuous flow network problem.

1.6.3 Continuous Max-flow

The max-flow problem formulated in the previous section was introduced in the discrete setting, and can be formulated in the same manner on a continuous domain. Let $x \in \Omega$ be a spatial position on a continuous 2D or 3D domain, Ω. The flow constraints can be reformulated as follows:

$$\rho_s(x) \leq C_s(x), \tag{1.29}$$

$$\rho_t(x) \leq C_t(x), \tag{1.30}$$

$$|\rho(x)| \leq C(x), \tag{1.31}$$

$$(\operatorname{div} q - \rho_s + \rho_t)(x) = 0 \tag{1.32}$$

المنارة للاستشارات
www.manaraa.com

Where div $q(x)$ is the divergence of the flow at x representing the total spatial flow, which is analogous to the sum operator in Equation 1.28. The continuous max-flow model can now be formulated as follows:

$$\max_{\rho_s,\rho_s,\rho} \int_{\Omega} \rho_s(x) \quad dx \tag{1.33}$$

subject to the constraints in Equations 1.29-1.32. By introducing a multiplier u to the flow conservation in Equation 1.33, the max-flow model can be re-written as follows:

$$\max_{\rho_s,\rho_s,\rho} \min_{u} \int_{\Omega} \rho_s(x) \quad dx + \int_{\Omega} u\,(\operatorname{div} q - \rho_s + \rho_t)(x) \quad dx \tag{1.34}$$

$$s.t. \qquad \rho_s(x) \leq C_s(x), \qquad \rho_t(x) \leq C_t(x), \qquad |\rho(x)| \leq C(x)$$

Analogous to the discrete setting, the continuous max-flow model in Equation 1.34 is equivalent to the continuous min-cut solution. Yuan *et al.* [74] have proposed a fast continuous max-flow algorithm to address Equation 1.34 using its augmented Lagrangian function. They use an iterative approach where the multiplier u is updated at each iteration. This algorithm has been used in numerous medical applications such as segmentation of vascular structures [75], segmentation of left ventricle [76], image fusion[77] and delineation of myocardial scar tissue [78]. The main advantage of the continuous max-flow over the graph cut is its ability to find a global solution to problems where a graph-based global solution is inefficient and/or impractical, such as resolving the field map inhomogeneities. Moreover, the continuous max-flow is implicitly parallelized, i.e. its computations can be solved in parallel using modern Graphics-processing Units (GPUs). In Chapters 2 and 3, we will explore two different methods using the continuous max-flow algorithm to map magnetic field inhomogeneities.

المنارة للاستشارات
www.manaraa.com

1.7 Thesis Outline

The thesis presents novel acquisition and reconstruction methods for water/fat separation with *in-vivo* applications on various human organs. Chapter 2, 3 and 4 are based on published peer-reviewed articles to Magnetic Resonance in Medicine (MRM) and Medical Image Computing and Computer Assisted Intervention (MICCAI).

In Chapter 2 a novel water/fat separation technique is introduced. The chapter is adapted from a peer-reviewed paper published in MICCAI 2012 proceedings. The technique estimates magnetic field inhomogeneities that hinder the reconstruction process. In contrast to most of the previous work that rely on spatial smoothness, the presented method uses a labeling model to resolve the ambiguity of the estimation. An initial guess of the field map is generated first then the estimate is subsequently refined using an IDEAL iterative process. The number of labels used to describe the initial estimate is penalized in the cost function to enforce fewer labels. This was shown to reduce the vulnerability of converging to local minima. In-vivo experiments were performed on cardiac and abdominal datasets showing excellent water/fat separation. The results were compared against the commonly-used region-growing method and have demonstrated significant outperformance in case of abrupt changes of magnetic field.

In Chapter 3 an optimized version of the method proposed in the previous chapter is presented. The effect of T_2^* decay was integrated in the labeling process. The initial estimate becomes better representative of the signal model and therefore more robust to local minima. In addition, an adaptive spatial filtering was introduced after the labeling procedure to enhance the performance of the method. A continuous max-flow approach was employed to address the labeling model, while T_2^*-IDEAL is applied in the second stage; the technique is therefore called Max-IDEAL. *In-vivo* data from the ISMRM challenge 2012 on water/fat separation were used to test the technique, resulting in successful separation in 98.44% of cases. The method was also tested against recent robust techniques as graph-cut and the FLAME methods

المنارة للاستشارات
www.manaraa.com

on *in-vivo* cases with severe inhomogeneities and has demonstrated successful water/fat separation while the other methods failed.

In Chapter 4 a new multi-gradient-echo bipolar acquisition sequence for fat quantification is proposed. This new acquisition strategy is more efficient than the current unipolar sequence currently employed in clinical practice. The sequence applied bipolar gradients at the frequency-encode gradient while alternating the polarity in the temporal dimension as well as the phase-encode dimension. The acquisition and reconstruction pipeline overcomes the bipolar artefacts known to corrupt the water/fat separation procedure. Phantoms and *in-vivo* experiments demonstrated accurate fat fraction and increased SNR efficiency compared to the established unipolar acquisition. Phase and magnitude artefacts from the bipolar acquisition were eliminated in all experiments.

In Chapter 5 the efficiency of the interleaved bipolar acquisition proposed in the previous chapter is demonstrated in animal experiments. One of the common applications of water/fat separation is to study obesity on animal models. Fat and water images with high spatial resolution are required. Using the interleaved bipolar sequence, the spatial resolution was doubled while keeping the same acquisition time as the standard unipolar sequence. The results also demonstrated higher SNR efficiency of the interleaved bipolar compared to the unipolar sequences.

In Chapter 6, improvements on the reconstruction and acquisition techniques are suggested with further applications, and the work presented in this dissertation is concluded.

المنارة للاستشارات
www.manaraa.com

References

[1] Alfire, M. E. and Treem, W. R., "Nonalcoholic fatty liver disease," *Pediatr Ann,* vol. 35, pp. 290-4, 297-9, Apr 2006.

[2] Iozzo, P., "Myocardial, Perivascular, and Epicardial Fat," *Diabetes Care,* vol. 34, pp. S371-S379, 2011.

[3] Börnert, P., Koken, P., Nehrke, K., Eggers, H., and Ostendorf, P., "Water/fat-resolved whole-heart Dixon coronary MRA: An initial comparison," *Magnetic Resonance in Medicine,* vol. 71, pp. 156-163, 2014.

[4] Shin, P. J., Larson, P. E. Z., Ohliger, M. A., Elad, M., Pauly, J. M., Vigneron, D. B.*, et al.*, "Calibrationless parallel imaging reconstruction based on structured low-rank matrix completion," *Magnetic Resonance in Medicine,* vol. 72, pp. 959-970, 2014.

[5] Siepmann, D. B., McGovern, J., Brittain, J. H., and Reeder, S. B., "High-resolution 3D cartilage imaging with IDEAL–SPGR at 3 T," *American Journal of Roentgenology,* vol. 189, pp. 1510-1515, 2007.

[6] Israel, G. M., Hindman, N., Hecht, E., and Krinsky, G., "The use of opposed-phase chemical shift MRI in the diagnosis of renal angiomyolipomas," *American Journal of Roentgenology,* vol. 184, pp. 1868-1872, 2005.

[7] Schick, F., Weiss, B., and Einsele, H., "Magnetic resonance imaging reveals a markedly inhomogeneous distribution of marrow cellularity in a patient with myelodysplasia," *Annals of hematology,* vol. 71, pp. 143-146, 1995.

[8] Schick, F., Einsele, H., Lutz, O., and Claussen, C., "Lipid selective MR imaging and localized 1H spectroscopy of bone marrow during therapy of leukemia," *Anticancer research,* vol. 16, pp. 1545-1551, 1995.

المنارة للاستشارات
www.manaraa.com

[9] Berglund, J., Johansson, L., Ahlström, H., and Kullberg, J., "Three-point dixon method enables whole-body water and fat imaging of obese subjects," *Magnetic Resonance in Medicine,* vol. 63, pp. 1659-1668, 2010.

[10] Addeman, B. T., Kutty, S., Perkins, T. G., Soliman, A. S., Wiens, C. N., McCurdy, C. M.*, et al.*, "Validation of volumetric and single-slice MRI adipose analysis using a novel fully automated segmentation method," *Journal of Magnetic Resonance Imaging,* 2014. DOI:10.1002/jmri.24526.

[11] Hu, H. H., Smith, D. L., Nayak, K. S., Goran, M. I., and Nagy, T. R., "Identification of brown adipose tissue in mice with fat–water IDEAL-MRI," *Journal of Magnetic Resonance Imaging,* vol. 31, pp. 1195-1202, 2010.

[12] Hu, H. H., Yin, L., Aggabao, P. C., Perkins, T. G., Chia, J. M., and Gilsanz, V., "Comparison of brown and white adipose tissues in infants and children with chemical-shift-encoded water-fat MRI," *Journal of Magnetic Resonance Imaging,* 2013.

[13] Lall, C. G., Aisen, A. M., Bansal, N., and Sandrasegaran, K., "Nonalcoholic fatty liver disease," *Am J Roentgenol,* vol. 190, pp. 993-1002, 2008.

[14] Hines, C. D. G., Frydrychowicz, A., Hamilton, G., Tudorascu, D. L., Vigen, K. K., Yu, H.*, et al.*, "T1 independent, T2* corrected chemical shift based fat--water separation with multi-peak fat spectral modeling is an accurate and precise measure of hepatic steatosis," *Journal of Magnetic Resonance Imaging,* vol. 33, pp. 873-881, 2011.

[15] Kellman, P., Hernando, D., and Arai, A. E., "Myocardial Fat Imaging," *Current Cardiovascular Imaging Reports,* vol. 3, pp. 83-91, 2010.

[16] Taviani, V., Hernando, D., Francois, C. J., Shimakawa, A., Vigen, K. K., Nagle, S. K.*, et al.*, "Whole-heart chemical shift encoded water–fat MRI," *Magnetic Resonance in Medicine,* vol. 72, pp. 718-725, 2014.

المنارة للاستشارات
www.manaraa.com

[17] Burke, A. P., Farb, A., Tashko, G., and Virmani, R., "Arrhythmogenic Right Ventricular Cardiomyopathy and Fatty Replacement of the Right Ventricular Myocardium Are They Different Diseases?," *Circulation,* vol. 97, pp. 1571-1580, 1998.

[18] Goldfarb, J. W., Roth, M., and Han, J., "Myocardial Fat Deposition after Left Ventricular Myocardial Infarction: Assessment by Using MR Water-Fat Separation Imaging 1," *Radiology,* vol. 253, pp. 65-73, 2009.

[19] Verhagen, S. N. and Visseren, F. L. J., "Perivascular adipose tissue as a cause of atherosclerosis," *Atherosclerosis,* vol. 214, pp. 3-10, 2011.

[20] Bachar, G. N., Dicker, D., Kornowski, R., and Atar, E., "Epicardial Adipose Tissue as a Predictor of Coronary Artery Disease in Asymptomatic Subjects," *Am J Cardiol,* vol. 110, pp. 534-538, 2012.

[21] Bernstein, M. A., King, K. F., and Zhou, X. J., *Handbook of MRI pulse sequences*: Elsevier Academic Press, 2004.

[22] Haacke, E. M., Brown, R. W., Thompson, M. R., and Venkatesan, R., *Magnetic resonance imaging: Physical principles and sequence design*: John Wiley and Sons, 1999.

[23] McRobbie, D. W., Moore, E. A., Graves, M. J., and Prince, M. R., *MRI from Picture to Proton*: Cambridge University Press, 2006.

[24] Bradley, W. G., "MR appearance of hemorrhage in the brain," *Radiology,* vol. 189, pp. 15-26, 1993.

[25] Hernando, D., Levin, Y. S., Sirlin, C. B., and Reeder, S. B., "Quantification of liver iron with MRI: State of the art and remaining challenges," *Journal of Magnetic Resonance Imaging,* 2014. doi:10.1002/jmri.24584.

المنارة للاستشارات
www.manaraa.com

[26] Le-Petross, H., Kundra, V., Szklaruk, J., Wei, W., Hortobagyi, G. N., and Ma, J., "Fast three-dimensional dual echo dixon technique improves fat suppression in breast MRI," *Journal of Magnetic Resonance Imaging,* vol. 31, pp. 889-894, 2010.

[27] Barger, A., DeLone, D., Bernstein, M., and Welker, K., "Fat signal suppression in head and neck imaging using fast spin-echo-IDEAL technique," *American journal of neuroradiology,* vol. 27, pp. 1292-1294, 2006.

[28] Abbara, S., Migrino, R. Q., Sosnovik, D. E., Leichter, J. A., Brady, T. J., and Holmvang, G., "Value of Fat Suppression in the MRI Evaluation of Suspected Arrhythmogenic Right Ventricular Dysplasia," *American Journal of Roentgenology,* vol. 182, pp. 587-591, 2004.

[29] Reeder, S. B., Cruite, I., Hamilton, G., and Sirlin, C. B., "Quantitative assessment of liver fat with magnetic resonance imaging and spectroscopy," *Journal of Magnetic Resonance Imaging,* vol. 34, pp. 729-749, 2011.

[30] Ma, J., "Dixon techniques for water and fat imaging," *Journal of Magnetic Resonance Imaging,* vol. 28, pp. 543-558, 2008.

[31] Reeder, S. B., Markl, M., Yu, H., Hellinger, J. C., Herfkens, R. J., and Pelc, N. J., "Cardiac CINE imaging with IDEAL water-fat separation and steady-state free precession," *Journal of Magnetic Resonance Imaging,* vol. 22, pp. 44-52, 2005.

[32] Reeder, S. B., Pineda, A. R., Wen, Z., Shimakawa, A., Yu, H., Brittain, J. H., *et al.*, "Iterative decomposition of water and fat with echo asymmetry and least-squares estimation (IDEAL): Application with fast spin-echo imaging," *Magnetic resonance in medicine,* vol. 54, pp. 636-644, 2005.

[33] Reeder, S. B., McKenzie, C. A., Pineda, A. R., Yu, H., Shimakawa, A., Brau, A. C., *et al.*, "Water--fat separation with IDEAL gradient-echo imaging," *Journal of Magnetic Resonance Imaging,* vol. 25, pp. 644-652, 2007.

المنارة للاستشارات
www.manaraa.com

[34] Dixon, W. T., "Simple proton spectroscopic imaging," *Radiology,* vol. 153, pp. 189-194, 1984.

[35] Ma, J., "Breath-hold water and fat imaging using a dual-echo two-point dixon technique with an efficient and robust phase-correction algorithm," *Magnetic resonance in medicine,* vol. 52, pp. 415-419, 2004.

[36] Glover, G. H. and Schneider, E., "Three-point dixon technique for true water/fat decomposition with B0 inhomogeneity correction," *Magnetic resonance in medicine,* vol. 18, pp. 371-383, 1991.

[37] Xiang, Q. S. and An, L., "Water-fat imaging with direct phase encoding," *Journal of Magnetic Resonance Imaging,* vol. 7, pp. 1002-1015, 1997.

[38] Reeder, S. B., Wen, Z., Yu, H., Pineda, A. R., Gold, G. E., Markl, M., *et al.*, "Multicoil Dixon chemical species separation with an iterative least-squares estimation method," *Magnetic Resonance in Medicine,* vol. 51, pp. 35-45, 2004.

[39] Yu, H., Reeder, S. B., Shimakawa, A., Brittain, J. H., and Pelc, N. J., "Field map estimation with a region growing scheme for iterative 3-point water-fat decomposition," *Magnetic resonance in medicine,* vol. 54, pp. 1032-1039, 2005.

[40] Lu, W. and Hargreaves, B. A., "Multiresolution field map estimation using golden section search for water-fat separation," *Magnetic Resonance in Medicine,* vol. 60, pp. 236-244, 2008.

[41] Hernando, D., Haldar, J. P., Sutton, B. P., Ma, J., Kellman, P., and Liang, Z. P., "Joint estimation of water/fat images and field inhomogeneity map," *Magnetic Resonance in Medicine,* vol. 59, pp. 571-580, 2008.

[42] Jacob, M. and Sutton, B. P., "Algebraic decomposition of fat and water in MRI," *Medical Imaging, IEEE Transactions on,* vol. 28, pp. 173-184, 2009.

المنارة للاستشارات

www.manaraa.com

[43] Hernando, D., Kellman, P., Haldar, J. P., and Liang, Z. P., "Robust water/fat separation in the presence of large field inhomogeneities using a graph cut algorithm," *Magnetic Resonance in Medicine,* vol. 63, pp. 79-90, 2010.

[44] Lu, W. and Lu, Y., "JIGSAW: joint inhomogeneity estimation via global segment assembly for water-fat separation," *Medical Imaging, IEEE Transactions on,* vol. 30, pp. 1417-1426, 2011.

[45] Berglund, J. and Kullberg, J., "Three-dimensional water/fat separation and T2* estimation based on whole-image optimization - Application in breathhold liver imaging at 1.5 T," *Magnetic Resonance in Medicine,* vol. 67, pp. 1684-1693, 2012.

[46] Tsao, J. and Jiang, Y., "Hierarchical IDEAL: Fast, robust, and multiresolution separation of multiple chemical species from multiple echo times," *Magnetic Resonance in Medicine,* vol. 70, pp. 155-159, 2013.

[47] Pineda, A. R., Reeder, S. B., Wen, Z., and Pelc, N. J., "Cramer--Rao bounds for three-point decomposition of water and fat," *Magnetic resonance in medicine,* vol. 54, pp. 625-635, 2005.

[48] Hernando, D., Hines, C. D. G., Yu, H., and Reeder, S. B., "Addressing phase errors in fat-water imaging using a mixed magnitude/complex fitting method," *Magnetic Resonance in Medicine,* vol. 67, pp. 638–644-638–644, 2012.

[49] Reeder, S. B., Hu, H. H., and Sirlin, C. B., "Proton density fat-fraction: A standardized mr-based biomarker of tissue fat concentration," *Journal of Magnetic Resonance Imaging,* vol. 36, pp. 1011-1014, 2012.

[50] Yu, H., Shimakawa, A., McKenzie, C. A., Brodsky, E., Brittain, J. H., and Reeder, S. B., "Multiecho water-fat separation and simultaneous R 2* estimation with multifrequency fat spectrum modeling," *Magnetic Resonance in Medicine,* vol. 60, pp. 1122-1134, 2008.

المنارة للاستشارات
www.manaraa.com

[51] Szczepaniak, L. S., Babcock, E. E., Schick, F., Dobbins, R. L., Garg, A., Burns, D. K., *et al.*, "Measurement of intracellular triglyceride stores by H spectroscopy: validation in vivo," *American Journal of Physiology-Endocrinology And Metabolism,* vol. 276, pp. E977-E989, 1999.

[52] Brix, G., Heiland, S., Bellemann, M. E., Koch, T., and Lorenz, W. J., "MR imaging of fat-containing tissues: valuation of two quantitative imaging techniques in comparison with localized proton spectroscopy," *Magnetic resonance imaging,* vol. 11, pp. 977-991, 1993.

[53] Ma, J., Wehrli, F., Song, H., and Hwang, S., "A single-scan imaging technique for measurement of the relative concentrations of fat and water protons and their transverse relaxation times," *Journal of Magnetic Resonance,* vol. 125, pp. 92-101, 1997.

[54] Yu, H., McKenzie, C. A., Shimakawa, A., Vu, A. T., Brau, A., Beatty, P. J., *et al.*, "Multiecho reconstruction for simultaneous water-fat decomposition and T2* estimation," *Journal of Magnetic Resonance Imaging,* vol. 26, pp. 1153-1161, 2007.

[55] Reeder, S. B., Bice, E. K., Yu, H., Hernando, D., and Pineda, A. R., "On the performance of T2* correction methods for quantification of hepatic fat content," *Magnetic Resonance in Medicine,* vol. 67, pp. 389-404, 2012.

[56] Chebrolu, V. V., Hines, C. D. G., Yu, H., Pineda, A. R., Shimakawa, A., McKenzie, C. A., *et al.*, "Independent estimation of T*2 for water and fat for improved accuracy of fat quantification," *Magnetic Resonance in Medicine,* vol. 63, pp. 849-857, 2010.

[57] Horng, D. E., Hernando, D., Hines, C. D. G., and Reeder, S. B., "Comparison of R2* correction methods for accurate fat quantification in fatty liver," *Journal of Magnetic Resonance Imaging,* vol. 37, pp. 414-422, 2013.

المنارة للاستشارات
www.manaraa.com

[58] Kühn, J.-P., Jahn, C., Hernando, D., Siegmund, W., Hadlich, S., Mayerle, J.*, et al.*, "T1 bias in chemical shift-encoded liver fat-fraction: Role of the flip angle," *Journal of Magnetic Resonance Imaging,* vol. 40, pp. 875-883, 2014.

[59] Yokoo, T., Bydder, M., Hamilton, G., Middleton, M. S., Gamst, A. C., Wolfson, T.*, et al.*, "Nonalcoholic Fatty Liver Disease: Diagnostic and Fat-Grading Accuracy of Low-Flip-Angle Multiecho Gradient-Recalled-Echo MR Imaging at 1.5 T 1," *Radiology,* vol. 251, pp. 67-76, 2009.

[60] Liu, C. Y., McKenzie, C. A., Yu, H., Brittain, J. H., and Reeder, S. B., "Fat quantification with IDEAL gradient echo imaging: correction of bias from T1 and noise," *Magnetic Resonance in Medicine,* vol. 58, pp. 354-364, 2007.

[61] Yang, I. Y., Cui, Y., Wiens, C. N., Wade, T. P., Friesen-Waldner, L. J., and McKenzie, C. A., "Fat fraction bias correction using T1 estimates and flip angle mapping," *Journal of Magnetic Resonance Imaging,* vol. 39, pp. 217-223, 2014.

[62] Johnson, B. L., Schroeder, M. E., Wolfson, T., Gamst, A. C., Hamilton, G., Shiehmorteza, M.*, et al.*, "Effect of flip angle on the accuracy and repeatability of hepatic proton density fat fraction estimation by complex data-based, T1-independent, T2*-corrected, spectrum-modeled MRI," *Journal of Magnetic Resonance Imaging,* vol. 39, pp. 440-447, 2014.

[63] Yu, H., Shimakawa, A., Hines, C. D., McKenzie, C. A., Hamilton, G., Sirlin, C. B.*, et al.*, "Combination of complex-based and magnitude-based multiecho water-fat separation for accurate quantification of fat-fraction," *Magnetic resonance in medicine,* vol. 66, pp. 199-199, 2011.

[64] Wade, T. P., Wiens, C. N., and McKenzie, C. A., "Eddy Current Compensated IDEAL," in *Proc. Intl. Soc. Mag. Reson. Med*, 2013, p. 549.

[65] Hernando, D., Sharma, S. D., Kramer, H., and Reeder, S. B., "On the confounding effect of temperature on chemical shift-encoded fat quantification," *Magnetic Resonance in Medicine,* pp. n/a-n/a, 2013.

المنارة للاستشارات
www.manaraa.com

[66] Griswold, M. A., Jakob, P. M., Heidemann, R. M., Nittka, M., Jellus, V., Wang, J., *et al.*, "Generalized autocalibrating partially parallel acquisitions (GRAPPA)," *Magnetic Resonance in Medicine,* vol. 47, pp. 1202-1210, 2002.

[67] Bydder, M., Larkman, D. J., and Hajnal, J. V., "Generalized SMASH imaging," *Magnetic resonance in medicine,* vol. 47, pp. 160-170, 2002.

[68] Deshmane, A., Gulani, V., Griswold, M. A., and Seiberlich, N., "Parallel MR imaging," *Journal of Magnetic Resonance Imaging,* vol. 36, pp. 55-72, 2012.

[69] Sodickson, D. K. and Manning, W. J., "Simultaneous acquisition of spatial harmonics (SMASH): fast imaging with radiofrequency coil arrays," *Magnetic Resonance in Medicine,* vol. 38, pp. 591-603, 1997.

[70] Pruessmann, K. P., Weiger, M., Scheidegger, M. B., and Boesiger, P., "SENSE: Sensitivity encoding for fast MRI," *Magnetic Resonance in Medicine,* vol. 42, pp. 952-962, 1999.

[71] Pruessmann, K. P., Weiger, M., Börnert, P., and Boesiger, P., "Advances in sensitivity encoding with arbitrary k-space trajectories," *Magnetic Resonance in Medicine,* vol. 46, pp. 638-651, 2001.

[72] Boykov, Y. and Veksler, O., "Graph cuts in vision and graphics: Theories and applications," *Handbook of Mathematical Models in Computer Vision, Springer-Verlag,* pp. 79-96, 2006.

[73] Boykov, Y., Veksler, O., and Zabih, R., "Fast approximate energy minimization via graph cuts," *IEEE Transactions on pattern analysis and machine intelligence,* pp. 1222-1239, 2001.

[74] Yuan, J., Bae, E., and Tai, X. C., "A study on continuous max-flow and min-cut approaches," presented at the In Proceedings of IEEE Conf. on Computer Vision and Pattern Recognition (CVPR), San Francisco, CA 2010.

المنارة للاستشارات
www.manaraa.com

[75] Ukwatta, E., Yuan, J., Rajchl, M., Qiu, W., Tessier, D., and Fenster, A., "3-D carotid multi-region MRI segmentation by globally optimal evolution of coupled surfaces," *Medical Imaging, IEEE Transactions on,* vol. 32, pp. 770-785, 2013.

[76] Nambakhsh, C., Yuan, J., Punithakumar, K., Goela, A., Rajchl, M., Peters, T. M., *et al.*, "Left ventricle segmentation in MRI via convex relaxed distribution matching," *Medical image analysis,* vol. 17, pp. 1010-1024, 2013.

[77] Miles, B., "Image Fusion and Axial Labeling of the Spine," 2014.

[78] Rajchl, M., Jing, Y., White, J. A., Ukwatta, E., Stirrat, J., Nambakhsh, C. M. S., *et al.*, "Interactive Hierarchical-Flow Segmentation of Scar Tissue From Late-Enhancement Cardiac MR Images," *Medical Imaging, IEEE Transactions on,* vol. 33, pp. 159-172, 2014.

المنارة للاستشارات

www.manaraa.com

"The significant problems we have cannot be solved at the same level of thinking we were at when we created them"
- Einstein

Chapter 2

A Convex Relaxation Approach to Water/Fat Separation with Minimum Label Description[1]

2.1 Introduction

The ability to separate fat from water in a magnetic resonance (MR) image is an important problem for a number of clinical applications. Bright fat signal can obscure underlying pathology and therefore suppression of the fat signal is required. In other cases, fat is considered an important diagnostic marker, and hence a clearer depiction of its signal, rather than its suppression, is desired.

[1] This chapter is adapted from a peer-reviewed article published in *Springer Lecture Notes in Computer Sciences* of *Medical Image Computing and Computer-Assisted Intervention (MICCAI)* 2012: Soliman, A. S., Yuan, J., White, J. A., Peters, T. M., and McKenzie, C. A., "A Convex Relaxation Approach to Fat/Water Separation with Minimum Label Description," Medical Image Computing and Computer-Assisted Intervention – MICCAI, LNCS 7511, pp. 519-526 (2012).

المنارة للاستشارات
www.manaraa.com

Common clinical applications of the latter include the diagnosis of non-alcoholic fatty liver diseases (NAFLD) [1, 2], as well as a variety of bone marrow diseases [3]. However, expanding interest in the evaluation of myocardial fat infiltration [4] and pericardial fat volume [5-7] justifies its optimization for cardiac imaging.

Among various available MR techniques, chemical-shift based (or Dixon-based) techniques [8] have become the most commonly used methods to obtain a quantitative fat measurement [9]. Chemical-shift based methods are characterized by their unique ability to extract a fat-only image with positive contrast, unlike other techniques that either tend to suppress the fat signal, making the process of identifying fat voxels ambiguous, or apply fat selective excitation which is sensitive to B0 and B1 inhomogeneities.

Unfortunately, a successful water/fat separation with Dixon-based techniques relies largely on the homogeneity of the magnetic field. In other words, the mapping of the magnetic field inhomogeneities – so called field map, cannot be decoupled from the water/fat separation process (see Sec 2.2.1). The field map estimation problem therefore, leads to a non-linear non-convex optimization problem, which has multiple local minima. An error in estimating the field map would propagate to the resultant water and fat images, causing what we term water/fat swaps. A “swap” is defined as assigning the main signal in a water-dominant voxel as fat, or vice-versa - an example of water/fat swaps is shown in Figure 2.1.

المنارة للاستشارات
www.manaraa.com

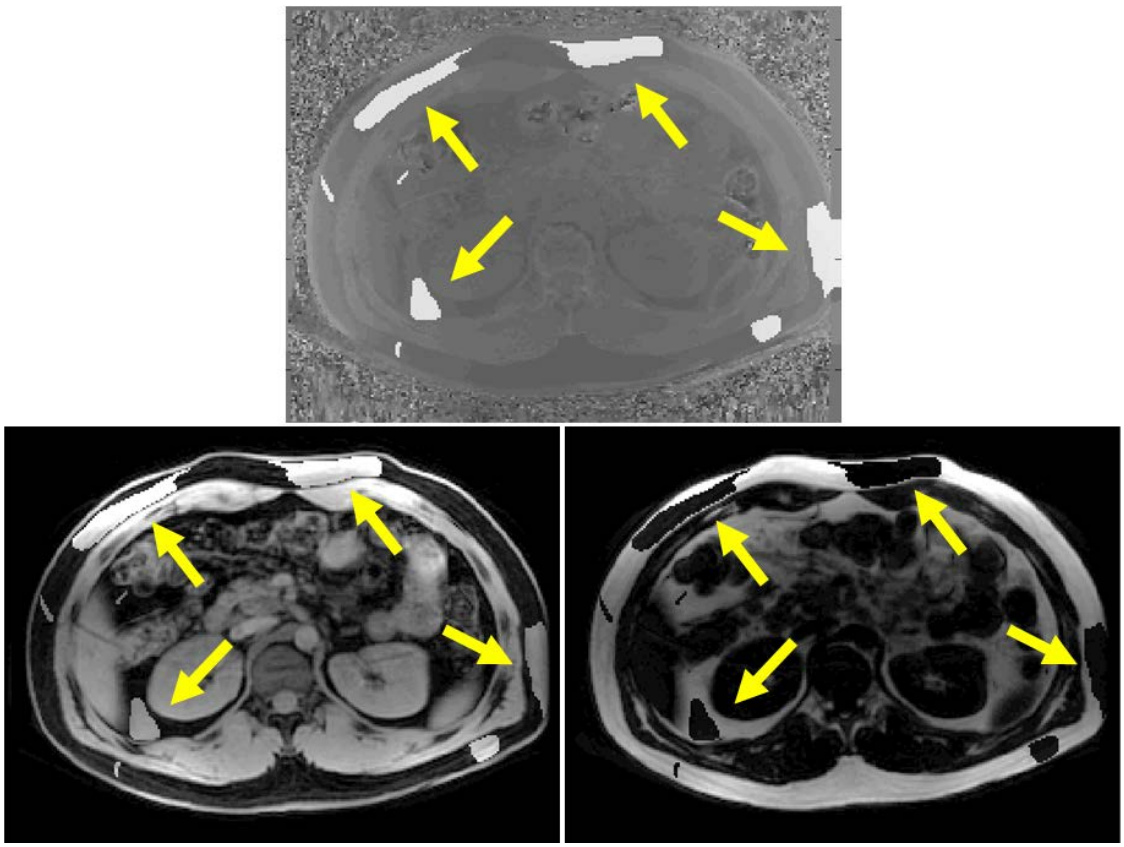

Figure 2.1: Water/fat swaps appearing in field map (top), water (left) and fat components (right)

المنارة للاستشارات
www.manaraa.com

The commonly-used technique in water/fat separation is the "Iterative Decomposition of water and fat with Echo Asymmetry and Least square estimation", abbreviated as IDEAL [10]. IDEAL is a Dixon-based method that acquires at least three echoes to estimate the field map, water and fat components. However, IDEAL is a local optimization method that heavily depends on the initialization process, and hence, convergence to the global optimum is not guaranteed. Moreover, it is a voxel-independent optimization, i.e. it does not enforce any global smoothness prior to the estimated field map. Yu et al. [11] proposed a region-growing technique to address the flaws of IDEAL. This method implicitly imposes a spatial smoothness on the field map; however, it does not account for the abrupt changes in magnetic field that might exist at tissue/air interfaces, which might cause water/fat swaps. Although several techniques have been proposed in the literature [11-17] to address the field map estimation problem, only a few have been considered sufficiently robust for clinical use [4, 13]. Further, their application has been limited to 1.5 Tesla [4] where B0 field inhomogeneities are modest compared to higher field strengths.

In this work, we propose a novel field map estimation approach that can withstand abrupt changes in field homogeneity at higher field strengths, particularly at 3.0 Tesla, while guaranteeing smoothness of the estimated field map. Our method relies on prior knowledge of the periodic variation of signal residuals with the field map values [11-13]. We use a two-stage approach to reach the global minimum solution, and provide a high resolution mapping of the field inhomogeneities. First, a label-cost prior max-flow approach [18] is performed on the signal residues to converge near the global optimum. The output is employed as an initial guess to the second stage, where a conventional gradient-descent IDEAL is applied to reach the exact field offset. Our method is tested for cardiac as well as abdominal images obtained at 3.0 Tesla, where challenging B0 field inhomogeneities commonly exist. Compared to the region growing method [11], our approach has significantly improved the robustness of field map estimation process and has efficiently removed water/fat swaps.

المنارة للاستشارات
www.manaraa.com

2.2 Theory and Methodology

In the following sections, we first derive the signal equation to be minimized; then we introduce the multi-labeling convex relaxation model and its dual continuous max-flow formulation along with the minimum description length (MDL) principle, which are applied in the first stage of our approach. The proposed MDL-based labeling model penalizes the number of "appearing" labels, which helps to avoid the small regional water/fat swaps that might appear in the presence of severe and rapid changes of magnetic field. In other words, such MDL prior smooth out small-scale partitions, which usually correspond to regional water/fat swaps. The MDL-based labeling model results in a coarse estimation of the field map. This step guarantees a global minimization by labeling each pixel with a field map value located near its global optimum solution. The coarse estimate of field map serves as an initial guess for the second stage that consists of applying the IDEAL iterative process [10, 19]. A stopping criterion of < 1 Hz was used for the iterative process, in order to provide a field map with a sufficient resolution for clinical applications, particularly pericardial fat quantification. Once the final field map is obtained, water and fat components can be directly computed from Equation 2.2

2.2.1 Signal Equation

Let $S(.)$ denote the signal acquired from a voxel v, containing a mixture of water and fat, such that:

$$S_v(t_n) = \left(\rho_{W,v} + \rho_{F,v} \cdot \sum_{m=1}^{M} \alpha_m . e^{i2\pi\, \delta_m\, t_n}\right) . e^{i2\pi\, \varphi_v\, t_n}\,, \tag{2.1}$$

where t_n denotes the echo-time (TE) shift ($n = 1, \dots, N$) of the acquired signal; $\rho_{W,v}$ and $\rho_{F,v}$ are the water and fat components at voxel v, respectively; M is the number of fat peaks in the fat spectrum; δ_m is the frequency of the m-th peak with its corresponding amplitude α_m (Hz), such that $\sum_{m=1}^{M} \alpha_m = 1$; φ_v (Hz) is the local

المنارة للاستشارات
www.manaraa.com

frequency offset at voxel v (i.e. the field map). We used a calibrated fat spectrum model as shown in [20], where $M = 6$ and the main fat peak is at ~ 420 Hz, relative to the water peak at 3.0 Tesla. Having three or more echo-times (TE) acquired (as described above), Equation 2.1 can be reformulated as follows:

$$\mathrm{S}_v(t) = \Psi(\varphi_v, t)\,.\ \mathrm{A}(t)\,.\ \mathrm{P}_v\ , \tag{2.2}$$

where

$$\Psi(\varphi_v) = \begin{bmatrix} e^{i2\pi\,\varphi_v\,t_1} & 0 & 0 \\ 0 & \ddots & 0 \\ 0 & 0 & e^{i2\pi\,\varphi_v\,t_N} \end{bmatrix},\ \mathrm{A} = \begin{bmatrix} 1 & \sum_{m=1}^{M} \alpha_m . e^{i2\pi\,\delta_m\,t_1} \\ \vdots & \vdots \\ 1 & \sum_{m=1}^{M} \alpha_m . e^{i2\pi\,\delta_m\,t_N} \end{bmatrix},$$

$\mathrm{S}_v(t) = [S_v(t_1), \dots\ S_v(t_n)]^T$, $\mathrm{P}_v = \left[\rho_{W,v},\ \rho_{F,v}\right]^T$. To estimate the required water and fat components $(\rho_{W,v},\ \rho_{F,v})$, the frequency offset φ_v should be demodulated first. Hence, dropping the known echo-time shift (t_n), a non-linear least-squares cost function can be derived from Equation 2.2 as follows:

$$\Gamma(\varphi_v) \coloneqq \left\|\mathrm{A}\,.\,\widehat{\mathrm{P}_v}\ - \widehat{\Psi}^{-1}(\varphi_v)\,.\,\mathrm{S}_v\right\|_2$$

$$\Gamma(\varphi_v) \coloneqq \left\|(\mathrm{AA}^{\dagger} - I)\ \widehat{\Psi}^{-1}(\varphi_v).\mathrm{S}_v\right\|_2\ , \tag{2.3}$$

where $\widehat{\mathrm{P}_v}$ and $\widehat{\Psi}(\varphi_v)$ are the estimated values of P_v and $\Psi(\varphi_v)$ respectively, I is the identity matrix, and † denotes the pseudo-inverse, $s.t.\,\mathrm{A}^{\dagger} = [\mathrm{A}^T\mathrm{A}]^{-1}\mathrm{A}^T$. However, two main problems are encountered when minimizing $\Gamma(\varphi_v)$: first, the non-convex property of the function, and second, it does not impose a priori smoothness on the estimated field map, as it is a voxel-by-voxel based strategy, and global minimization is not guaranteed.

المنارة للاستشارات
www.manaraa.com

2.2.2 The Potts Model

In image processing, a multi-labeling problem assigns the optimal label $\varphi \in \varphi_1 \dots \varphi_L$ to each voxel. The Potts model is a labeling approach that minimizes the total perimeter of all one-label regions, without assuming any prior order for the labels. It results in a partition of the continuous domain Ω into L disjoint subdomains $\{\Omega_i\}_{i=1}^{L}$, as follows:

$$\min_{\{\Omega_i\}_{i=1}^{L}} \sum_{i=1}^{L} \int_{\Omega_i} \Gamma(\varphi_i, x)\, dx \; + \lambda \sum_{i=1}^{L} |\partial\Omega_i| \tag{2.4}$$

$$s.t. \bigcup_{i=1}^{L} \Omega_i = \Omega, \;\; \text{and} \;\; \Omega_k \bigcap \Omega_m = \emptyset, \qquad \forall k \neq m$$

where $\Gamma(\varphi_i, x)$ is the cost of assigning label φ_i to location x, as defined in Equation 2.3, $\emptyset$ denotes an empty set, and $|\partial\Omega_i|$ measures the perimeter of each subdomain Ω_i , $i = 1, \dots, L$.

The Potts model in Equation 2.4 can be efficiently solved by its convex-relaxation model as follows [21]:

$$\min_{u \in S} \left\{ \mathrm{E}(u) \coloneqq \sum_{i=1}^{L} \left(\int_{\Omega} u_i(x)\, \Gamma(\varphi_i, x)\, dx \; + \beta \int_{\Omega} |\nabla u_i| \; dx \right) \right\} \tag{1.5}$$

where S is the convex constrained set of $u(x) \coloneqq \big(u_1(x), \dots, u_L(x)\big)$:

$$S = \left\{ u(x) \mid \sum_{i=1}^{L} u_i(x) = 1, \quad \forall x \in \Omega\,; \quad u_i(x) \in [0,1], \quad i = 1, \dots, L \right\}$$

المنارة للاستشارات
www.manaraa.com

2.2.3 Minimum Description Length (MDL)-Based Potts Model

The minimum description length (MDL) principle penalizes the number of appearances or labels in image labeling problems. It naturally leads to the use of fewer partitions or labels to describe the given image, without simultaneously over smoothing the underlying domain [18]. The MDL cost is introduced by adding the term γZ to the Potts model, where γ is a constant and $Z = \#\{1 \leq i \leq L \mid \Omega_i \neq \emptyset\}$ gives the number of non-empty labels, i.e. a label-cost prior. Yuan *et al.* [18] showed that adding the label-cost prior to Equation 2.5 leads to the following convex-relaxed MDL-based Potts model, used here:

$$\min_{u \in S} \left\{ \mathrm{E}(u) := \sum_{i=1}^{L} \left(\int_{\Omega} u_i(x)\, \Gamma(\varphi_i, x)\, dx + \beta \int_{\Omega} |\nabla u_i|\, dx \right) \right\} + \gamma \sum_{i=1}^{L} \max_{x \in \Omega} u_i(x) \qquad (2.6)$$

2.2.4 A Fast Continuous Max-Flow Approach to MDL-based Potts Model

The continuous max-flow approach [21, 22] to the MDL-based Potts model (Equation 2.6) used in this study is summarized below:

Let Ω be a continuous 2D image domain, L the number of labels, and $\Omega_i,\ i = 1, \dots L$ a copy of Ω assigned to the ith label. For each location $x \in \Omega$, a source flow $\rho_s(x)$ is streaming from the source node s to a labeled copy Ω_i, $s.t.\ \forall\, \Omega_i,\ i = 1, \dots L,\ \rho_s(x)$ is the same. Similarly for each $x \in \Omega$, a sink flow to the sink t is assigned. However, $\rho_i(x), i = 1, \dots L$ may differ. A spatial flow $q_i(x)\ i = 1, \dots L$ is also defined for each location. The continuous max-flow model can be formulated as follows:

$$\max_{\rho_s, \rho, q} \left\{ P(\rho_s, \rho, q) := \int_{\Omega} \rho_s\, dx \right\}, \qquad (2.7)$$

subject to the constraints:

المنارة للاستشارات
www.manaraa.com

a. $(\operatorname{div} q_i - \rho_s + \rho_i - r_i)(x) = 0, \qquad i = 1, \dots, L$

b. $|q_i(x)| \le C_i(x), \;\; \rho_i(x) \le \Gamma(\varphi_i, x), \;\; \int_\Omega |r_i(x)|\, dx \le \gamma \qquad i = 1, \dots, L,$

where $C_i(x) = \beta$ is the capacity of the spatial flow $q_i(x)$, and $r_i(x)$ is the extra flow associated with the penalty of the number of labels. Yuan *et al.* [18] proved that the max-flow formulation (Equation 2.7) is dual to the convex-relaxed MDL-based Potts model, and results in an efficient flow maximization algorithm to Equation 2.6.

2.3 Experiments

Our method was tested on 19 abdominal and cardiac images acquired on a 3.0 T MRI system (Discovery MR 750, GE Healthcare, Waukesha, WI). Cardiac images were acquired in different orientations (short-axis, 4-chambers and axial views) with a fast multi-echo GRE sequence using a 32-coil cardiac array [23]. Abdominal images were acquired with a 3D IDEAL-SPGR sequence [20] using an 8-coil array. Four and 6 equally-spaced echo-time shifts were used (interleaved acquisition for cardiac data). Each cardiac slice is acquired in one ~20s breath-hold while the 8 abdominal slices were acquired with parallel MRI acquisition (acceleration factor of 2) in one ~20s breath-hold. Matrix sizes of acquired images varied between 256x256 and 256x192.

The field map estimated from the first and final stages of our approach, as well as the fat and water components are shown below (Figure 2.2). For the abdominal example, TE/ΔTE = 1.04/0.828 msec and TR = 7.324 msec; for the cardiac example, TE/ΔTE = 2.28/1.54 msec and TR = 12.66 msec.

Our results are compared to those obtained from the region-growing technique [11] on the same dataset, to show that water/fat swaps have been significantly reduced (Figure 2.3). A major drawback in the region-growing method is that it forces the field map smoothness using a 2D extrapolation approach, which does not account for the abrupt changes of field homogeneity, in particular in cardiac images. We

المنارة للاستشارات
www.manaraa.com

have tackled this problem by employing a convex-relaxed labeling model that guarantees the global optimum. Moreover, it implicitly imposes smoothness on the estimated field map by penalizing small partitions, which correspond to regional water/fat swaps.

The processing time of our method is 1.5-5 minutes per image, depending on the level of smoothness and the underlying degree of inhomogeneities, compared to 6.5 minutes per image for the region-growing method. Moreover, the max-flow stage can be easily accelerated over modern computation frameworks, e.g. graphics processing units (GPU).

المنارة للاستشارات
www.manaraa.com

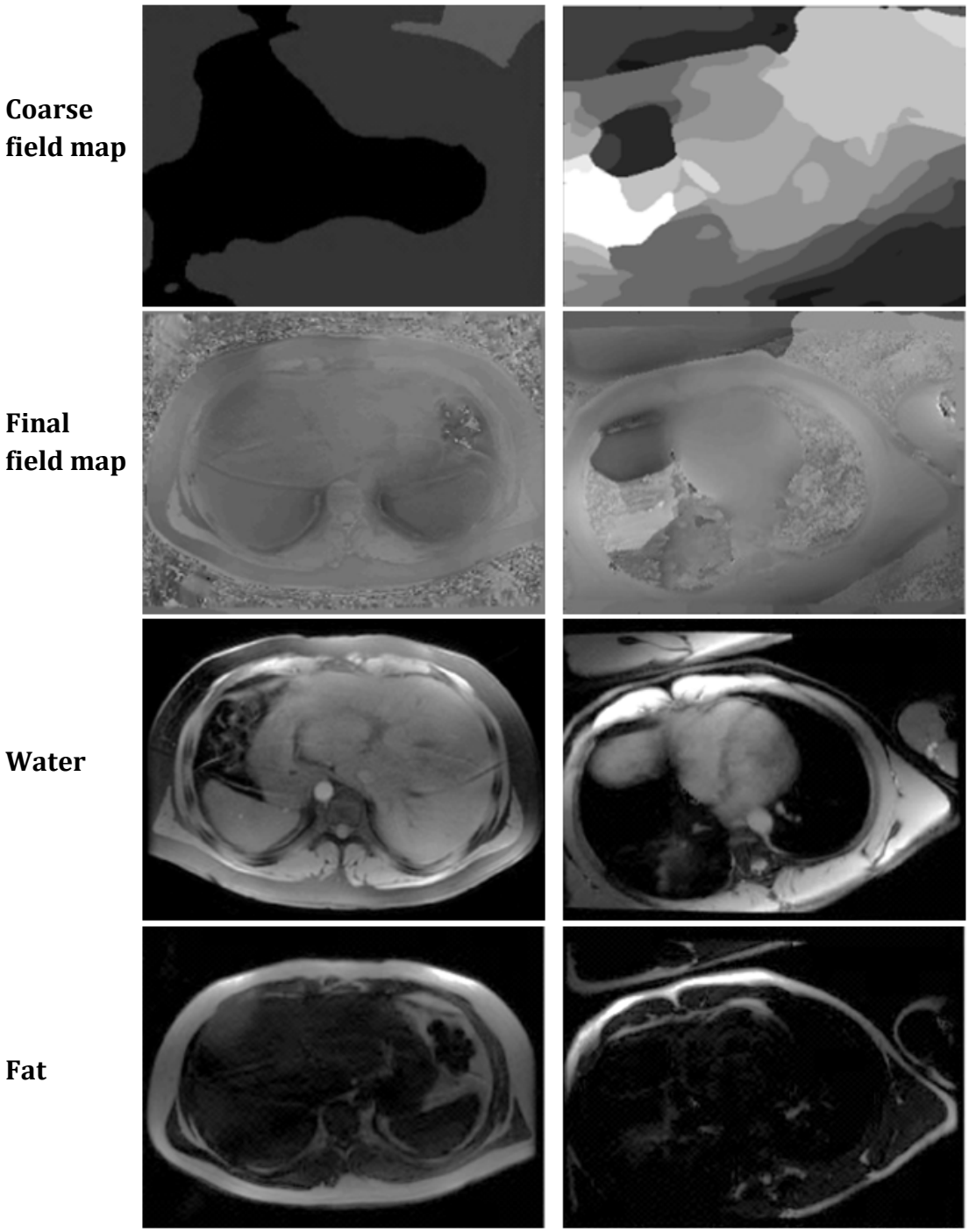

Figure 2.2: Left column: axial abdominal slice, Right column 4-chambers cardiac view. Top to bottom: the coarse estimate of field map from the max-flow stage, final field map after the second stage, water and fat components

المنارة للاستشارات
www.manaraa.com

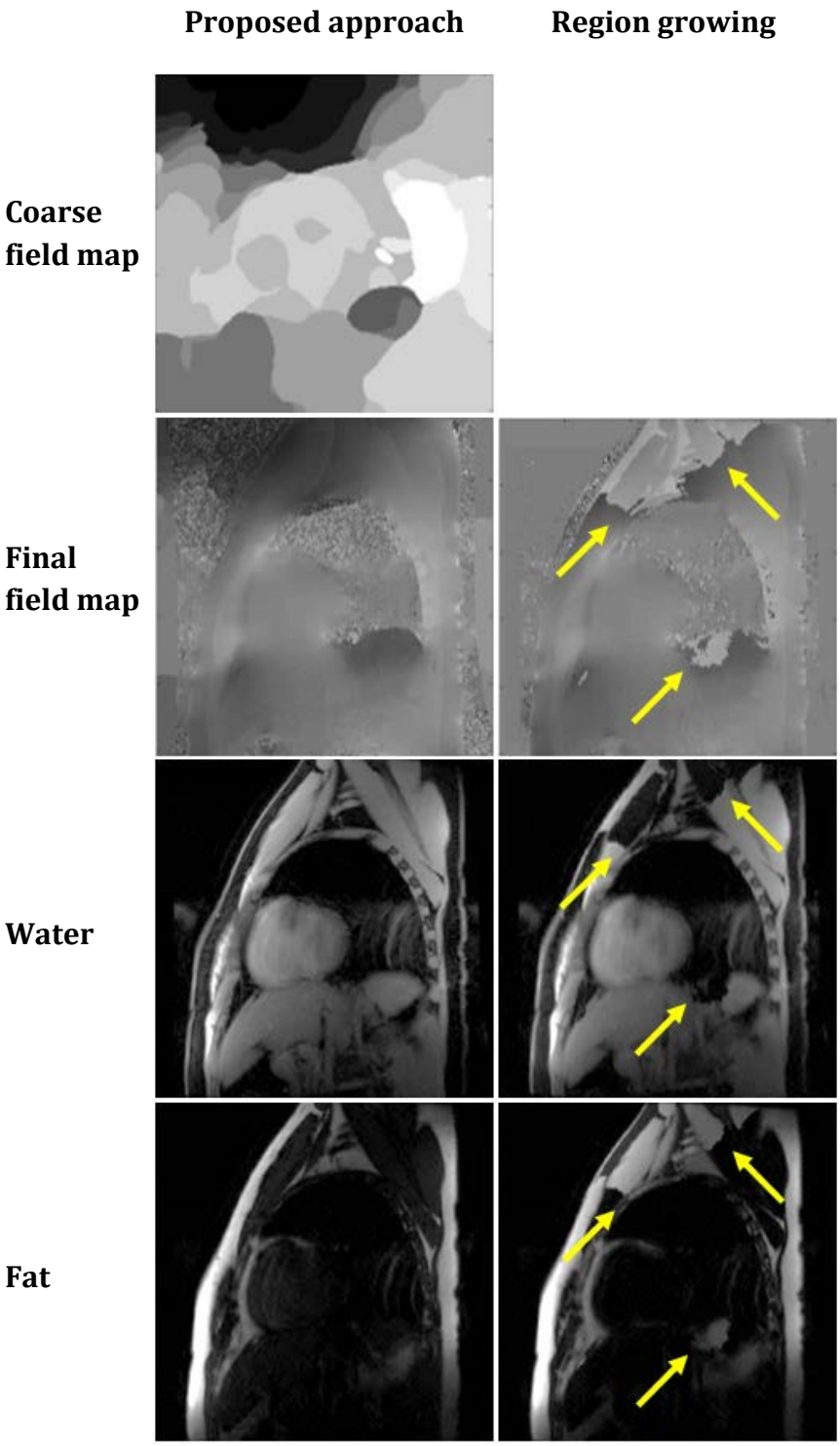

Figure 2.3: Comparison between our approach (left column) and the region-growing method (right column) on a short-axis cardiac image. Yellow arrows indicate the locations of water/fat swaps that have clearly avoided by our method.

المنارة للاستشارات
www.manaraa.com

2.4 Discussion

The robustness of field map estimation techniques is usually judged by the visual identification of water/fat swaps. However, we provide an approximate metric for the effectiveness of the technique by counting the number of pixels that have shown water/fat swaps in a user-defined region of interest – In abdominal images, the liver is assumed to be the region of interest, while in cardiac images the whole intra-thoracic space including the area surrounding the diaphragm is considered. An approximate average for the pixels showing water/fat swaps is ~274 $\pm$ 720 pixels with the region-growing technique vs. ~17 $\pm$ 32 pixels with our proposed method.

Taking into account the periodicity of $\Gamma(\varphi)$ [11, 12] (i.e. $\pm$ 1/ (2ΔTE)), we found that using 20 equally-spaced field offsets for the first stage is sufficient to target the optimal label. However, relying only on the max-flow stage to reach the exact field offset would significantly increase the processing time, as we would use up to ~800 labels in order to achieve the same high resolution field map.

Comparing to a recent graph cut-based technique [13] currently used in clinical applications [4], our approach provides a field map with higher frequency resolution, with an estimation error less than 1 Hz over the whole image. This may have important utility for supporting accurate myocardial and pericardial fat quantification, given an expanding use of 3.0 Tesla field strengths for cardiac imaging.

المنارة للاستشارات
www.manaraa.com

Acknowledgments

We acknowledge funding from CIHR Strategic Training Program for Vascular Research, and Ontario Research Fund: Imaging for Cardiovascular therapeutics. This research was undertaken, in part, thanks to funding from the Canada Research Chairs program. We thank Karl K. Vigen for providing cardiac IDEAL pulse sequence, Curtis Wiens for helping in data acquisition, and Bryan Addeman for the revision of the manuscript. We acknowledge the use of the Fat-Water Toolbox (http://ismrm.org/workshops/FatWater12/data.htm) for some of the experiments.

المنارة للاستشارات
www.manaraa.com

References

[1] Alfire, M. E. and Treem, W. R., "Nonalcoholic fatty liver disease," *Pediatr Ann,* vol. 35, pp. 290-4, 297-9, Apr 2006.

[2] Lall, C. G., Aisen, A. M., Bansal, N., and Sandrasegaran, K., "Nonalcoholic fatty liver disease," *American Journal of Roentgenology,* vol. 190, pp. 993-1002, 2008.

[3] Haavardsholm, E. A., Bøyesen, P., Østergaard, M., Schildvold, A., and Kvien, T. K., "Magnetic resonance imaging findings in 84 patients with early rheumatoid arthritis: bone marrow oedema predicts erosive progression," *Annals of the rheumatic diseases,* vol. 67, pp. 794-800, 2008.

[4] Kellman, P., Hernando, D., and Arai, A. E., "Myocardial Fat Imaging," *Current Cardiovascular Imaging Reports,* vol. 3, pp. 83-91, 2010.

[5] Iozzo, P., "Myocardial, Perivascular, and Epicardial Fat," *Diabetes Care,* vol. 34, pp. S371-S371, 2011.

[6] Bachar, G. N., Dicker, D., Kornowski, R., and Atar, E., "Epicardial Adipose Tissue as a Predictor of Coronary Artery Disease in Asymptomatic Subjects," *Am J Cardiol,* vol. 110, pp. 534-538, 2012.

[7] Verhagen, S. N. and Visseren, F. L. J., "Perivascular adipose tissue as a cause of atherosclerosis," *Atherosclerosis,* vol. 214, pp. 3-10, 2011.

[8] Ma, J., "Dixon techniques for water and fat imaging," *Journal of Magnetic Resonance Imaging,* vol. 28, pp. 543-558, 2008.

[9] Hines, C. D. G., Frydrychowicz, A., Hamilton, G., Tudorascu, D. L., Vigen, K. K., Yu, H., *et al.*, "T1 independent, T2* corrected chemical shift based fat-water separation with multi-peak fat spectral modeling is an accurate and precise

المنارة للاستشارات
www.manaraa.com

measure of hepatic steatosis," *J Magn Reson Imaging,* vol. 33, pp. 873-881, 2011.

[10] Reeder, S. B., Pineda, A. R., Wen, Z., Shimakawa, A., Yu, H., Brittain, J. H., *et al.*, "Iterative decomposition of water and fat with echo asymmetry and least-squares estimation (IDEAL): Application with fast spin-echo imaging," *Magnetic resonance in medicine,* vol. 54, pp. 636-644, 2005.

[11] Yu, H., Reeder, S. B., Shimakawa, A., Brittain, J. H., and Pelc, N. J., "Field map estimation with a region growing scheme for iterative 3-point water-fat decomposition," *Magnetic resonance in medicine,* vol. 54, pp. 1032-1039, 2005.

[12] Lu, W. and Hargreaves, B. A., "Multiresolution field map estimation using golden section search for water-fat separation," *Magnetic Resonance in Medicine,* vol. 60, pp. 236-244, 2008.

[13] Hernando, D., Kellman, P., Haldar, J. P., and Liang, Z. P., "Robust water/fat separation in the presence of large field inhomogeneities using a graph cut algorithm," *Magnetic Resonance in Medicine,* vol. 63, pp. 79-90, 2010.

[14] Soliman, A. S., Yuan, J., Vigen, K. K., White, J. A., Peters, T. M., and McKenzie, C. A., "Robust Field Map Estimation using VARPRO and Multi-labeling Continuous Max-Flow," presented at the In Proceedings of the 20th Annual Meeting of ISMRM, Melbourne, Australia 2012.

[15] Soliman, A. S., Yuan, J., Vigen, K. K., White, J. A., Peters, T. M., and McKenzie, C. A., "Fast Field Map Estimation with Multi-labeling Continuous Max-Flow," presented at the In Proceedings of ISMRM Workshop on Fat-Water Separation, Long Beach, CA, 2012.

[16] Berglund, J., Johansson, L., Ahlström, H., and Kullberg, J., "Three-point dixon method enables whole-body water and fat imaging of obese subjects," *Magn Reson Med,* vol. 63, pp. 1659-1668, 2010.

المنارة للاستشارات

www.manaraa.com

[17] Hernando, D., Haldar, J. P., Sutton, B. P., Ma, J., Kellman, P., and Liang, Z. P., "Joint estimation of water/fat images and field inhomogeneity map," *Magn Reson Med,* vol. 59, pp. 571-580, 2008.

[18] Yuan, J., Bae, E., Boykov, Y., and Tai, X.-C., "A continuous max-flow approach to minimal partitions with label cost prior," in *Scale Space and Variational Methods in Computer Vision*, ed: Springer, 2012, pp. 279-290.

[19] Reeder, S. B., Wen, Z., Yu, H., Pineda, A. R., Gold, G. E., Markl, M., *et al.*, "Multicoil Dixon chemical species separation with an iterative least-squares estimation method," *Magnetic Resonance in Medicine,* vol. 51, pp. 35-45, 2004.

[20] Yu, H., Shimakawa, A., McKenzie, C. A., Brodsky, E., Brittain, J. H., and Reeder, S. B., "Multiecho water-fat separation and simultaneous R 2* estimation with multifrequency fat spectrum modeling," *Magnetic Resonance in Medicine,* vol. 60, pp. 1122-1134, 2008.

[21] Yuan, J., Bae, E., Tai, X. C., and Boykov, Y., "A continuous max-flow approach to potts model," presented at the In Proceedings of the 11th European Conference on Computer Vision (ECCV), Crete, Greece, 2010.

[22] Yuan, J., Bae, E., and Tai, X. C., "A study on continuous max-flow and min-cut approaches," presented at the In Proceedings of IEEE Conf. on Computer Vision and Pattern Recognition (CVPR), San Francisco, CA 2010.

[23] Vigen, K. K., Francois, C., Yu, H., Shimakawa, A., Brittain, J. H., and Reeder, S. B., "Multi-Echo IDEAL Cardiac Water--Fat Imaging," in *Proceedings of the 17th Annual Meeting of ISMRM, Honolulu, HI*, 2009, pp. 2775-2775.

المنارة للاستشارات

www.manaraa.com

"Wherever you go, go with all your heart"
- Confucius

Chapter 3

Max-IDEAL: A Max-Flow Based Approach to IDEAL Water /Fat Separation[1]

3.1 Preface

In the previous chapter we introduced a new convex relaxation approach to address the field map estimation problem. The technique does not rely on spatial-smoothness constraints as previous methods; however a unique global smoothness constraint is employed to estimate the inhomogeneities. Although successful

[1] This chapter is adapted from a peer-reviewed article published in *Magnetic Resonance in Medicine*: Soliman, A.S., Yuan, J., Vigen, K.K., White, J.A., Peters, T.M., and McKenzie, C.A. "Max-IDEAL: A max-flow based approach for IDEAL water/fat separation." Magnetic Resonance in Medicine 72(2): 510-521, 2014.

المنارة للاستشارات
www.manaraa.com

water/fat separation was obtained in most cases, few challenges need yet to be addressed:

i. There are several points related to the T_2^* decay of the signal:

   a) It was shown that the T_2^* decay affects the accuracy of the quantification. Although the inclusion of T_2^* decay has been previously demonstrated in the literature [1] (T_2^*-IDEAL), the effect of including T_2^* decay in the labeling stage needs yet to be explored.

   b) The initial estimate of the field map produced by the first stage neglects the T_2^* decay. We hypothesize that the inclusion of T_2^* decay will increase the robustness of estimating the initial guess of the labeling stage.

   c) For each voxel, there is a certain field map value as well as a combined T_2^* decay for both water and fat components. Up to 50 discrete values of field map might be used in the labeling stage. Extending the same concept of labeling for the T_2^* decay, additional 5-10 discrete T_2^* might be also employed at each voxel. This will have a huge computation burden as approximately 250-500 labels should be built at each voxel. Consequently, the processing time will significantly increase.

ii. In the previous chapter the imposed smoothness was controlled by two factors: the smoothness-constraint parameter and the MDL-parameter (label cost). In certain cases, manual tuning of both parameters were required, which makes it less applicable in clinical practice.

iii. The evaluation of the convex relaxation approach was done against the well-known region-growing IDEAL-based technique [2]. Further comparisons against different techniques in the literature are required to assess the performance of the proposed smoothness constraint.

المنارة للاستشارات
www.manaraa.com

3.2 Introduction

Among various methods, Dixon-based, or chemical-shift based, techniques [3] have become the most commonly used for quantitative fat measurement due to their ability to generate a fat-only image with positive contrast. This approach relies upon the chemical-shift induced frequency difference between fat and water (~3.5 ppm). Basically, a multi-point Dixon method requires multiple acquisitions at different echo-times (TEs), followed by a post-processing step to reconstruct fat and water components. However, this reconstruction process can be severely hindered by the inhomogeneities in the main magnetic field (B0) that can cause ambiguity in the identification of water and fat signal components. Therefore, mapping such inhomogeneities – so called field mapping - is necessary for a correct water/fat separation. An incorrect estimation of field map values will propagate to the reconstructed fat and water images, causing what is commonly referred to as water/fat swaps, where the main signal in a water-dominant voxel is identified as fat, and vice-versa.

Several Dixon based techniques have been proposed in the literature to resolve the field inhomogeneity confounding water/fat separation [2, 4-17]; however, an algorithm that can guarantee an accurate separation without noticeable swaps has yet to be demonstrated. One common technique is the IDEAL (Iterative Decomposition of water and fat with Echo Asymmetry and Least-squares estimation) method [12] which has demonstrated successful separation in liver applications [18]. IDEAL [12, 13] employs an iterative process to simultaneously estimate the field map, fat and water components. However, the original IDEAL implementation [12, 13] uses a local optimization method that heavily depends on the initialization process, and hence, convergence to the global optimum is not guaranteed. Moreover, it is a voxel-independent optimization, i.e. it does not enforce any global smoothness prior to the estimated field map.

A region-growing method has been proposed by Yu et al. [2] to address the limitations of IDEAL. They performed zero-initialized IDEAL processing on a low-

المنارة للاستشارات
www.manaraa.com

resolution version of the image, and used the output as an initial guess for a specific region in the high-resolution (original) image. After performing IDEAL, the field map values of this region were then linearly extrapolated in a square-spiral trajectory, to be used as an initial guess for the local neighboring pixels. Although this method implicitly imposes a spatial smoothness on the field map via the extrapolation process, it does not account for the abrupt changes in magnetic field that might exist at tissue/air interfaces, which might cause water/fat swaps.

The VARPRO formulation [7] has been used to resolve the ambiguity of field map estimation and was addressed using the iterated conditional modes (ICM) algorithm [7], which is based on the use of Markov Random Fields, and the well-known graph-cut algorithm [8]. This approach imposes a smoothness constraint by considering the differences between a field map value at certain pixel and the neighboring values. While this explicit spatial smoothness is used to avoid incorrect estimation, over-smoothing of the field map may occur, particularly where rapid variations of B0 exist. To avoid over-smoothness, Lu and Lu [11] introduced the JIGSAW algorithm, in which a new consistency measure between adjacent field map values replaced the conventional spatial smoothness constraint. However, the algorithm was only introduced for a single peak fat spectrum, and the T2* decay, which is necessary for accurate quantification of fat fraction [19], was not considered. Another recent technique is the Fat Likelihood Analysis for Multiecho Signals (FLAME) [17], which identifies water- and fat-dominant pixels by exploiting the fitting residuals of two different signal models as complementary information, in addition to field map smoothness, to achieve the separation.

We have previously proposed a modified version of the IDEAL method capable of resolving abrupt B0 transitions without over-smoothing the resultant field map [14, 15]; it outperforms the widely-used region-growing-based IDEAL. This method 'labels' the field of view into regions of coarse estimates of frequency offsets before applying the IDEAL reconstruction. In the current work, the labeling approach is extended to include the T2* effect in the reconstruction process, showing that

المنارة للاستشارات
www.manaraa.com

inclusion of T2* in the labeling stage significantly improves the robustness of water/fat separation. Moreover, an adaptive spatial filtering stage is added as a pre-processing step to increase the efficiency of the approach by generating an approximate estimate of the vulnerable locations that might result in water/fat swaps. Finally, comparisons with recently proposed techniques, namely the graph-cut [8] and the FLAME [17] methods, are provided. The approach was tested on liver and cardiac images of healthy volunteers, abdominal datasets of NAFLD patients with iron-overload where T2* maps are required for diagnosis, as well as cases from the ISMRM 2012 challenge on water-fat separation.

3.3 Theory

The proposed method consists of two stages, the first of which produces an approximate estimate of the field map in which each voxel is assigned a frequency offset near its optimal global minimum. In other words, a coarse discretization of the whole range of the field map (bounds described next section) is used to assign each region in the image domain to certain frequency offset. The objective of this stage is to enforce the estimation process towards the global minimum. The output is employed as an initial estimate of the field map in the gradient-descent-based IDEAL processing of the second stage where the final field map (in a higher frequency resolution) is obtained. Therefore, the role of the first stage is to resolve the ambiguity of the estimation by the convex-relaxation approach, while the second step converges to the exact value of the frequency offset. This approach is capable of detecting the regions of abrupt changes of frequency offset via a unique smoothness constraint imposed in the labeling stage [14, 15]. The process of dividing the image domain into regions is termed “labeling”. In this work, the Potts labeling model [20] is used through its convex-relaxed formulation [20, 21]. In particular, the approach essentially relies on a continuous max-flow algorithm to solve the labeling model prior to the IDEAL processing and is therefore named Max-IDEAL.

المنارة للاستشارات
www.manaraa.com

In addition to the well-known non-convex property of this problem [6-8, 10, 13], the required degree of smoothness is another challenge that accompanies the estimation process. Although the variations of magnetic field are assumed to be smooth, enforcing a strong spatial smoothness can produce erroneous estimation if the algorithms employed do not account for the sudden B0 variations that are induced at air/tissue interfaces as well as for the high rates of change of inhomogeneities that might exist throughout the field of view. Additionally, an accurate signal modeling is required for a correct estimation. In other words, as the cost function is derived from the signal equation, considering the multi-peak fat spectrum and the T2* decay in the signal model is necessary to reduce the ambiguity in distinguishing the correct field map from the aliased solution (i.e. the solution that causes a "water/fat swap") [17, 19]. It was previously shown that T2*-IDEAL stage provides more accurate fat fraction maps [1, 18, 19]. However, as will be shown in this work, it is also necessary to incorporate the effect of T2* decay in the labeling stage.

In the following sections, the cost function to be minimized is derived from the signal equation, and then the adaptive spatial filter and the multi-labeling model are described.

3.3.1 Signal Equation

Let $S(.)$ denote the signal acquired from a voxel v, containing a mixture of water and fat, such that:

$$S_v(t_n) = \left(\rho_{W,v} + \rho_{F,v} \cdot \sum_{m=1}^{M} \alpha_m . e^{i2\pi\, \delta_m\, t_n}\right) . e^{i2\pi\, \varphi_v\, t_n}\, e^{-R_{2v}^{*}\, t_n}\,, \tag{3.1}$$

where t_n (s) denotes the echo-time (TE) $(n = 1, \dots, N)$ of the acquired signal; $\rho_{W,v}$ and $\rho_{F,v}$ are the water and fat components at voxel v, respectively; M is the number of fat peaks in the fat spectrum; δ_m (Hz), is the frequency of the m-th peak with its

المنارة للاستشارات
www.manaraa.com

corresponding amplitude α_m , such that $\sum_{m=1}^{M} \alpha_m = 1$; φ_v (Hz) is the local frequency offset at voxel v (i.e. the *field map*), $R_{2_v}^*$ (s^{-1}) models the T_2^* (s) decay at voxel v, such that $R_2^* = \frac{1}{T_2^*}$. A pre-calibrated fat spectrum model is employed [19], where M=6, δ_m= [485.41, 434.32, 332.12, 247.82, 49.82, -76.64] Hz at 3.0 Tesla, with corresponding amplitudes, α_m=[0.0870, 0.6930, 0.1280, 0.0040, 0.0390, 0.0480]. Having four or more echo-times (TE) acquired, Equation 3.1 can be reformulated as follows [1, 13]:

$$\mathrm{S}_v(t_n) = \Psi_v(\varphi, R_2^*, t_n) \,.\, \mathrm{A}(t_n) \,.\, \mathrm{P}_v \;, \tag{3.2}$$

where

$$\Psi_v(\varphi, R_2^*, t_n) = \begin{bmatrix} e^{i\,(2\pi\,\varphi_v + iR_{2_v}^*)t_1} & 0 & 0 \\ 0 & \ddots & 0 \\ 0 & 0 & e^{i\,(2\pi\,\varphi_v + iR_{2_v}^*)t_N} \end{bmatrix},$$

$$\mathrm{A} = \begin{bmatrix} 1 & \sum_{m=1}^{M} \alpha_m . e^{i2\pi\,\delta_m\,t_1} \\ \vdots & \vdots \\ 1 & \sum_{m=1}^{M} \alpha_m . e^{i2\pi\,\delta_m\,t_N} \end{bmatrix}$$

$\mathrm{S}_v(t) = [S_v(t_1), \dots\, S_v(t_n)]^T$, $\mathrm{P}_v = [\rho_{W,v},\ \rho_{F,v}]^T$. To estimate the required water and fat components $(\rho_{W,v},\ \rho_{F,v})$, the frequency offset φ_v should be demodulated first. Hence, dropping the known echo-time(t_n), a non-linear weighted least-squares cost function can be derived from (Equation 3.2) as follows:

$$\Gamma_v(\varphi, R_2^*) := \left\| \mathrm{A} \,.\, \widehat{\mathrm{P}_v} - \widehat{\Psi}_v^{\,-1}(\varphi\,, R_2^*) \,.\, \mathrm{S}_v \right\|_2$$

المنارة للاستشارات
www.manaraa.com

$$\Gamma_v(\varphi, R_2^*) := \left\| (\mathrm{AA}^\dagger - I).\widehat{\Psi}_v{}^{-1}(\varphi\,, R_2^*).\mathrm{S}_v \right\|_2 \,, \tag{3.3}$$

where $\widehat{\mathrm{P}_v}$ and $\widehat{\Psi}_v(\varphi\,, R_2^*)$ are the estimated values of P_v and $\Psi_v(\varphi, R_2^*)$ respectively, I is the identity matrix, and † denotes the pseudo-inverse, $s.t.$ $\mathrm{A}^\dagger = [\mathrm{A}^T\mathrm{A}]^{-1}\mathrm{A}^T$.

Two main problems are encountered when minimizing $\Gamma_v(\varphi, R_2^*)$: first, the non-convex property of the function shows multiple local minima – Figure 3.1 (a, b). Second, $\Gamma_v(\varphi, R_2^*)$ does not impose *a priori* smoothness on the estimated field map, as it is a voxel-by-voxel based strategy.

It is important to note that to maximize the signal-to-noise performance, the images are acquired at equally-spaced echo-time shifts (i.e. $\mathrm{TE_n} - \mathrm{TE_{n-1}} = \Delta\mathrm{TE}$) [12]. In this case, $\Gamma_v(\varphi)$ is periodic with a period of $1/\Delta\mathrm{TE}$, allowing us to determine the lower and upper bounds of the search space, which are set to $[\pm 1/(2\Delta\mathrm{TE})]$, necessary for the max-flow model employed in the first stage.

The required smoothness level depends on the severity of B0 inhomogeneity, which varies between different anatomies as well as with different acquisition parameters [12, 22] (e.g. first TE, echo-spacing). In Soliman *et al.* [15], water/fat swaps were avoided primarily via adjusting two parameters: a label-cost prior and the smoothness parameter of the labeling model. To reduce the effort of case-by-case adjustment in the current work, the label-cost prior is replaced instead by performing two major modifications to the signal residuals $\Gamma_v(\varphi)$: 1. incorporating $\mathrm{T_2}^*$ effect in the labeling stage; 2. introducing an adaptive spatial filter (ASF) as a pre-processing step before the labeling stage.

المنارة للاستشارات
www.manaraa.com

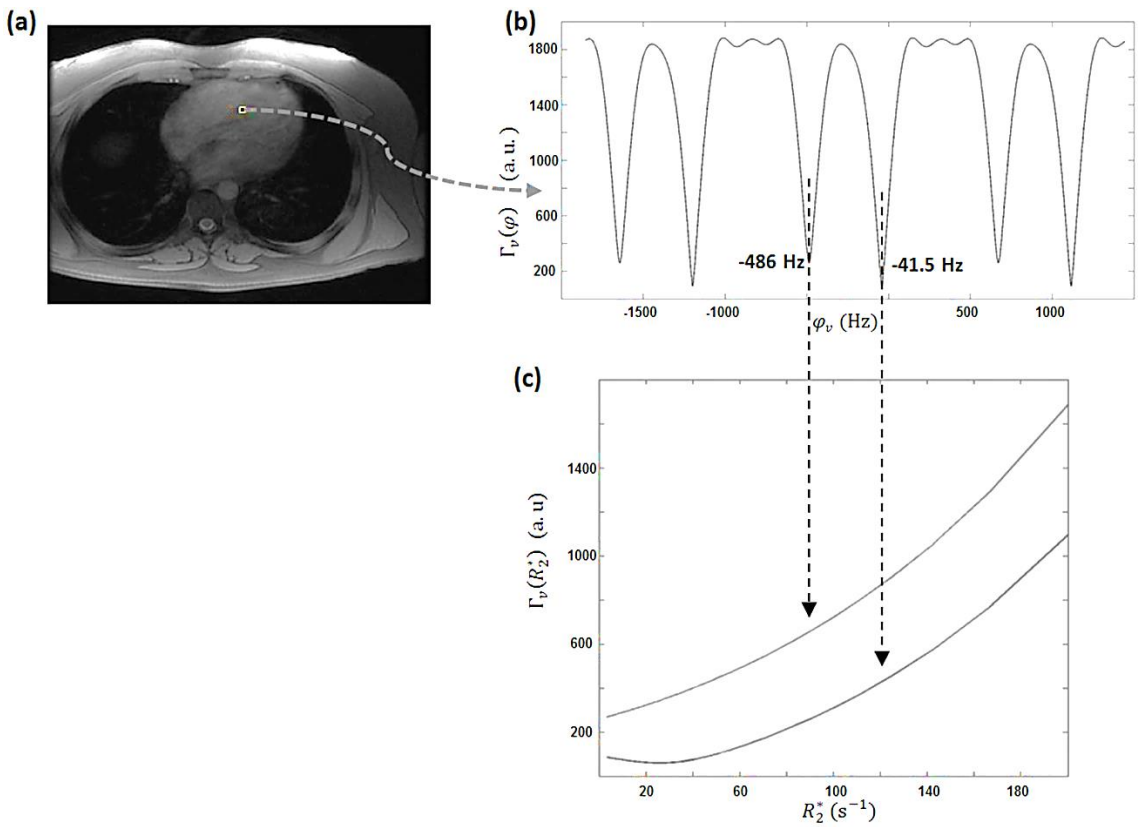

Figure 3.1: (a) A point is selected on a 2D axial cardiac image.
(b) Neglecting the effect of T_2^* decay (i.e. $R_2^* = 0$), the variation of the signal residuals $\Gamma_v(\varphi)$. (c) By assigning φ_v to its optimal value (-41.5 Hz) and the aliased value (-486 Hz), the variation of $\Gamma_v(R_2^*)$ is drawn with different R_2^* values.

المنارة للاستشارات
www.manaraa.com

3.3.2 Inclusion of T_2^* effect

The residual function $\Gamma_v(\varphi, R_2^*)$ varies in a 2D space over the field map, φ and R_2^* respectively. Unlike the field map, the variation of the signal residuals (Equation 3.3) with T_2^* decay is less complicated. In order to minimize $\Gamma_v(\varphi, R_2^*)$ for the optimal field map, a dimensionality reduction is necessary. Previously, "joint" [6, 8] and "decoupled" [6] approaches were used to include the T_2^* effect. In the "joint" estimation, for certain frequency offset φ_i, the residual function is redefined with respect to R_2^*, $s.t. \overline{\Gamma_v}(\varphi_i) = \min \Gamma_v(\varphi_i, R_2^*)$; whereas in the "decoupled" estimation, $R_2^*$is first neglected $s.t. \overline{\Gamma_v}(\varphi_i) = \Gamma_v(\varphi_i, R_2^* = 0)$, then subsequently estimated in a second step. In this work, a different approach is used to address the T_2^* effect. In Figure 3.1 (c), we observed that, for certain frequency offset φ_i , the change of the residual function, $\Gamma_v(\varphi_i, R_2^*)$ over a discrete R_2^* range is a simple convex function, which usually has lower residuals from the correct minimum, $\varphi_{correct}$, than those obtained from the aliased solution, $\varphi_{aliased}$. Therefore, by summing the residuals over the discrete set of R_2^* values, a variant of the residual function is defined as follows:

$$\overline{\Gamma_v}(\varphi_i) = \sum_{k=1}^{K} \Gamma_v\left(\varphi_i, R_{2_k}^*\right), \tag{3.4}$$

where K is the number of discrete R_2^* set. Consequently, $\overline{\Gamma_v}(\varphi)$ becomes a more accurate representation of the cost of assigning frequency φ at voxel v. We found that this "inclusive" approach is more amenable to the incorporation of T_2^* decay effects in the labeling process, which is essential in some cases, as will be shown in the discussion section.

المنارة للاستشارات
www.manaraa.com

3.3.3 Adaptive Spatial filtering (ASF)

This filter produces an approximate estimate of the locations where water/fat swaps may occur, and the corresponding cost of these locations is consequently increased. The rationale beyond modifying the cost arises from the fact that, for a uniform echo-spacing acquisition, $\overline{\Gamma_v}(\varphi)$ exhibits at least two minima [5, 10, 14] for the correct and aliased solutions respectively – Figure 3.1 (b). Hence, by increasing the cost of the vulnerable locations, $\overline{\Gamma_v}(\varphi)$ is weighted towards the correct frequency offset at voxel v. The ASF is performed as follows:

Assuming η_v is a straightforward minimization of $\overline{\Gamma_v}(\varphi)$ at voxel v, $s.t.$

$$\eta_v = \underset{\{\varphi_i\}_{i=1}^{L}}{\operatorname{argmin}} \overline{\Gamma_v}(\varphi_i) \tag{3.5}$$

where L is a discrete set of frequency offsets. As noted by Lu *et al.* [10], the global minimum of the signal residuals at certain location v might not represent the correct frequency offset. Hence η is expected to show clear fat/water swaps, as demonstrated by Figure 3.2 (a). For a pixel with coordinates (m, n), we define $\eta_x^i(m,n)$, as a backward finite difference of η in the x-direction, $s.t.$ $\eta_x^i(m,n) = \eta(m,n) - \eta(m-i,n)$; $i = 1 \dots c_1$; and $\eta_y^j(m,n)$ as a backward finite difference of η in the y-direction, $s.t.$ $\eta_y^j(m,n) = \eta(m,n) - \eta(m,n-j)$; $j = 1 \dots c_2$; where c_1 and c_2 are two positive constants determining the range of finite differences at each direction respectively. Hence, we define $F^{(k)}(m,n)$ as the filter output at iteration k, $s.t.$

$$F^{(k)}(m,n) = \sum_{i=1}^{c_1} \eta_x^i(m,n) + \sum_{j=1}^{c_2} \eta_y^j(m,n) \tag{3.6}$$

المنارة للاستشارات
www.manaraa.com

The output of $F^{(1)}$ is shown in Figure 3.2 (b), where the vulnerable locations of water/fat swaps can easily be identified and separated via simple thresholding - Figure 3.2 (c). Dropping the pixel coordinates (m, n) for simplicity, the corresponding cost at voxel v is therefore modified as follows:

$$\overline{\Gamma_v^{(k)}}(\varphi_i, i = 1, \dots, L \mid \varphi_i = \eta_v) = \begin{cases} \overline{\Gamma_v^{(k-1)}}(\varphi_i) + c_3 & F^{(k)} > c_4 \\ \overline{\Gamma_v^{(k-1)}}(\varphi_i) & otherwise \end{cases} \tag{3.7}$$

where c_3 and c_4 are constants representing the added cost and the filter threshold, respectively. At the end of each iteration, η is updated, $s.t.\ \eta^{(k+1)} = \text{argmin}_{\{\varphi_i\}_{i=1}^{L}} \overline{\Gamma^{(k)}}(\varphi_i)$. Figure 3.2 illustrates the role of the filter, showing η before (Figure 3.2 (a)) and after (Figure 3.2 (d)) the ASF processing. The resultant data cost, $\bar{\Gamma}(\varphi)$, obtained from ASF is then employed in the labeling stage (Equation 3.8), described next.

المنارة للاستشارات
www.manaraa.com

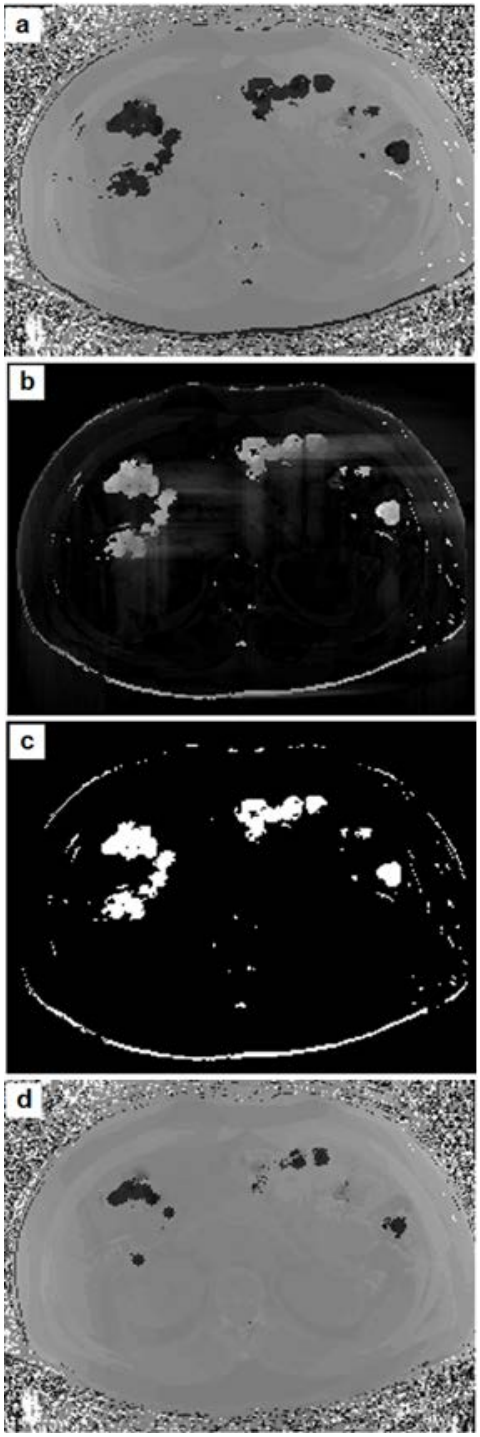

Figure 3.2: (a) Field map, η, obtained from Eq.5 before applying the adaptive spatial filter (ASF); (b) the output of ASF after the first iteration, $F^{(1)}$, from Eq.6; (c) A thresholded version of (b), producing a binary mask for the vulnerable locations of water/fat swaps; (d) the final output of the ASF, showing less water/fat swaps than (a).

المنارة للاستشارات
www.manaraa.com

3.3.4 The Potts Labeling Model

Recalling from Chapter 2, the Potts labeling model minimizes the total perimeter of all single-label regions, and results in a partition of the continuous domain Ω into L disjoint subdomains $\{\Omega_i\}_{i=1}^{L}$, as follows:

$$\min_{\{\Omega_i\}_{i=1}^{L}} \sum_{i=1}^{L} \int_{\Omega_i} \Gamma(\varphi_i, x)\, dx \; + \lambda \sum_{i=1}^{L} |\partial\Omega_i| \tag{3.8}$$

$$s.t. \bigcup_{i=1}^{L} \Omega_i = \Omega, \;\; \text{and} \;\; \Omega_k \bigcap \Omega_m = \emptyset, \qquad \forall k \neq m$$

where the set of labels φ_i, $i = 1, \dots, L$, corresponds to a set of equally-spaced frequency offsets, i.e. it is a rough discretization of the field map range. $\Gamma(\varphi_i, x)$ is the cost of assigning label φ_i to location x, as defined in Equations 3.3, 3.4 and 3.7. Each subdomain Ω_i, $i = 1, \dots, L$, is labeled with a certain frequency offset φ_i, $i = 1, \dots, L$, where $|\partial\Omega_i|$ measures the perimeter of each subdomain Ω_i, $i = 1, \dots, L$, and λ is a regularization parameter that controls the weight of the total perimeter of the disjoint regions. It is important to note that the required smoothness of the field map is imposed here by the minimization of the total perimeter of the labeled regions included in the Potts model. This regularization term replaces the conventional local spatial smoothness constraint that was previously used in the literature [6-8]. The proposed smoothness constraint is capable of handling field inhomogeneities with high rates of change, as shown later.

The multi-label Potts model in Equation 3.8 can be approximated as a convex optimization problem, leading to a convex-relaxed Potts model that can be addressed using a flow-maximization approach, as proposed by Yuan *et al.* [20]. The continuous max-flow approach [20, 21] is equivalent to the minimal cut solution over the continuous image domain [21]. By mapping the labeling model to a continuous network flow problem as described in [20], $\Gamma(\varphi_i, x)$ is set as the upper bound of the sink flow, ρ_i, where $\rho_i(x)$ is the flow streaming from each labeled

المنارة للاستشارات
www.manaraa.com

copy, Ω_i, to a sink t, at each $x \epsilon \Omega$. For more details, please refer to Yuan *et al.* [15, 20]. It is important to note that in the convex flow configuration, the regularization term, $\lambda \sum_{i=1}^{L} |\partial \Omega_i|$ in Equation 3.8 is mapped to the spatial flow of the network, for which the capacity of the flow controls the smoothness level of the total perimeter of the labeled regions. In other words, by employing the continuous max-flow approach, the capacity of the spatial flow becomes the tunable parameter that controls the degree of smoothness of the total perimeter in the labeling stage, $s.t.\ |q_i\ (x)| \leq \beta$. Here, $q_i(x), i = 1, \ldots L$ is the spatial flow at location x and β is its capacity, which for simplicity, is referred to as the smoothness parameter in the current context.

3.4 Methods

3.4.1 MR acquisition

This work was carried out under approval granted by the Office of Research Ethics of Western University, Canada. Cardiac and abdominal images from 5 healthy volunteers were acquired on 3T MR system (Discovery MR 750, GE Healthcare, Waukesha, WI). The data acquired consists of 32 2D cardiac images from 3 healthy volunteers at different orientations (axial; short-axis and 2, 3, and 4 chambers long axis), as well as 136 slices from 4 3D axial abdominal datasets acquired from 2 NAFLD patients and 2 healthy volunteers. All the acquisitions were obtained with 6 unipolar equally-spaced echo-times (TE). Cardiac images were acquired with a fast multi-echo GRE sequence using a cardiac 32-coil array [23]. Each cardiac slice was acquired within one ~20 s breath-hold with an interleaving acquisition [23]. Acquisition matrices of all cardiac data were 256x192, bandwidth = 651 Hz/pixel, flip angle = 8°, slice thickness = 8 mm, TR ranges between 8.31 ms and 9.74 ms, initial TE ranges between 1.82 ms and 2.38 ms with ΔTE between 0.85 ms and 0.96 ms, respectively. All abdominal data were acquired with a 3D multi-echo SPGR sequence [19] in one ~20 s breath-hold with parallel MRI acquisition. Data from 2

المنارة للاستشارات
www.manaraa.com

healthy volunteers were obtained: the first abdominal dataset consists of 8 slices of 10 mm thickness within the liver, acquired with 8-coil array at bandwidth of 1116 Hz/pixel, flip angle = 8°, TR = 7.32 ms, TE/ΔTE = 1.04/0.83 ms and acquisition matrix of 192x192. The second dataset comprised 12 slices of 5 mm thickness, acquired with 32-coil array at bandwidth of 1116 Hz/pixel, flip angle = 3°, TR = 5.8 ms, TE/ΔTE = 0.768/0.596 ms and acquisition matrix 128x128. Data from 2 NAFLD patients, covering the whole liver in 56 and 60 slices, respectively, were obtained. The 2 datasets were acquired with 8-coil array, flip angle = 5°, 5 mm slice thickness, acquisition matrix 224x128 and TR/TE/ΔTE = 7.48/1.064/0.52 ms and 7.61/1.08/0.872 ms. These data are processed as follows:

3.4.2 Pre-processing: ASF

The signal residual at each voxel is constructed as in Equations 3.3 and 3.4, and subsequently processed with the ASF as described above. The number of discrete T_2^* values is set to 3 and the values were empirically set to 10, 50 and 60 ms, as this was found to be sufficient to include the T_2^* effect without a significant increase in the computation time. T_2^* values of 50 and 60 ms were chosen as approximations to the T_2^* value of fat, while 10 ms was chosen to consider the effect of rapid T_2^* decay that might exist. The number of finite differences performed was chosen as a scale of the image dimensions, for instance, c_1 and c_2 were set to the width/5 and the height/5 of the image, respectively. For a normalized filter F, c_4 is set to 0.4 and increased by 0.2 at each iteration; and c_3 is set to 0.5.

3.4.3 STAGE I: A Continuous Max-flow Approach to Potts Model

The convex multi-labeling max-flow algorithm is capable of determining the optimal label for each voxel. As mentioned above, the labeling range is set between $[\pm 1/(2\Delta TE)]$. The range of frequency offsets is discretized into a set of equally-spaced labels, where each corresponds to certain frequency offset. The labeling process is

المنارة للاستشارات
www.manaraa.com

performed in 2D. The number of discrete labels was empirically chosen and set to 50 in all the experiments, as this was found to be sufficient to *target* a frequency offset near the global minimum, which is the goal of the first stage. The smoothness parameter β was set to a default value of 0.5. A coarse estimate of the field map is produced from this stage. It is worth noting that in some cases B0 inhomogeneities vary over more than one period throughout the field of view. This phenomenon is automatically detected before the processing. Consequently, the ASF step is automatically skipped and the smoothness parameter β is tuned down to 0.3 without user intervention. This automatic parameter tuning is necessary to avoid oversmoothing the initial field map.

3.4.4 STAGE II: T2*-IDEAL Water/fat Separation

The IDEAL iterative process has been implemented as described in Reeder *et al.* [12] and the T_2^* decay was integrated in the estimation process as proposed in Yu *et al.* [1]. The original version of IDEAL sets the initial field map estimate of the iterative process to zero in all voxels. In the proposed approach, the estimate produced by the labeling stage is used as the initial field map. The stopping criterion for the IDEAL iterative process is set to < 0.5 Hz for the field map increment over the whole image. This criterion is assumed to be sufficient for clinical applications [13]. It is worth noting that T_2^* is initialized to zero. Its effect was considered in the labeling stage to provide a more robust estimation of the field map; however, an initial T_2^* map was not carried out in the first stage.

All the reconstructions were processed on a dual core Intel-Xeon PC @ 2.4 GHz and 24 GB of RAM. The Potts labeling stage was accelerated on a graphics processing unit (GPU) NVIDIA Quadro 600 with 96 CUDA cores and 1GB of memory. Comparisons with the graph-cut were performed using the implementation provided in the Fat-Water toolbox with its default set of parameters. For the FLAME technique, the online GE reconstruction was used.

المنارة للاستشارات
www.manaraa.com

3.5 Results

The Max-IDEAL approach was tested on a total of 168 2D slices from the acquired cardiac and abdominal data mentioned above. Out of all 168 images employed in this study, adjustment of the smoothness parameter was required in 1 cardiac case and 1 abdominal case, where β was set to 1 and 0.3, respectively. Among the cardiac datasets, a single case of failure demonstrated water/fat swaps that hinder the clinical interpretation of the underlying anatomy. Water/fat separation was successfully achieved in all abdominal examples. All the datasets were processed with the T_2^* estimation integrated in the estimation process and the R_2^* map was simultaneously obtained in all cases. The average processing time for the whole approach (including T_2^* estimation) was ~14 s. Figure 3.3 shows the reconstruction of a cardiac 4-chamber view. As shown in Figure 3.3 (a), the output of the labeling stage can successfully handle the variations of B0 magnetic field by mapping each region to an approximate frequency offset. Another example of a 2-chamber cardiac slice is shown in Figure 3.4, where the fat fraction map (fat/(fat+water)) as well as the R_2^* map are shown. The abdominal data consist of 116 slices from 3D datasets of 2 NAFLD patients and 20 slices from 2 healthy volunteers. An example for a successful separation from a NAFLD patient with iron overload is shown in Figure 3.5. The reconstruction of the failure case could not be resolved with other state-of-the-art techniques, such as the graph-cut [8] and FLAME [14] methods as shown in Figure 3.6. Figure 3.7 shows a comparison between the proposed method and the labeling approach used in [15]. It is clear that using the label cost prior in [15] was not sufficient to avoid the occurrence of water/fat swaps; however, a successful reconstruction is achieved by the proposed approach.

المنارة للاستشارات
www.manaraa.com

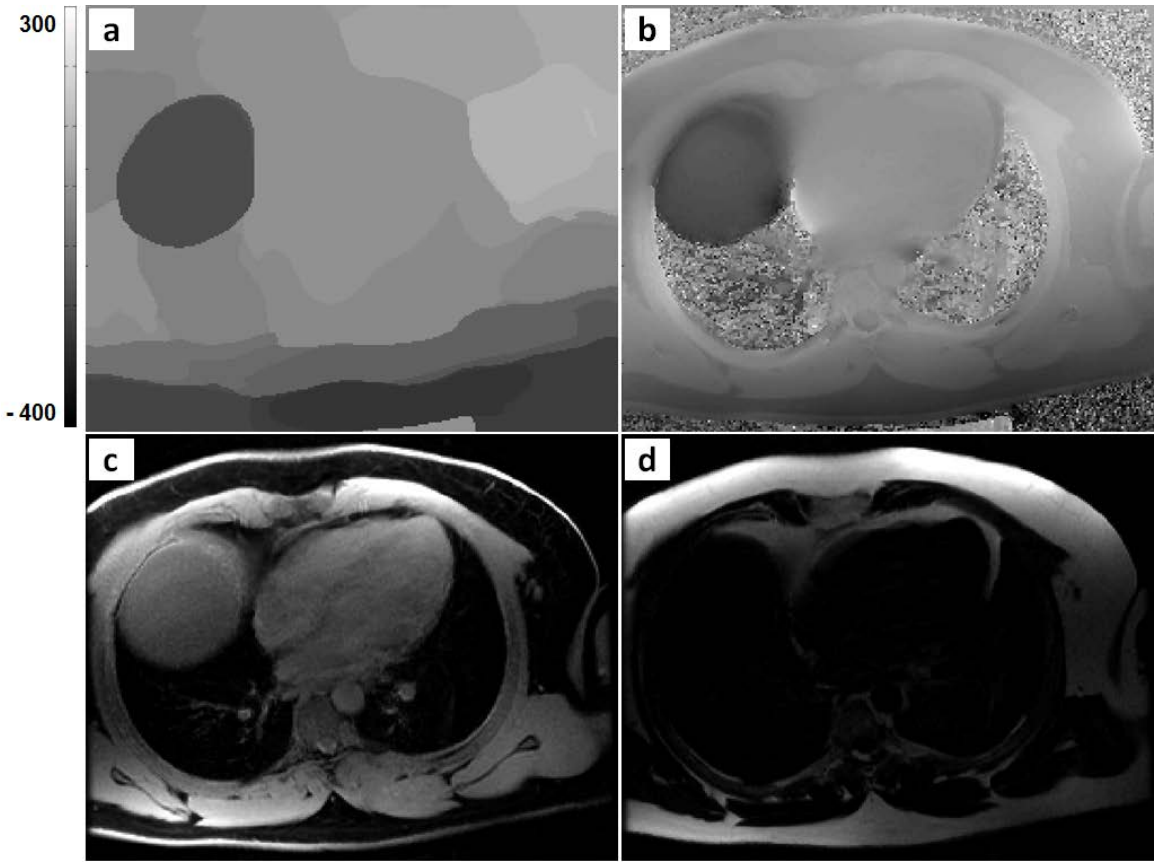

Figure 3.3: Fat water separation in a 4-chamber cardiac slice acquired from a healthy volunteer. (a) Output of the labeling stage showing a coarse estimation of the field map, (b) Final field map after the second stage, (c) Water component, (d) Fat component.

المنارة للاستشارات
www.manaraa.com

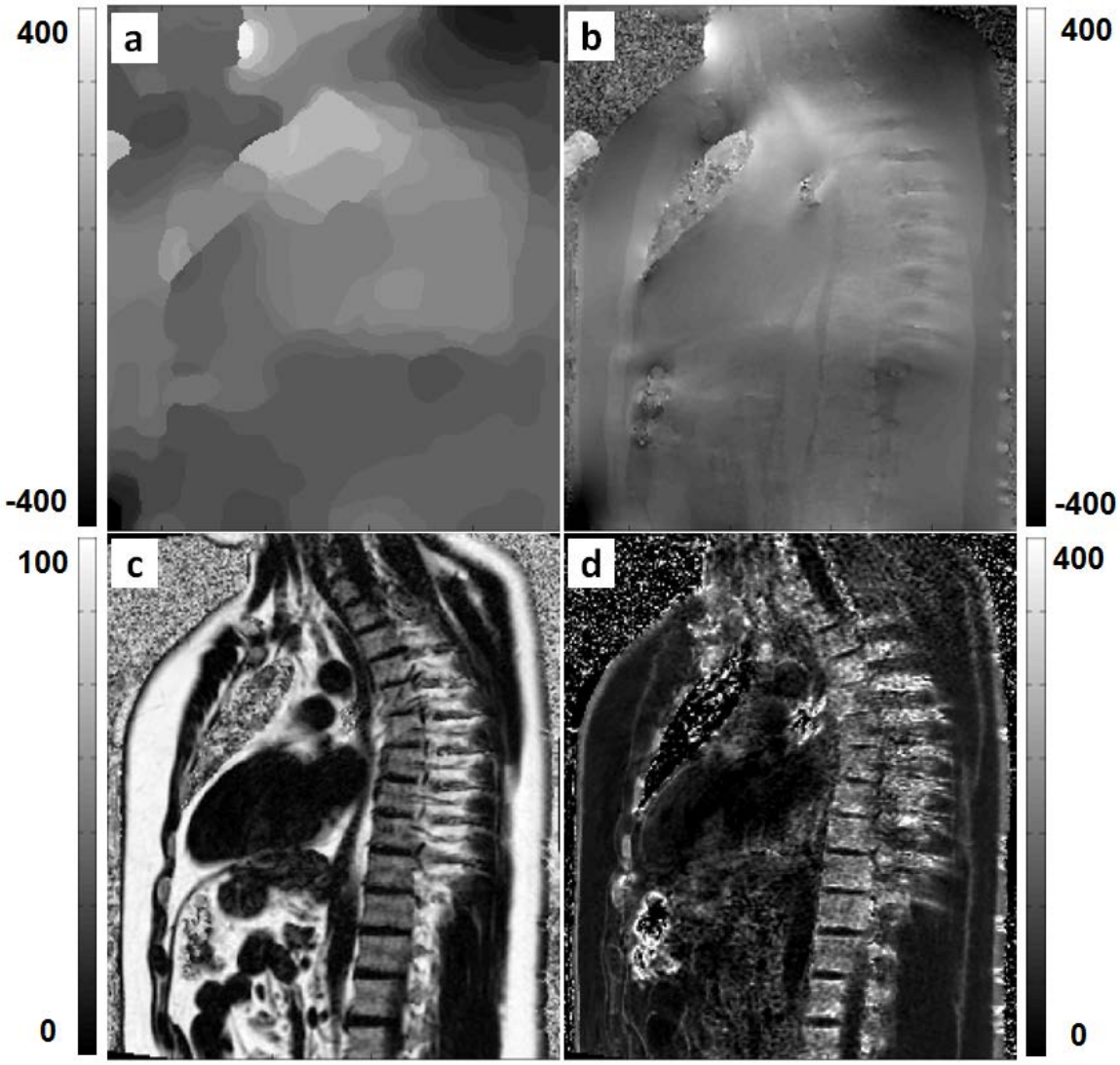

Figure 3.4: Reconstructed data from a 2-chamber cardiac. (a) The labeled field map from the first stage, (b) final field map, (c) fat fraction map and (d) R_2^* map

المنارة للاستشارات
www.manaraa.com

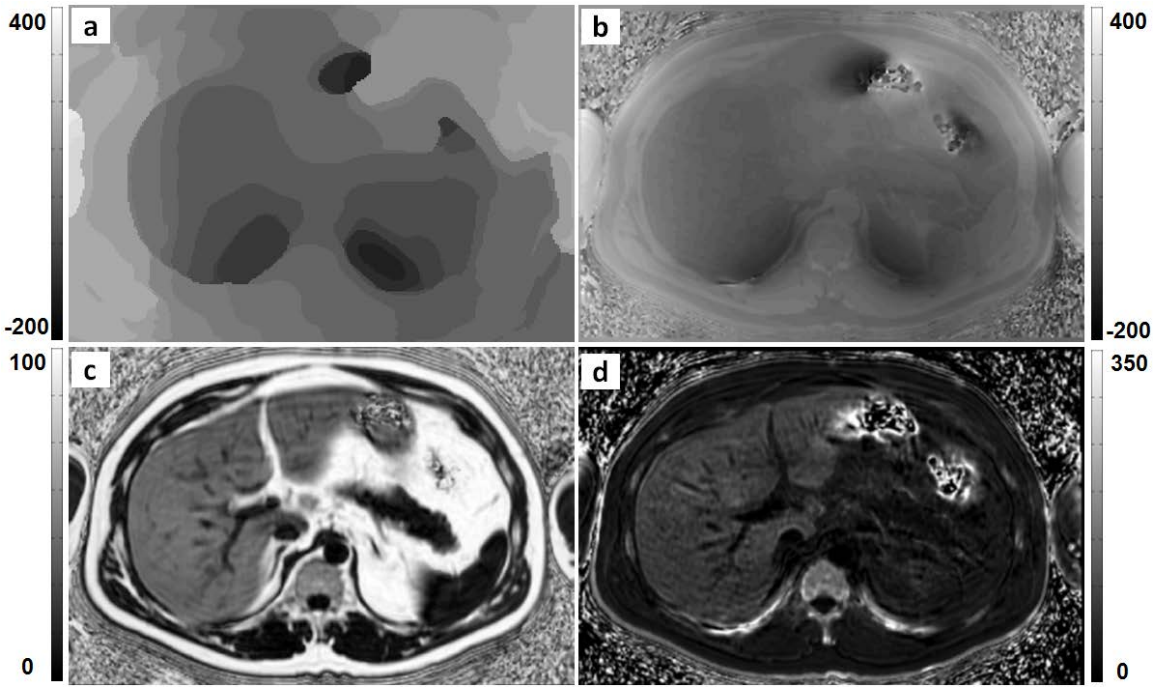

Figure 3.5: Reconstructed data from an axial abdominal slice. (a) The labeled field map from the first stage, (b) final field map, (c) fat fraction map and (d) R_2^* map

المنارة للاستشارات
www.manaraa.com

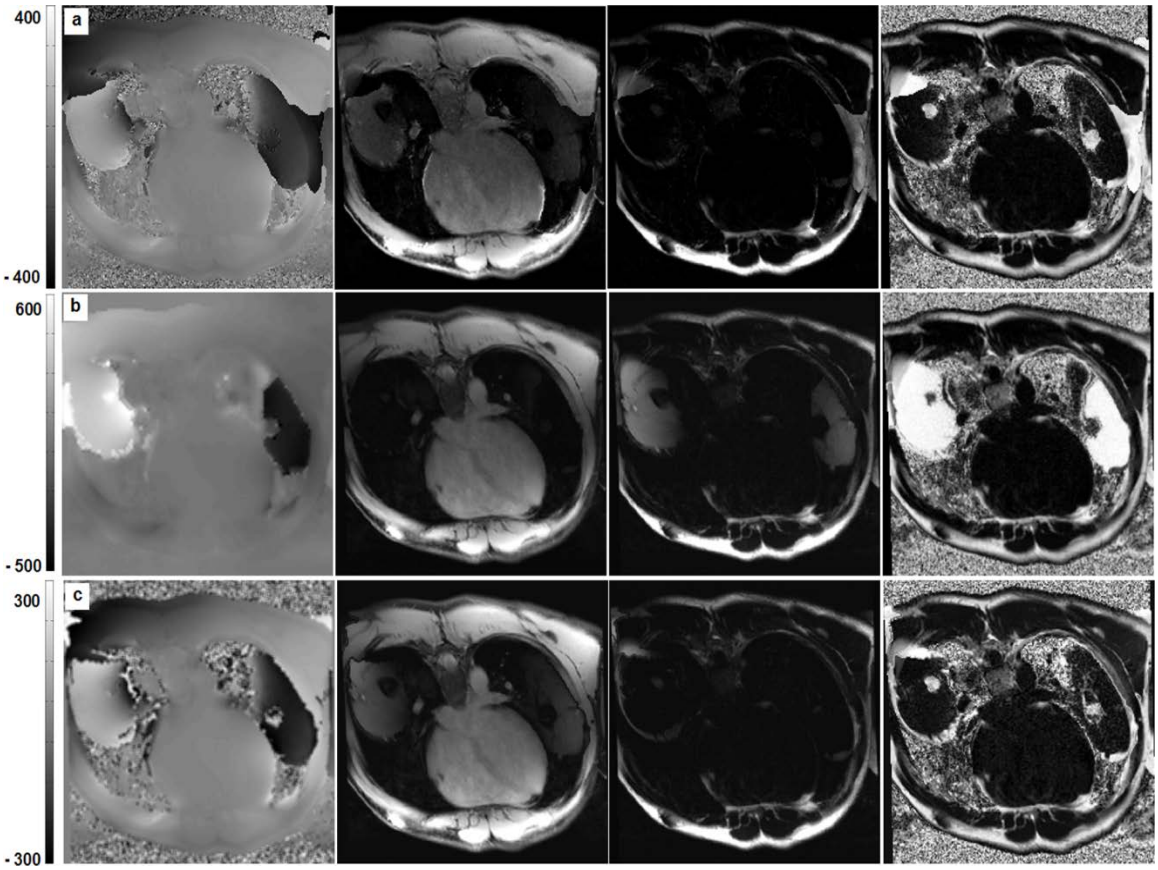

Figure 3.6: The reconstruction of the failure case using Max-IDEAL (a), the graph-cut method (b) and the FLAME technique (c). Left to right: field map, water, fat and fat fraction map.

المنارة للاستشارات
www.manaraa.com

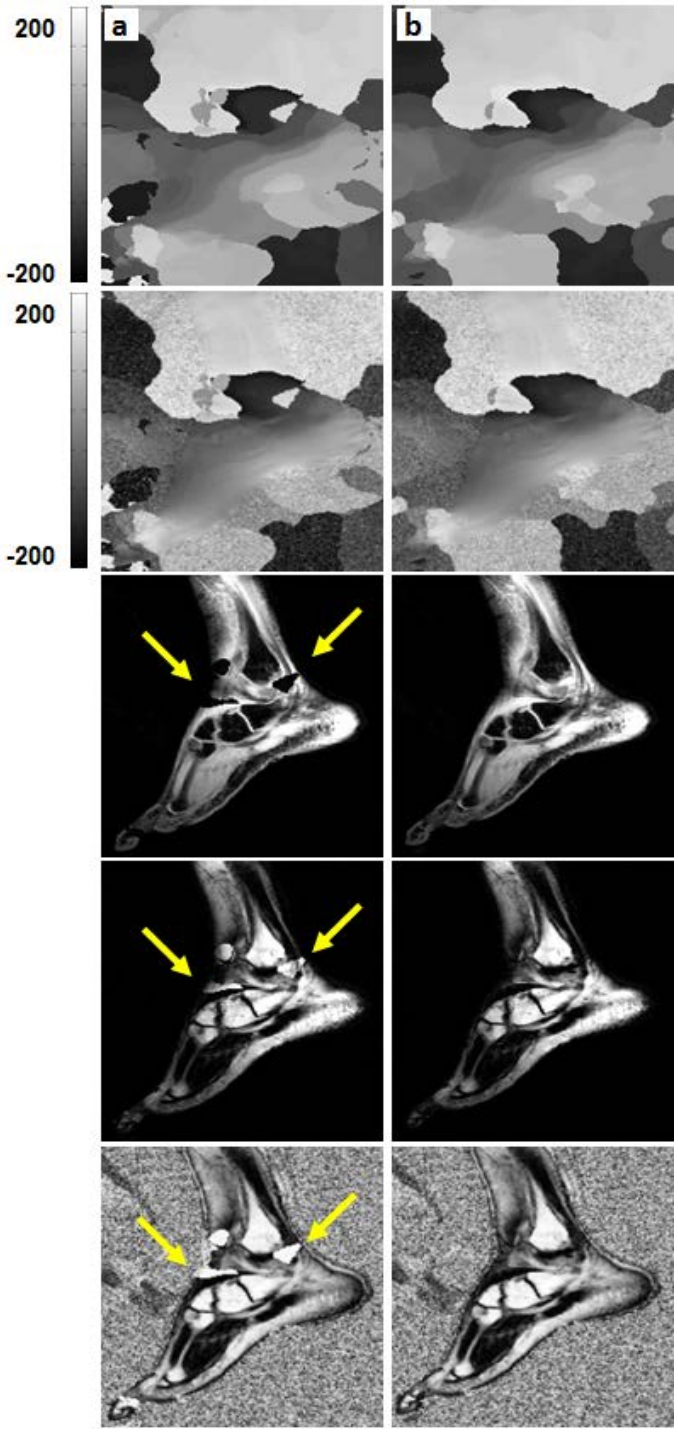

Figure 3.7: Reconstruction of a selected slice from a case provided by the ISMRM 2012 challenge with the labeling approach in [15] (a) and the proposed method (b).

المنارة للاستشارات
www.manaraa.com

In order to show the ability of Max-IDEAL to resolve the severe variations of B0 over previously proposed methods, a comparison with the graph-cut technique [8] is shown in Figure 3.8 using cases from the ISMRM 2012 challenge. The reconstructed cases show large changes in B0 magnetic field that were incorrectly estimated with the graph-cut, while they were successfully resolved with Max-IDEAL. Notice that B0 changes vary over more than one period, hence the ASF step was skipped, as mentioned earlier. Figure 3.9 shows another comparison with the water/fat reconstruction of the recent FLAME technique [14] on a short-axis cardiac slice. While the FLAME method failed to resolve rapid B0 variations, Max-IDEAL can successfully achieve the reconstruction even in the presence of significant breathing motion artifact.

المنارة للاستشارات
www.manaraa.com

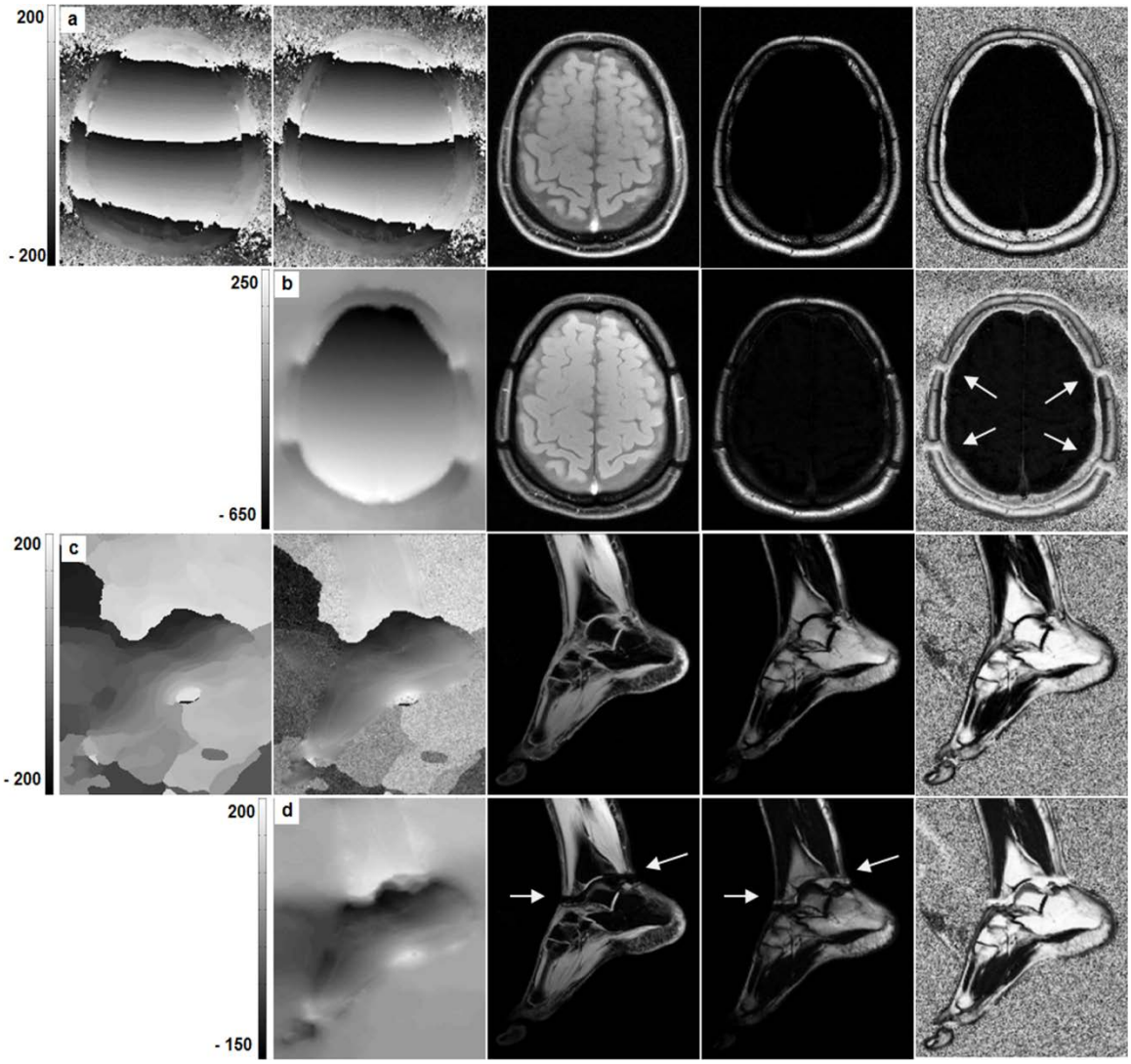

Figure 3.8: Comparisons between Max-IDEAL (a, c) and the graph-cut method (b, d) using two cases from the ISMRM 2012 challenge. The proposed approach can resolve strong B0 variations while the spatial smoothness constraint employed in graph-cut fails. Left to right: initial field map (a and c only), final field map, water, fat and fat fraction map.

المنارة للاستشارات
www.manaraa.com

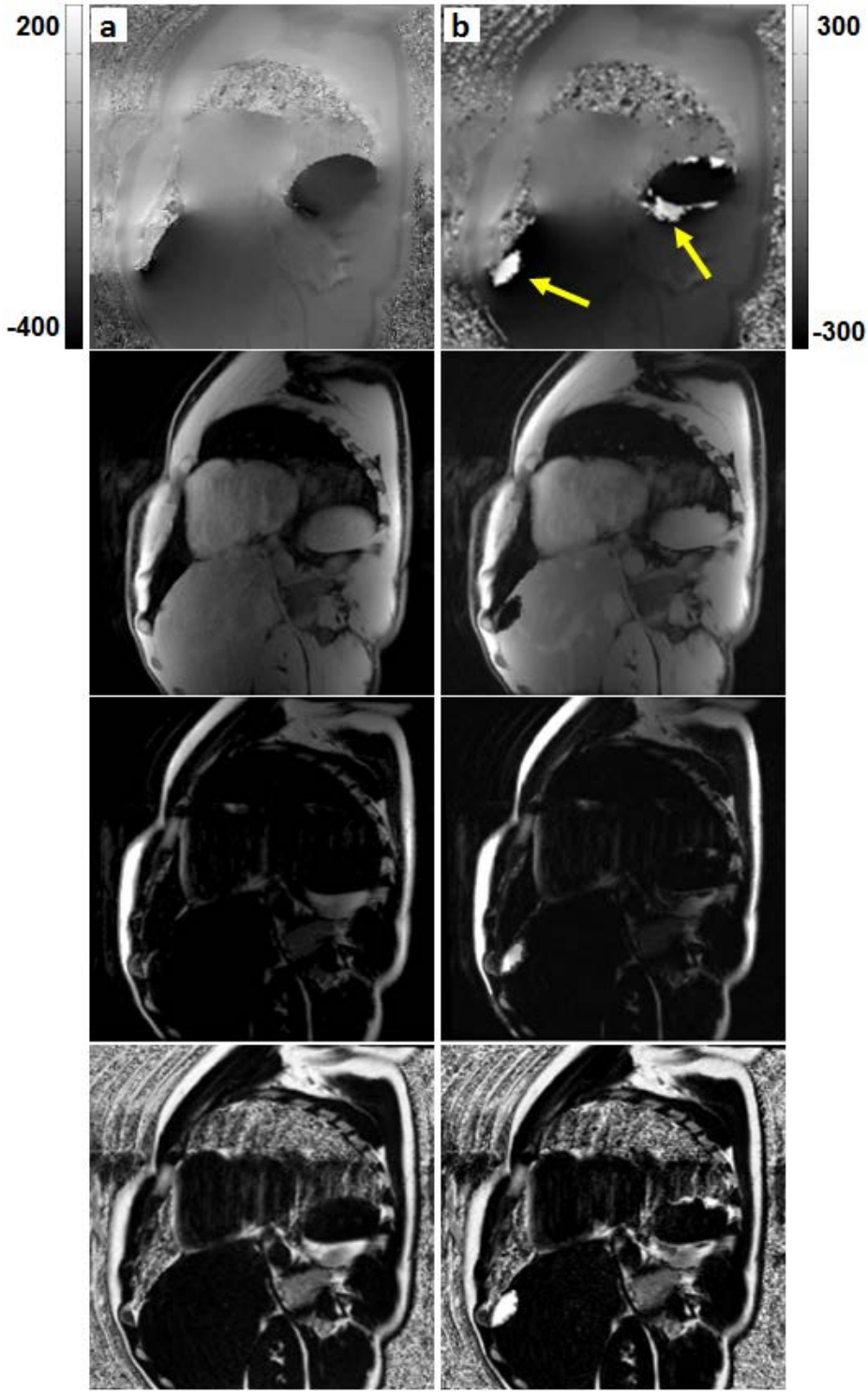

Figure 3.9: A comparison with the FLAME technique on a short-axis cardiac slice. (a) Results from Max-IDEAL; (b) results of FLAME method. Top to bottom: field map, water, fat and fat fraction map

المنارة للاستشارات
www.manaraa.com

3.6 Discussion

In this work, the problem of measuring field inhomogeneities is addressed by using a max-flow-based IDEAL approach that is capable of handling abrupt B0 variations. The Max-IDEAL method is performed in two stages, the first of which detects the correct global minimum while the second stage converges to the exact solution. In the labeling stage, the cost function is minimized over a discrete set of frequency offsets, such that the output is a coarse field map in which each region is labeled by certain offset value. A Potts labeling model was used for the labeling process, and was minimized via a continuous flow maximization approach.

A unique advantage of Max-IDEAL is that the smoothness prior is imposed in the labeling stage in a different manner than previous techniques in the literature. In previous methods, the smoothness is explicitly enforced spatially by considering the difference between the frequency offset of certain voxel and its local neighborhood [7, 8]. As an example, the quadratic function used in the graph-cut method [8] might not be capable of handling inhomogeneities with high rates of change – Figure 3.8. However, in our proposed method, the smoothness is represented by the perimeter of each labeled region, described by $|\partial\Omega_i|$ in the Potts labeling model (Equation 3.8), which enforces smoothness via minimizing the total perimeter of the labeled regions. Hence, increasing the smoothness prior in cases of severe inhomogeneity limits the occurrence of water/fat swaps without blurring or reducing the frequency resolution of the estimated field map.

The inclusion of the T_2^* effect in both stages is important. Since the ambiguity of distinguishing the correct from the aliased field map is resolved solely by the labeling stage, an accurate representation of the signal model is required in this stage. By considering T_2^* decay, the value produced from the signal residuals at each voxel (Equation 3.4) becomes a better representation of the cost of assigning the corresponding frequency offset at that voxel, which improves the robustness of the labeling stage. On the other hand, employing T_2^* in the second stage produces an accurate fat fraction as well as the R_2^* map as shown in Yu *et al.*[1, 19]. To illustrate

المنارة للاستشارات
www.manaraa.com

the importance of including T_2^* in the labeling stage, a case from the ISMRM 2012 challenge is reconstructed in Figure 3.9 with and without incorporating T_2^* in the labeling stage, while using T_2^*-IDEAL in the second stage in both reconstructions. It is clear from Figure 3.10 that the reconstruction might fail if the T_2^* effect was not considered in the labeling process.

By employing T_2^*-IDEAL, the values of R_2^* map are produced over a continuous range, in contrast to the recent graph-cut method which assigns certain value to each pixel out of a discrete set of R_2^* values [8]. Therefore, Max-IDEAL allows more efficient estimation of the R_2^* map of the underlying anatomy without a significant increase in the overall computation time.

The number of discrete values used in the labeling stage is a trade-off between the computation time of the labeling model and the accuracy of detecting the correct minimum. By using an insufficient number of discrete samples of the residuals curve (Figure 3.1 (b)), the algorithm might fail to locate the correct minimum. On the other hand, increasing the number of samples can significantly prolong the processing time. Fifty equally-spaced discrete values were therefore empirically chosen, as this was found to be sufficient to target the correct solution without a significant increase in the computation time.

المنارة للاستشارات
www.manaraa.com

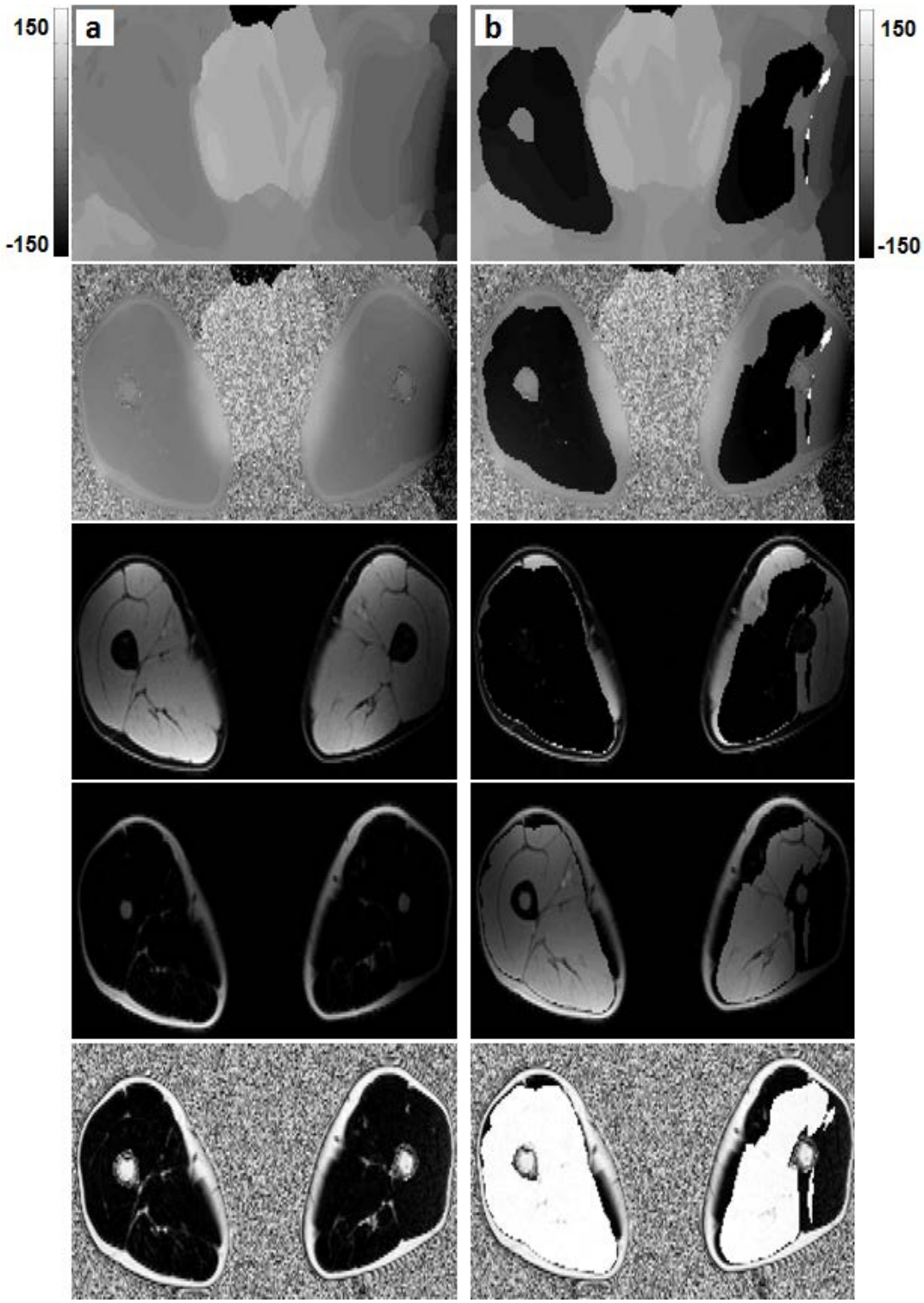

Figure 3.10: Reconstruction of a case from ISMRM 2012 challenge with (a) T_2^* applied in both stages of the approach, and (b) T_2^* incorporated only in the second stage (T_2^*-IDEAL). The reconstruction fails in case T_2^* decay is not considered in the labeling stage.

المنارة للاستشارات
www.manaraa.com

It is important to note that the cost function has a periodic form, such that a 2π phase shift does not affect the separation process – Figure 3.7 and Figure 3.8. In other words, when limiting the search space to one period centered at zero offset, a correct water/fat separation will still be obtained even if a "non-smooth" field map is produced. While the apparent smoothness of the field map is a criterion that is conventionally used to visually assess the presence of water/fat swaps, in this case the "non-smooth" appearance of field map arises from the 2π phase shift, which does not hamper the success of the reconstruction, as can be seen in the reconstructed fat and water components - Figure 3.7 and Figure 3.8.

Although the proposed approach has shown promising results in handling severe B0 inhomogeneities, Max-IDEAL has two main limitations. Firstly, an artifact might be produced in the detection of boundaries in the labeling stage. Boundaries separating two neighboring labeled regions in the output of the first stage might not represent the actual *location of the transition* of the sudden change of magnetic field, particularly when high level of smoothness is applied. Therefore, a small boundary of water/fat swap might appear in the results. An example of this artifact is shown in Figure 3.11. This phenomenon was noticed in 6 cardiac images and 18 abdominal images (total of 24 images out of 167 successfully reconstructed cases). However, the artifact was overcome in 11 cases by manually tuning the smoothness parameter β. Moreover, for the cardiac cases, it was subsequently confirmed by an expert cardiologist (J.A.W.) to not hinder the clinical evaluation of relevant cardiac structures. This artifact appears away from the region of interest (liver) in all the affected abdominal cases.

المنارة للاستشارات
www.manaraa.com

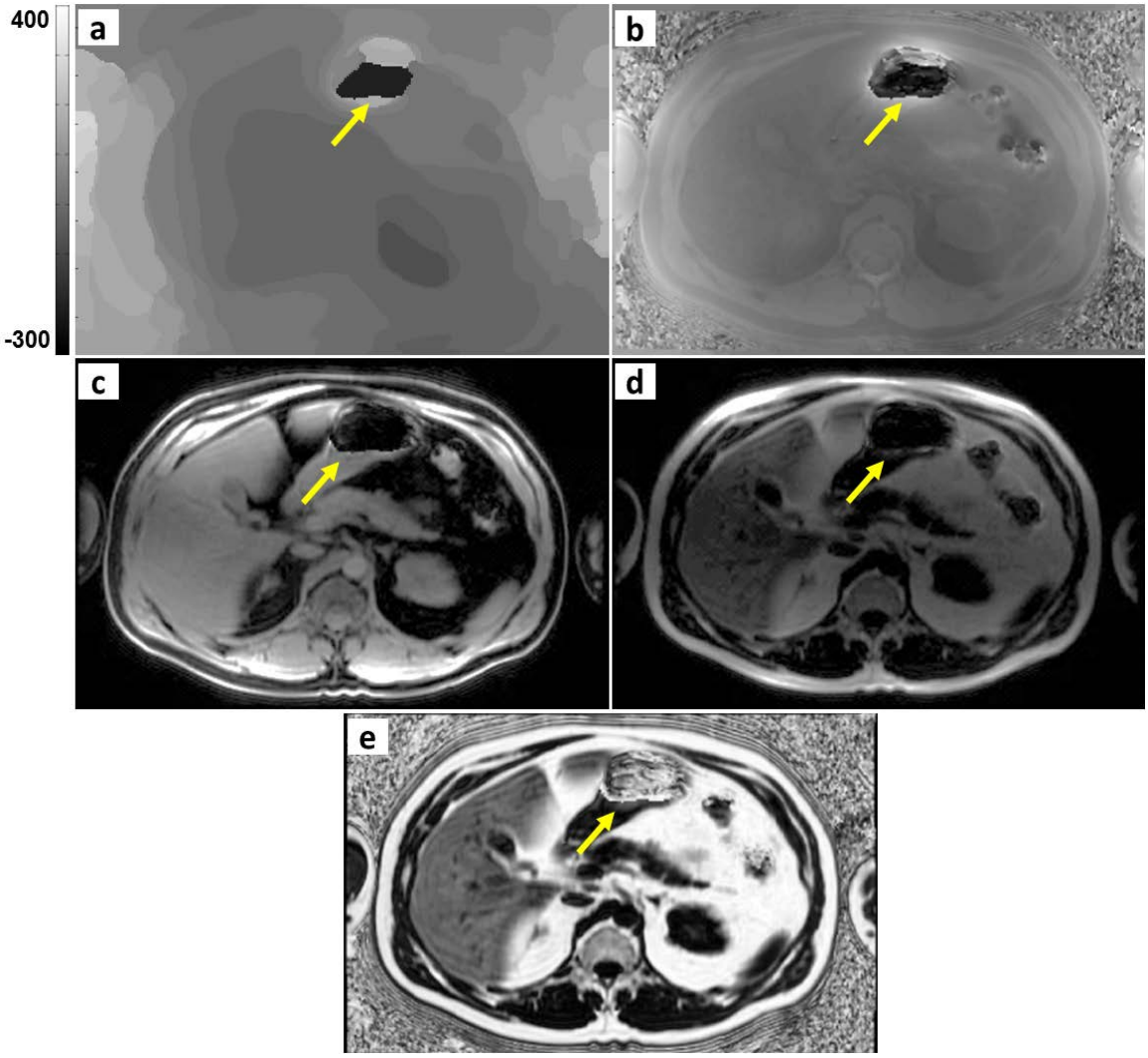

Figure 3.11: An example of the boundary artifact appearing in an axial abdominal slice. This artifact is induced around the bowels where very low signal is received.

المنارة للاستشارات
www.manaraa.com

Another limitation of Max-IDEAL is its dependence on the smoothness level enforced in the first stage. However, as shown in Figure 3.2, the ASF reduces the vulnerable regions of water/fat swaps such that a fixed (default) value for the smoothness constraint (β=0.5) becomes sufficient in most of the cases to overcome the rest of the vulnerable locations in the labeling stage. The effect of changing the smoothness level β on the reconstructed data is shown in Figure 3.11 using a case from the ISMRM 2012 challenge. As can be noticed in Figure 3.12 (a), the enforced smoothness (β=0.2) is not sufficient to avoid fat/water swaps. With higher smoothness levels, the algorithm inherently tends to use fewer labels to describe the field map [20], and hence details of the underlying inhomogeneities can be omitted, causing water/fat swaps - Figure 3.12 (d). Therefore, setting β is a trade-off between avoiding such artifact and removing water/fat swaps.

المنارة للاستشارات
www.manaraa.com

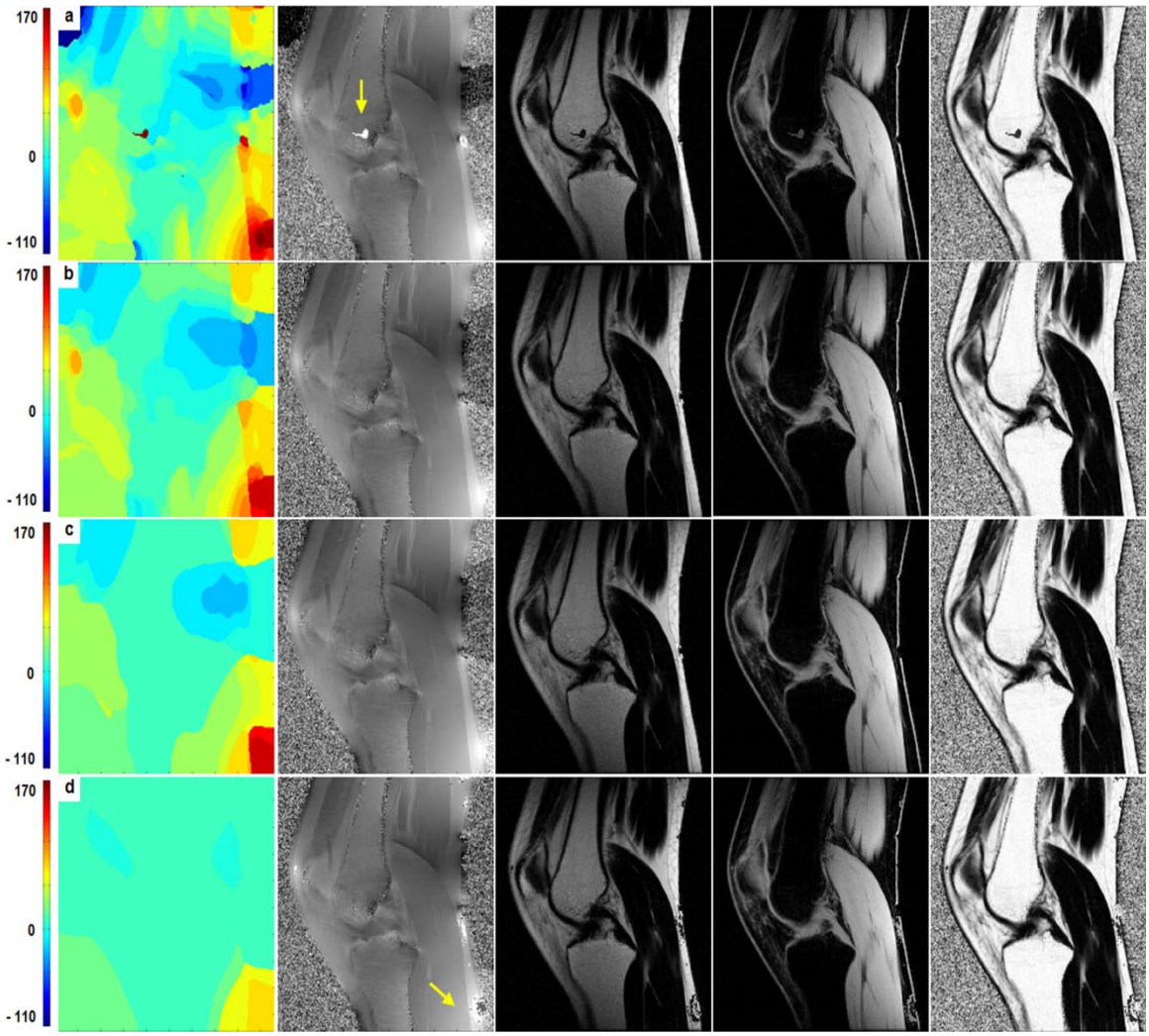

Figure 3.12: The effect of applying different smoothness levels on the reconstruction of a case from ISMRM 2012 challenge: (a) β=0.2 was insufficient to remove water/fat swaps; successful reconstruction can be achieved in (b) β = 0.5 and (c) β = 2; (d) Oversmoothed initial field map with β = 4 causes water/fat artifacts as noted by the arrow. The ASF was not applied in this reconstruction in order to solely examine the effect of the smoothness parameter.

المنارة للاستشارات
www.manaraa.com

The feasibility of 3D Max-IDEAL has been recently shown [24]. Preliminary results demonstrated successful reconstruction of abdominal datasets. Berglund *et al.*[5] have shown the feasibility of 3D whole body water/fat separation with the 3-point Dixon approach, with a qualitative assessment of the separation. We anticipate 3D Max-IDEAL to have comparable results in the pelvis, head, arms and legs, while boundary artifacts can arise in the thorax and abdomen. However, an automatic anatomy-based tuning of the smoothness level might reduce the significance of this artifact.

Although the processing time was less than 13 s for most of the cases (with a matrix size of 256x192), a more advanced GPU with higher number of CUDA cores (available up to 3072 cores) can significantly accelerate the reconstruction process. It is worth noting that applying a more advanced background removal filter than simple signal thresholding might also reduce the processing time since background pixels unnecessarily prolong the convergence rate; however, this is outside the focus of the current work.

3.7 Conclusion

In this work, we demonstrated a fast max-flow based approach for water/fat separation. The proposed method performs the IDEAL water/fat separation *guided* by a convex-relaxed labeling model that is solved via a flow maximization approach. Instead of the conventional spatial smoothness used in previous methods, Max-IDEAL relies on enforcing smooth boundaries in the labeling stage to avoid water/fat swaps. Additional robustness is gained by incorporating the T_2^* effect in both stages of the reconstruction, showing the importance of its inclusion in the labeling process. Moreover, a pre-processing filtering step was included to improve the efficiency of the reconstruction. The approach has demonstrated the ability to handle fast and severe B0 variations cases where previous spatial smoothness-based techniques can fail.

المنارة للاستشارات
www.manaraa.com

Acknowledgments

We thank Dr. Diego Hernando from the University of Wisconsin-Madison for valuable discussions. We acknowledge funding from CIHR Strategic Training Program in Vascular Research, from the NSERC Computer-Assisted Medical Intervention (CAMI) program and from the Ontario Research Fund Consortium in Interventional Cardiac Therapeutics. C.A. McKenzie holds the Canada Research Chair in Translational Magnetic Resonance Imaging at Western University. This research was undertaken, in part, thanks to funding from the Canada Research Chairs Program and GE Healthcare. We acknowledge the use of the Fat-Water Toolbox (http://www.ismrm.org/workshops/FatWater12/) for some of the experiments in this article.

المنارة للاستشارات

www.manaraa.com

References

[1] Yu, H., McKenzie, C. A., Shimakawa, A., Vu, A. T., Brau, A. C. S., Beatty, P. J., *et al.*, "Multiecho reconstruction for simultaneous water-fat decomposition and T2* estimation," *J Magn Reson Imaging,* vol. 26, pp. 1153-1161, 2007.

[2] Yu, H., Reeder, S. B., Shimakawa, A., Brittain, J. H., and Pelc, N. J., "Field map estimation with a region growing scheme for iterative 3-point water-fat decomposition," *Magn Reson Med,* vol. 54, pp. 1032-1039, 2005.

[3] Ma, J., "Dixon techniques for water and fat imaging," *J Magn Reson Imaging,* vol. 28, pp. 543-558, 2008.

[4] Berglund, J., Ahlström, H., Johansson, L., and Kullberg, J., "Two-point dixon method with flexible echo times," *Magn Reson Med,* vol. 65, pp. 994-1004, 2011.

[5] Berglund, J., Johansson, L., Ahlström, H., and Kullberg, J., "Three-point dixon method enables whole-body water and fat imaging of obese subjects," *Magn Reson Med,* vol. 63, pp. 1659-1668, 2010.

[6] Berglund, J. and Kullberg, J., "Three-dimensional water/fat separation and T2* estimation based on whole-image optimization-Application in breathhold liver imaging at 1.5 T," *Magn Reson Med,* vol. 67, pp. 1684-1693, 2012.

[7] Hernando, D., Haldar, J. P., Sutton, B. P., Ma, J., Kellman, P., and Liang, Z. P., "Joint estimation of water/fat images and field inhomogeneity map," *Magn Reson Med,* vol. 59, pp. 571-580, 2008.

[8] Hernando, D., Kellman, P., Haldar, J. P., and Liang, Z.-P., "Robust water/fat separation in the presence of large field inhomogeneities using a graph cut algorithm," *Magn Reson Med,* vol. 63, pp. 79-90, 2010.

المنارة للاستشارات
www.manaraa.com

[9] Jacob, M. and Sutton, B. P., "Algebraic decomposition of fat and water in MRI," *IEEE Trans Med Imaging,* vol. 28, pp. 173-184, 2009.

[10] Lu, W. and Hargreaves, B. A., "Multiresolution field map estimation using golden section search for water-fat separation," *Magn Reson Med,* vol. 60, pp. 236-244, 2008.

[11] Lu, W. and Lu, Y., "JIGSAW: Joint Inhomogeneity Estimation via Global Segment Assembly for Water–Fat Separation," *IEEE Trans Med Imaging,* vol. 30, pp. 1417-1426, 2011.

[12] Reeder, S. B., Pineda, A. R., Wen, Z., Shimakawa, A., Yu, H., Brittain, J. H., *et al.*, "Iterative decomposition of water and fat with echo asymmetry and least-squares estimation (IDEAL): Application with fast spin-echo imaging," *Magn Reson Med,* vol. 54, pp. 636-644, 2005.

[13] Reeder, S. B., Wen, Z., Yu, H., Pineda, A. R., Gold, G. E., Markl, M., *et al.*, "Multicoil Dixon chemical species separation with an iterative least-squares estimation method," *Magn Reson Med,* vol. 51, pp. 35-45, 2004.

[14] Soliman, A. S., Yuan, J., Vigen, K. K., White, J. A., Peters, T. M., and McKenzie, C. A., "Robust Field Map Estimation using VARPRO and Multi-labeling Continuous Max-Flow," presented at the In Proceedings of the 20th Annual Meeting of ISMRM, Melbourne, Australia 2012.

[15] Soliman, A. S., Yuan, J., White, J. A., Peters, T. M., and McKenzie, C. A., "A Convex Relaxation Approach to Fat/Water Separation with Minimum Label Description," in *Lecture Notes in Computer Science*. vol. 7511, N. Ayache, H. Delingette, P. Golland, and K. Mori, Eds., ed: Springer Berlin Heidelberg, 2012, pp. 519-526.

[16] Tsao, J. and Jiang, Y., "Hierarchical IDEAL: Fast, robust, and multiresolution separation of multiple chemical species from multiple echo times," *Magn Reson Med,* vol. 70, pp. 155-159, 2013.

المنارة للاستشارات
www.manaraa.com

[17] Yu, H., Reeder, S. B., Shimakawa, A., McKenzie, C. A., and Brittain, J. H., "Robust multipoint water-fat separation using fat likelihood analysis," *Magn Reson Med,* vol. 67, pp. 1065-1076, 2012.

[18] Hines, C. D. G., Frydrychowicz, A., Hamilton, G., Tudorascu, D. L., Vigen, K. K., Yu, H.*, et al.*, "T1 independent, T2* corrected chemical shift based fat-water separation with multi-peak fat spectral modeling is an accurate and precise measure of hepatic steatosis," *J Magn Reson Imaging,* vol. 33, pp. 873-881, 2011.

[19] Yu, H., Shimakawa, A., McKenzie, C. A., Brodsky, E., Brittain, J. H., and Reeder, S. B., "Multiecho water-fat separation and simultaneous R2* estimation with multifrequency fat spectrum modeling," *Magn Reson Med,* vol. 60, pp. 1122-1134, 2008.

[20] Yuan, J., Bae, E., Tai, X. C., and Boykov, Y., "A continuous max-flow approach to potts model," presented at the In Proceedings of the 11th European Conference on Computer Vision (ECCV), Crete, Greece, 2010.

[21] Yuan, J., Bae, E., and Tai, X. C., "A study on continuous max-flow and min-cut approaches," presented at the In Proceedings of IEEE Conf. on Computer Vision and Pattern Recognition (CVPR), San Francisco, CA 2010.

[22] Pineda, A. R., Reeder, S. B., Wen, Z., and Pelc, N. J., "Cramér-Rao bounds for three-point decomposition of water and fat," *Magn Reson Med,* vol. 54, pp. 625-635, 2005.

[23] Vigen, K., Francois, C., Yu, H., Shimakawa, A., Brittain, J., and Reeder, S., "Multi-Echo IDEAL Cardiac Water–Fat Imaging," presented at the In Proceedings of the 17th Annual Meeting of ISMRM, Honolulu, Hawaii 2009.

[24] Soliman, A. S., Yuan, J., Peters, T. M., and McKenzie, C. A., "3D Mapping of T2* and B0 Inhomogeneities for Water/Fat Separation," in *In Proceedings of the 21st Annual Meeting of ISMRM*, Salt Lake City, UT, 2013, p. 4227.

المنارة للاستشارات
www.manaraa.com

"If the facts don't fit the theory, change the facts"
- Einstein

Chapter 4

Fat Quantification Using an Interleaved Bipolar Acquisition[1]

4.1 Introduction

Multi gradient echo sequences have been widely used for chemical-shift encoded imaging, particularly water/fat separation. Images are acquired at several echo times (TE), where fat and water exhibit different phase shifts [1, 2]. The acquired images are subsequently post-processed to obtain water and fat components [3-9]. To achieve an accurate fat measurement, several confounding factors must be considered during the reconstruction process, particularly B0 magnetic field inhomogeneities [1, 2], T_2^* decay[10] , T1-bias [11], noise-related bias [11],

[1] This chapter is adapted from an article in submission to *Magnetic Resonance in Medicine*: Soliman, A.S., Wiens, C.N., Wade, T.P., Peters, T. M., and McKenzie, C. A., "Fat quantification Using an Interleaved Bipolar Acquisition", *Magnetic Resonance in Medicine* (2014).

المنارة للاستشارات
www.manaraa.com

temperature bias [12], and accurate spectral modeling of fat [13]. Typically, 6 echo-times are recommended for accurate fat measurement [13, 14].

On the acquisition side, parameters such as the flip angle, first echo time (TE_1), and echo spacing also influence the accuracy of the quantification. Low flip angles are usually recommended to reduce T_1-bias [11]. The echo combination (TE_1 and echo spacing) has significant impact on the signal-to-noise (SNR) performance and should be chosen carefully to avoid degraded SNR quality [15, 16]. Selection of TE_1 is restricted by the maximum gradient strength, the maximum achievable slew-rate during the readout pre-winder gradient and the time required for the RF pulse. Echo spacing varies with the selection of receiver bandwidth, spatial resolution, field of view (FOV) and gradient performance (slew rate and maximum gradient strength). It is important to choose an echo spacing that provides the best SNR performance [15, 16]. In addition, short echo spacing is desired to increase the range of frequency offsets in which water and fat components can be unambiguously distinguished during the reconstruction process [2].

Multi-echo acquisition can be achieved using either unipolar or bipolar readout gradients. In a unipolar acquisition, the echoes have the same readout polarity while in a bipolar acquisition the echoes are acquired with both positive and negative readout gradient polarities. Typically, fat quantification is performed using 6 unipolar readout gradients separated by flyback gradients [13, 14]. These long flyback gradients increase the minimum achievable echo spacing, heightening the ambiguity in identifying fat and water species. To achieve optimal echo spacing within an acceptable acquisition time, the echoes are often acquired in an interleaved fashion with multiple shots. For instance, the 6 echoes are acquired over 6/n repetition times (TR) (i.e. over 6/n shots), where n is the number of echoes per TR. This also increases the acquisition time. In a bipolar acquisition the flyback gradients are omitted and the 6 echoes alternate their polarities [17]. By removing the flyback gradients, shorter echo spacing can be achieved, often allowing the acquisition of all of the echoes at optimal echoes spacing in one repetition time (i.e. a

المنارة للاستشارات
www.manaraa.com

single shot). Consequently, a shorter scan time can be achieved. Therefore, bipolar acquisitions have higher SNR efficiency, as more of the scan time is spent in collecting the data. SNR efficiency is defined as the SNR normalized by the total acquisition time (SNR / sqrt(acquisition time)).

However, several challenges accompany bipolar sequences [17, 18]. First, phase errors induced by readout gradient delays and eddy currents can severely distort the reconstruction if not explicitly accounted for. Although these phase errors also exist in unipolar acquisitions, they add up to a fixed phase term on all the echoes. This does not disrupt the water/fat separation as the relative phase between the echoes remains unaffected. In bipolar acquisition, however, the phase errors are alternating their polarities between positive and negative readout gradients, causing severe artefacts in the water/fat separation process. Phase errors are induced in all spatial directions, but are dominated by a linear phase error in the readout direction. Resolving linear and high-order phase errors is essential for a correct water/fat separation [18]. A second challenge arises from the behaviour of the MRI receiver system. The receiver filters often have non-flat frequency response [18, 19]. Hence, a k-space point acquired with a negative readout gradient will be subject to a different frequency response than if it is acquired with a positive readout gradient. This causes an asymmetric amplitude modulation between negative and positive polarities along the readout direction. Finally, distortions caused by both the chemical-shift of fat signal and the magnetic field inhomogeneities appear in opposite directions for positive and negative echoes.

Existing approaches have been proposed to overcome these challenges. Yu *et al.* [18] performed phase and amplitude corrections for bipolar acquisitions using additional reference lines acquired with reversed polarities. However, the accuracy of the water/fat separation is limited by the number of acquired lines. In other words, errors can only be completely removed when full resolution reference lines are employed, which will double the acquisition time. The application of these corrections was only demonstrated for a qualitative 3-point water/fat separation.

المنارة للاستشارات
www.manaraa.com

The feasibility of fat quantification with 6-point bipolar acquisition was recently shown by Peterson *et al*. [20]. They performed a joint estimation of the phase and amplitude errors with the water/fat separation process in a least-squares estimation procedure. This technique lowers the expected number of signal averages (NSA) of the resulting water and fat components. In addition, the initial guess for the phase error was determined from the first three echoes; this phase map is vulnerable to 2D phase wraps as the employed 1D linear phase unwrapping might not be sufficient in clinical practice. The gradient-descent-based reconstruction is subject to the conventional drawback of the original IDEAL, where the field map estimation process can be trapped in a local minimum, swapping the water and fat signals.

In this work we propose a new multi-echo bipolar acquisition scheme that overcomes the induced phase and amplitude modulations. The proposed acquisition and reconstruction strategies eliminate the bipolar artefacts without requiring additional correction algorithms. The proposed technique is compared to the established unipolar acquisition as the reference for fat quantification. Experiments are performed on phantoms and *in vivo*, showing accurate fat measurements and higher SNR efficiency compared to unipolar sequences.

4.2 Theory

In a multi-gradient-echo bipolar acquisition, the polarity of the readout gradient alternates every other echo, such that odd echoes are acquired with positive readout gradient while even echoes acquired with negative readout. For instance, for a 6-echo acquisition, all k-space lines have positive polarity at TE_1, TE_3 and TE_5, and negative polarity in TE_2, TE_4 and TE_6. Representative pulse sequence diagrams of the unipolar and the conventional bipolar acquisitions are shown in Figure 4.1 (a) and (b), respectively. In this work, a new acquisition scheme is proposed, where all readout gradient waveforms alternate their polarities every other k-space line. In

المنارة للاستشارات
www.manaraa.com

other words, the odd-numbered phase-encode lines are acquired in (+ve, -ve, +ve, -ve, +ve, -ve) polarities, referred to as scheme 1 herein. For the even-numbered phase-encode lines, the polarities of the readout gradient are flipped (i.e. -ve, +ve, -ve, +ve, -ve, +ve), referred to as scheme 2. In this manner, each echo includes phase-encode lines acquired in both polarities. By separating positive and negative lines, two under-sampled datasets are obtained. For instance, if the acquisition was performed without acceleration, then each dataset will be subsampled by a factor of two. Parallel imaging reconstruction is then performed to produce two fully-sampled k-space data with opposite polarities. Additional calibration lines are required to perform the parallel imaging reconstruction as described later. The pulse sequence diagram is shown in Figure 4.2.

Following the reconstruction, a complex averaging of positive and negative datasets is obtained. This last step will overcome the alternating phase and magnitude errors between positive and negative acquisitions and can be described as follows:

Assuming S_o and S_e represent the signal acquired at the odd-numbered and even-numbered lines, respectively, such that

$$S_o(t_n) = S\, e^{i\theta\,(-1)^n} \tag{4.1}$$

$$S_e(t_n) = S\, e^{i\theta\,(-1)^{n+1}} \tag{4.2}$$

where

$$S = \left(\rho_W + \rho_F \,.\, \sum_{m=1}^{M} \alpha_m . e^{i2\pi\,\delta_m\,t_n}\right) . e^{i2\pi\,\Phi\,t_n}$$

Here, $\theta = \psi - i\gamma$ is a complex term representing phase (ψ) and magnitude (γ) errors [20], t_n (s) denotes the echo time (TE) ($n = 1, \ldots, 6$) of the acquired signal, ρ_W and ρ_F are the water and fat components, M is the number of peaks in the fat spectrum, δ_m (Hz) and α_m are the frequency and the amplitude of the m-th peak

المنارة للاستشارات
www.manaraa.com

respectively, and $\Phi = \varphi + i/(2\pi\, T_2^*)$ where φ is the local frequency offset. By averaging the positive and negative datasets:

$$\hat{S}(t_n) = \frac{S\left(e^{i\theta\,(-1)^n} + e^{i\theta\,(-1)^{n+1}}\right)}{2} = S\cos\theta \tag{4.3}$$

Hence the summation removes the alternating errors between even and odd echoes, while adding a constant error term instead on all the echoes that does not disrupt the water/fat separation process. This step removes the alternating phase/amplitude errors without a direct correction algorithm; therefore it is not susceptible to residual phase errors that might persist following any correction strategy causing biases in fat measurements.

To perform a self-calibrated parallel imaging reconstruction the centre lines of the k-space should be fully-acquired in a single readout polarity; otherwise the calibration lines would be disrupted by the phase/magnitude errors between the alternating polarities. However, for a complete cancelation of the alternating phase errors in Equation 4.3, the polarity of the readout gradient of the calibration lines should also match the polarity of the phase-encode lines. To achieve that, the centre lines of the k-space are fully-acquired with the two schemes, obtaining two sets of calibration lines, one of each polarity. From both schemes, only the calibration lines from a single echo time is needed for the reconstruction. Nevertheless, all the centre lines of the k-space from the 2 schemes at all the echoes are incorporated in the reconstruction for a further increase in the SNR. The workflow of the proposed technique is shown in Figure 4.3. It is important to notice that this acquisition scheme can be also combined with parallel imaging acceleration, where the interleaving strategy is performed only on the acquired (non-zero) lines.

Following Equation 4.3, water and fat components can be estimated from $\hat{S}$ using conventional field map estimation techniques that are employed with the unipolar sequences.

المنارة للاستشارات
www.manaraa.com

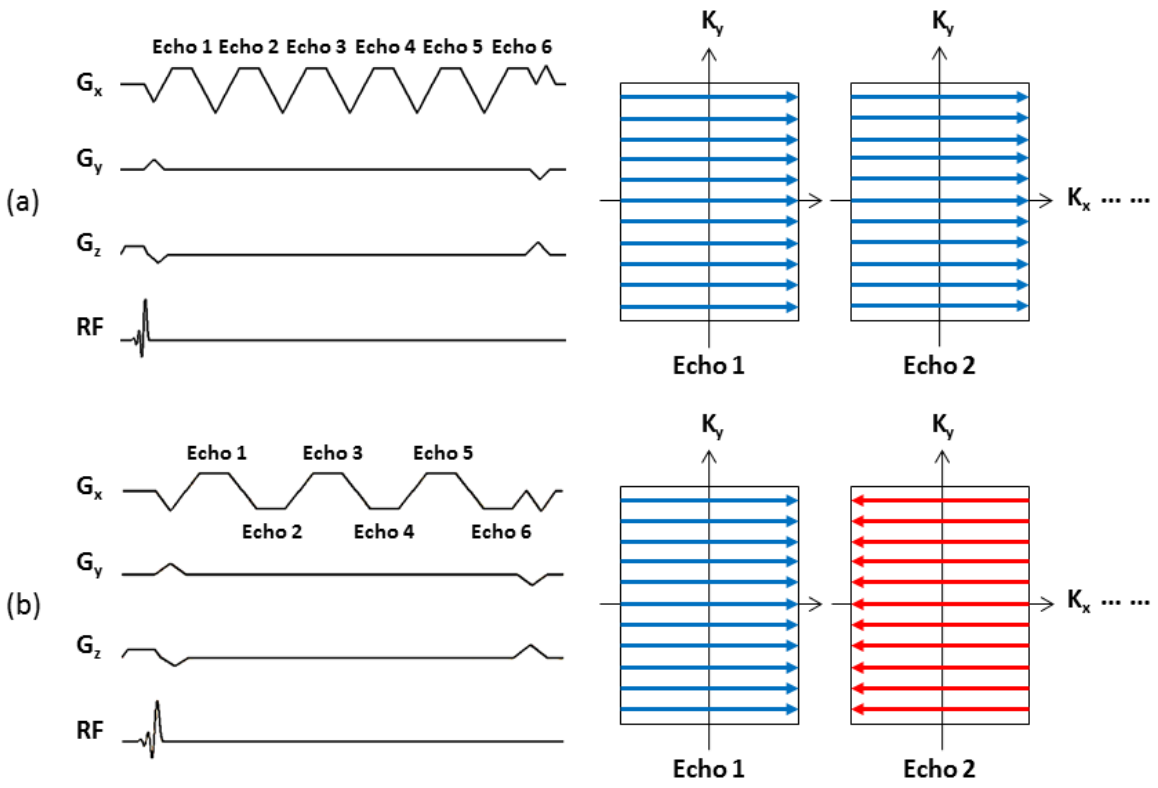

Figure 4.1: (a) A representative diagram of the unipolar sequence. All echoes are acquired with the same readout gradient polarity (positive). Here all echoes are acquired in a single TR (single shot). (b) A representative diagram of the conventional bipolar sequence. Odd echoes are acquired with positive polarities (blue arrows) while even echoes have negative polarities (red arrows). The bipolar acquisition in (b) necessitates employing post-processing phase and magnitude correction algorithms before water/fat separation.

المنارة للاستشارات
www.manaraa.com

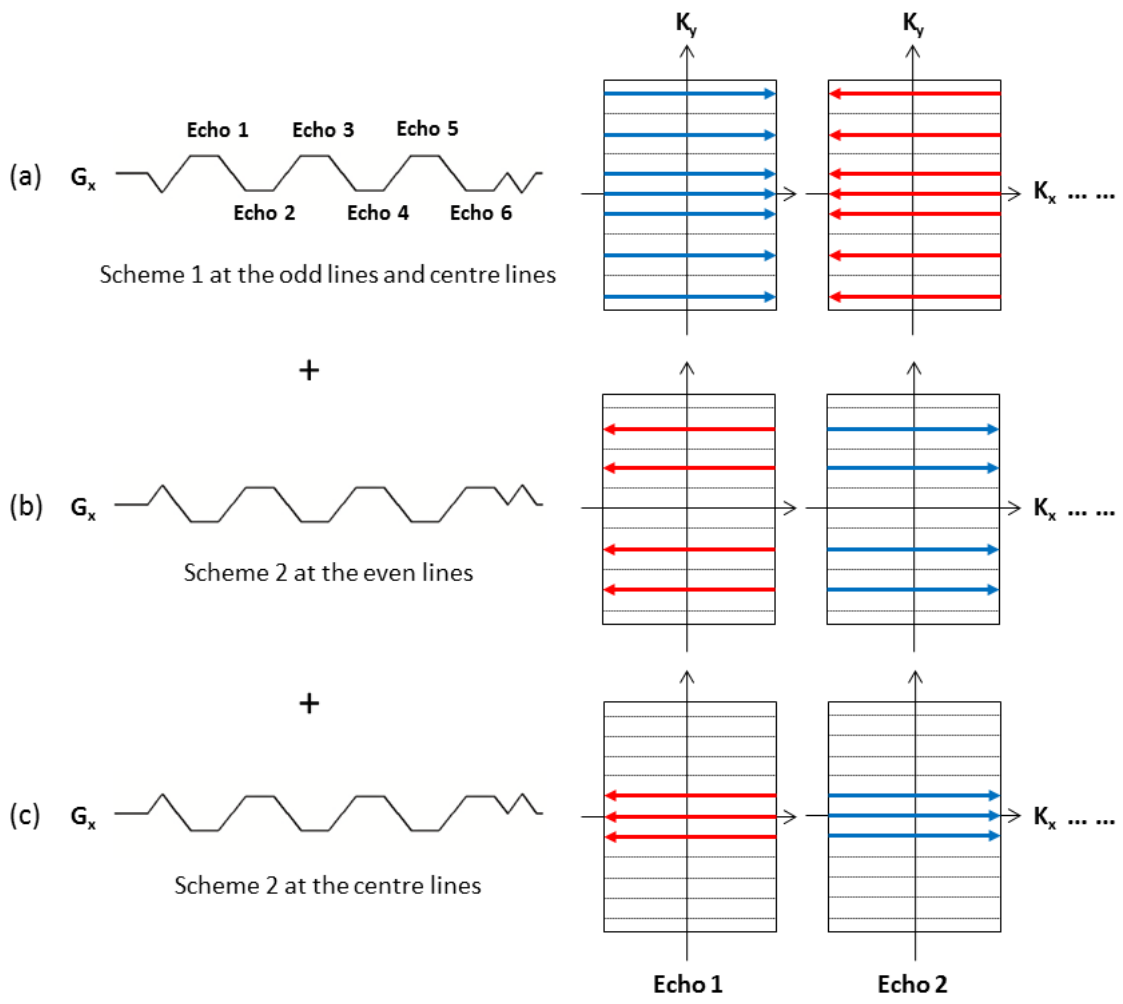

Figure 4.2: The proposed interleaved bipolar acquisition: Two bipolar schemes are employed, where scheme 1 has opposite polarity to scheme 2. The odd lines are acquired with scheme 1 while the even lines are acquired with scheme 2. The centre lines are fully-acquired with both schemes.

المنارة للاستشارات
www.manaraa.com

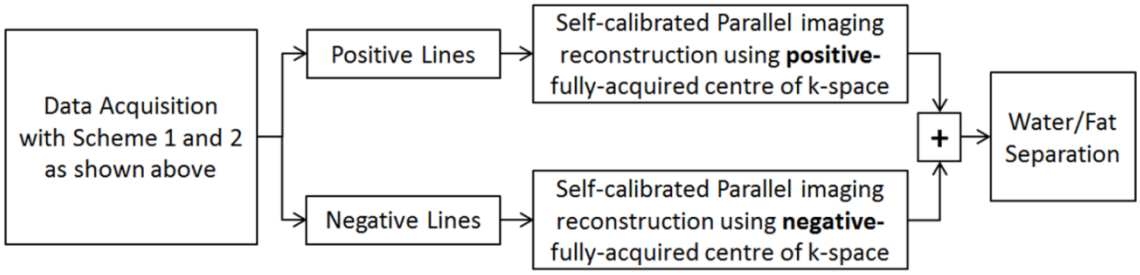

Figure 4.3: The reconstruction pipeline for the interleaved bipolar acquisition. The centre of k-space acquired with a positive polarity is used in the self-calibrated parallel imaging reconstruction of the positive lines, and vice-versa for the negative lines.

4.3 Methods

This work was carried out under approval granted by the Office of Research Ethics of Western University, Canada. All experiments were performed on a 3T MR (Discovery MR 750, GE Healthcare, Waukesha, WI). An investigational version of multi-echo 3D IDEAL-SPGR was modified to acquire data in an interleaved bipolar readout scheme. In all phantom and *in vivo* experiments, 6 echoes were acquired as recommended for accurate fat quantification [13]. Flip angle of 3° was used in all experiments to minimize the T_1-related bias [11]. Optimal echo-spacings were targeted in all the acquisitions to maximize the noise performance [15, 16]. Consequently, interleaved bipolar acquisitions were obtained in a single shot (echo-train-length =6), while 2 shots (echo-train length = 3) were used in unipolar acquisitions. The size of the additional calibration lines of all the interleaved bipolar acquisitions was fixed to ky x kz = 24 x 24 lines. For comparisons of SNR maps, a calibration centre of ky x kz = 24 x 24 was used in both unipolar and interleaved bipolar acquisitions.

المنارة للاستشارات
www.manaraa.com

Phantom experiments were performed with the interleaved bipolar sequence and compared to the unipolar sequence as an established reference. First, axial acquisition of a pure-water spherical phantom was obtained with both sequences using a head receive-only 8 coil-array at a bandwidth = ±142.86 kHz, acquisition matrix = 160x160x40, FOV=32 cm x 32 cm and slice thickness = 6 mm for both sequences. TR/TE1/ΔTE = 6.74/1.04/0.82 ms for the unipolar acquisition and 6.82/0.98/0.88 ms for the interleaved bipolar acquisition. The acquisition time was 86 s and 50 s for unipolar and interleaved bipolar acquisitions, respectively. Second, a phantom set with different fat fraction values was prepared from a mixture of agar and peanut oil as described in [21]. Five 60mL plastic vials were prepared with fat percentages of 0%, 5%, 10%, 20% and 100% respectively. Coronal acquisition of the phantoms were obtained using a torso receive-only 8 coil-array at a BW = ±100 kHz, acquisition matrix = 128x128x22, FOV=22 cm x 22 cm and slice thickness = 6 mm for both sequences. TR/TE1/ΔTE = 7.38/1.13/0.90 for the unipolar acquisition and 7.64/1.10/0.99 ms for the interleaved bipolar acquisition. The acquisition time was 42 s and 26 s for unipolar and interleaved bipolar acquisitions, respectively.

In vivo experiments were performed on 2 healthy volunteers where abdominal and knee datasets were acquired from each volunteer. For all experiments both unipolar and interleaved bipolar acquisitions were obtained.

An oblique knee dataset was acquired from volunteer (A) at approximately 10° from the sagittal plane along the S/I axis using a knee transmit-receive 8 coil-array at a BW=±142.86 kHz, FOV=24 cm x 18 cm, matrix size=160x144x40, slice thickness=3 mm for both sequences; TR/TE1/ΔTE = 8.75/1.33/1.13 ms and 10.57/1.4/1.06 ms for unipolar and interleaved bipolar acquisitions, respectively. The acquisition time was 122 s for unipolar and 56 s for interleaved bipolar, respectively. Another oblique knee dataset was acquired from volunteer (B) at approximately 15° from the sagittal plane using a knee transmit-receive 8 coil-array at a BW=±142.86 kHz, FOV=24 cm x 18 cm, matrix size=160x168x32 and slice thickness=4 mm for both sequences; TR/TE1/ΔTE = 10.95/1.47/1.108 ms and 8.51/1.29/1.104 ms for

المنارة للاستشارات
www.manaraa.com

unipolar and interleaved bipolar acquisitions, respectively. The acquisition time was 118 s for unipolar and 52 s for interleaved bipolar, respectively.

Whole-liver coverage was achieved in all the abdominal acquisitions and parallel imaging acceleration was used to keep the acquisition times within a ~25 s breath-hold. Abdominal data from volunteer (A) were acquired with a cardiac receive-only 8 coil-array at a BW=±125 kHz, FOV=36 cm x 27 cm, matrix size=160x120x24, slice thickness=8 mm for both sequences; TR/TE1/ΔTE = 5.36/0.82/0.65 ms and 7.1/0.91/0.96 ms for unipolar and interleaved bipolar acquisitions, respectively. Parallel imaging with an outer acceleration of 1.3x1 for unipolar and 1x1 interleaved bipolar was used for a total scan time of 25s for each sequence. Abdominal data from volunteer (B) was acquired with a torso receive-only 32 coil-array at a BW=±100 kHz, FOV=34 cm x 25.5 cm, matrix size=160x120x32, slice thickness=8 mm for both sequences; TR/TE1/ΔTE = 6.16/1.01/0.82 ms and 8.21/1.06/1.12 ms for unipolar and interleaved bipolar acquisitions, respectively. For an acquisition time of 25 s, an outer acceleration factor of 2x1.25 and 1.15x1.5 was used for unipolar and interleaved bipolar, respectively.

Following the separation of positive and negative phase-encode lines, conjugate-gradient SENSE [22] was used to reconstruct two fully-sampled datasets with opposite polarities. The first echo – which is positive in scheme 1 and negative in scheme 2 – was used for the self-calibration. A complex averaging of the two reconstructed sets was then performed. Magnetic field inhomogeneities were estimated from the averaged dataset using Max-IDEAL [7]. A complex multi-peak fitting with a single T_2^* decay was considered in the water/fat reconstruction. A pre-calibrated fat spectrum was used [13] with the frequency and amplitude values described in [7]. To compare the accuracy of fat quantification from the phantom experiments, noise-bias correction of the fat fraction maps were performed on both techniques [11]. Signal-to-noise maps were calculated using the generalized pseudo-replica method [23]. Three replicas of the acquired data were obtained offline by adding pseudo-random Gaussian noise, then the standard deviation of the noise

المنارة للاستشارات
www.manaraa.com

variations in space ([7x7x5] neighborhood) and through the replicas were used to calculate the SNR maps [23]. In all experiments, noise-only scans were acquired at the same bandwidths and amplitude gains as the corresponding unipolar and interleaved bipolar acquisitions, in order to correctly calculate and scale the noise covariance matrix [23, 24].

4.4 Results

Figure 4.4 shows the fat fraction images from a pure-water sphere acquired using unipolar and bipolar acquisitions. As shown in Figure 4.4, phase errors from the readout gradient cause fat fraction bias in the unipolar acquisition; this effect is not observed in the interleaved bipolar sequence. Phase errors occur in the unipolar acquisition from either eddy-currents or other imperfections of the MRI gradients. However, in the interleaved bipolar acquisition, these errors have opposite polarities from positive and negative readout gradients; hence they cancelled out through the complex summation, resulting in correct fat fraction measurements without requiring additional correction steps.

Fat quantification from unipolar and interleaved bipolar acquisitions was performed on selected ROIs on the fat fraction images as shown in Figure 4.5 (a), where the same ROIs were used in both experiments. Figure 4.5 (b) shows the error in fat fraction measurement (True fat fraction – measured fat fraction) from both sequences after performing the noise-bias correction. The results of the interleaved bipolar acquisition demonstrated accurate fat measurements without further correction algorithms. It is worth noting that the standard deviation of the errors was slightly larger in the interleaved bipolar results than the unipolar sequence. This can be expected as the reconstruction pipeline of the interleaved bipolar subsamples the data which results in a g-factor induced SNR loss.

المنارة للاستشارات
www.manaraa.com

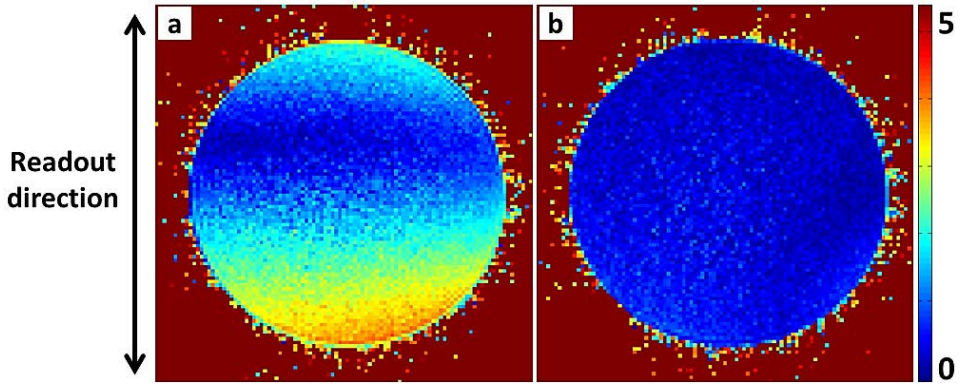

Figure 4.4: Fat fraction images (ranging from 0% to 5%) of a pure-water phantom from unipolar (a) and interleaved bipolar (b) axial acquisitions. Phase errors from the readout gradient cause fat fraction bias in the unipolar acquisition, while the errors were negligible in the interleaved bipolar results.

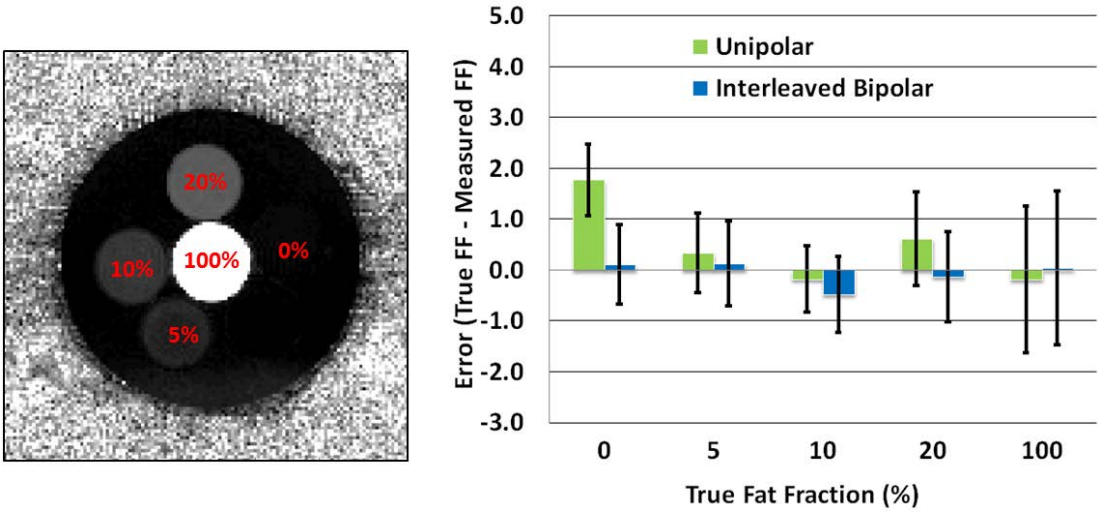

Figure 4.5: Results from a coronal acquisition of the phantom set. (a) Fat fraction map of the phantom set with the locations of the 5 vials of different fat fractions indicated. (b) Differences between the true and the measured values from the two sequences, demonstrating accurate fat quantification obtained using the interleaved bipolar compared to the unipolar sequence.

المنارة للاستشارات
www.manaraa.com

Figure 4.6 demonstrates the efficiency of the interleaved bipolar sequence for *in vivo* applications. Water and fat images with their corresponding SNR efficiency maps from oblique knee acquisitions from volunteer (B) are shown. The interleaved bipolar sequence demonstrated higher SNR efficiency compared to the unipolar sequence. Excellent water/fat separation that does not suffer from phase/amplitude errors was obtained with the proposed technique. As shown in the figure, two ROIs were selected on the fat fraction maps to compare the fat quantification results. Fat fractions in ROI #1 were 1.28 ± 3.4 and 1.48 ± 3.9 in the unipolar and interleaved bipolar acquisitions respectively, while ROI #2 values recorded 96.84 ± 3.6 and 96.76 ± 3.5, respectively. The interleaved bipolar technique can therefore produce accurate fat fraction maps in a significantly shorter acquisition time compared to the unipolar sequence (52 s vs. 118 s) in a fully sampled acquisition.

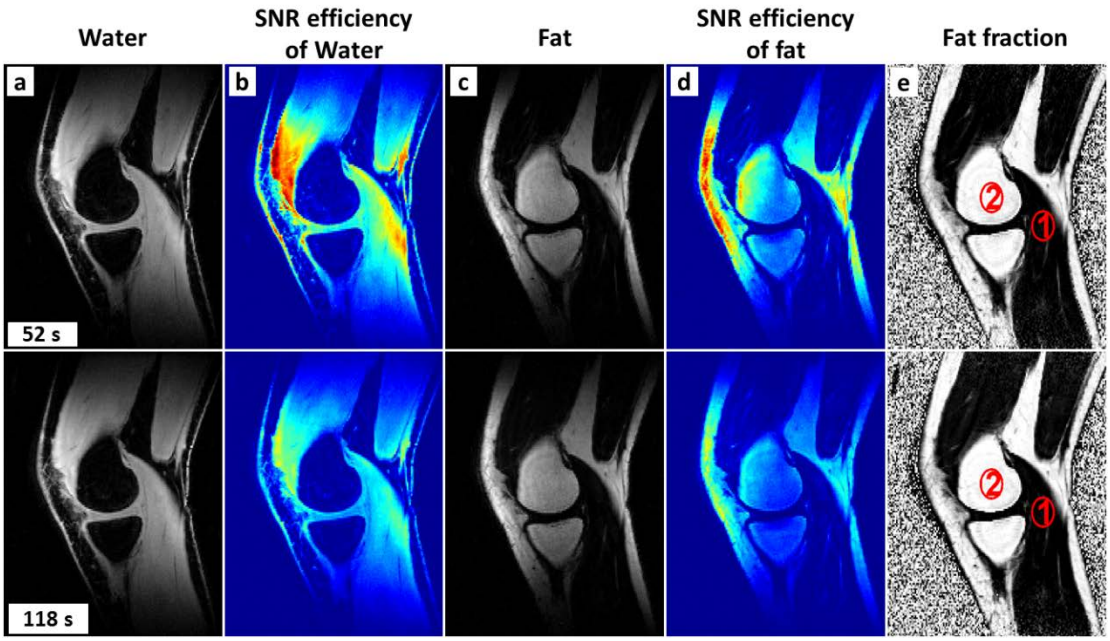

Figure 4.6: Water and fat images of a volunteer's knee were obtained with the interleaved bipolar (upper row) and the unipolar sequence (lower row). SNR efficiency maps in (b) and (d) are scaled from [0, 1]. The 2 ROIs in (e) were used for the fat quantification results reported in the text, and demonstrated that accurate fat fractions were obtained with the 2 sequences. However, the SNR efficiency maps (b and d) show that higher SNR efficiency was obtained with the bipolar sequence.

المنارة للاستشارات
www.manaraa.com

Abdominal acquisitions from volunteer (A) are shown in Figure 4.7. Whole-liver coverage was achieved in a single ~25 s breath-hold with each sequence by adjusting acceleration factors. Excellent water/fat separation that does not suffer from phase/amplitude errors was obtained with the interleaved bipolar sequence. As shown in Figure 4.7, an ROI is selected in the liver to compare the quantification results. The fat fraction was 3.92 ± 2.2 and 3.00 ± 1.8 in the unipolar and interleaved bipolar acquisitions, respectively. Accurate fat fraction maps obtained from the interleaved bipolar sequence compared to the standard unipolar acquisition.

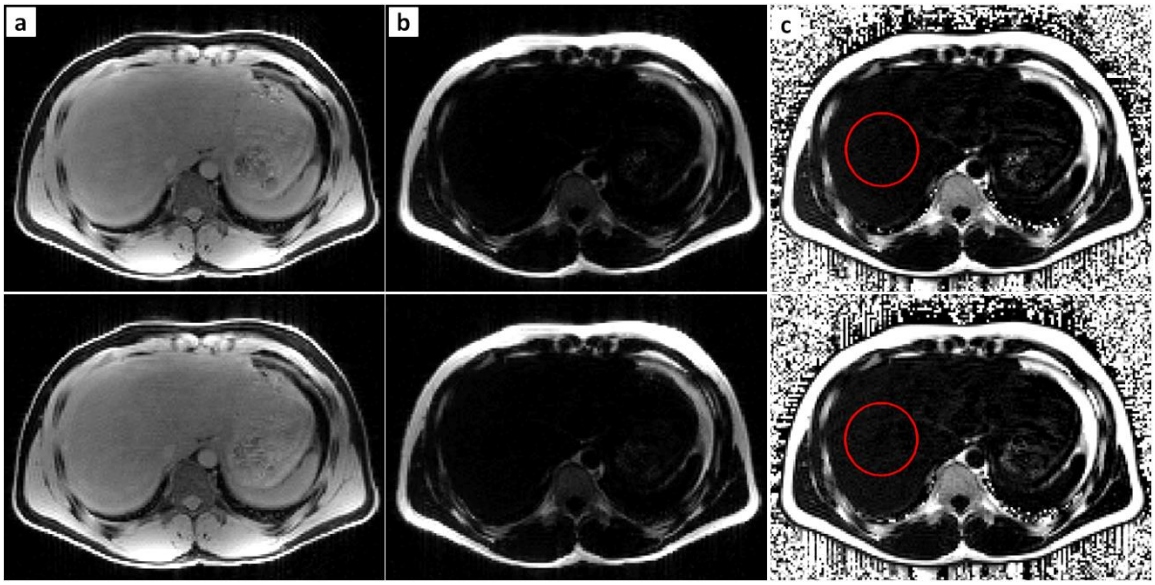

Figure 4.7: (a) Water, (b) fat and (c) fat fraction maps of a whole-liver acquisition from the interleaved bipolar (upper row) and the unipolar (lower row) sequences, respectively. The ROIs selected in the liver in (c) were used for the fat quantification results reported in the text, and demonstrated that accurate fat fraction was obtained with the interleaved bipolar sequence.

المنارة للاستشارات
www.manaraa.com

As the interleaved bipolar acquisition is implicitly faster than its corresponding unipolar sequence, so less parallel imaging acceleration is needed during the acquisition and higher SNR can be achieved as shown in Figure 4.8. The SNR in the liver was ~30% higher in the water image using the proposed sequence. It is worth noting that the echo-timing of the interleaved bipolar acquisition (TE1/ΔTE) is expected to achieve lower noise performance than its corresponding unipolar acquisition [16], particularly at low fat fractions; however the SNR gain from the efficiency of the interleaved bipolar is still remarkably higher than the unipolar acquisition.

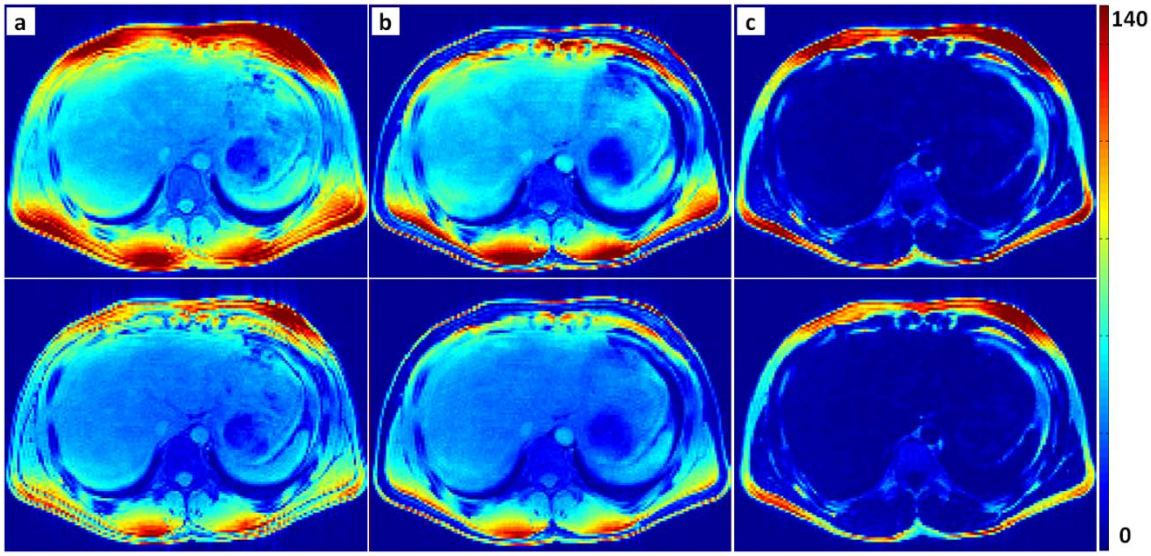

Figure 4.8: SNR maps of the 2nd echo (a), the water (b) and the fat (c) images from the interleaved bipolar (upper row) and the unipolar (lower row) sequences, respectively. Higher SNR was obtained in all the images with the proposed bipolar sequence.

المنارة للاستشارات
www.manaraa.com

4.5 Discussion

We demonstrated a new multi-echo bipolar acquisition and reconstruction technique that does not require phase nor magnitude corrections. The interleaved bipolar acquisition is more SNR efficient than the current established unipolar sequence. The efficiency of the sequence resides from: 1) the removal of fly-back gradients; 2) its ability to acquire the 6 echoes within the optimal range of echo spacing in a single TR at 3 Tesla, while 2 shots are required in the unipolar sequence to achieve similar noise performance. The efficiency of the interleaved bipolar is more significant at high bandwidth and small FOVs where the fly-back gradients of the unipolar sequence further prolong the acquisition time. For time-restricted acquisitions, the proposed acquisition offers higher SNR than its corresponding unipolar version. As shown in the abdominal examples, whole-liver coverage in a single breath-hold (~25 s) required lower parallel imaging acceleration than the unipolar acquisition, so higher SNR was achieved. It is worth noting that in order to mitigate SNR losses from increasing g-factor, higher acceleration is used in the slice direction first, as the reconstruction method implicitly introduces an additional subsampling of 2 in the phase-encode direction.

Another advantage of the interleaved bipolar technique is that it significantly reduces the phase errors induced in the unipolar acquisition (Figure 4.4), where additional correction of the acquired data is required before performing the water/fat separation process. It is worth noting that the induced phase errors depend on the selected physical axis used in the readout. We noticed that these errors are negligible when the readout direction is on the Z-axis (head-foot direction) and therefore coronal acquisitions were performed in Figure 4.5 for comparisons of fat fractions. Finally, the complex addition markedly reduces the residual aliasing remaining after parallel imaging reconstruction. Data reconstructed from each readout polarity have similar aliasing artifacts but with opposite phases [25], hence the residual aliasing is cancelled after the complex summation.

المنارة للاستشارات
www.manaraa.com

The proposed technique is limited to coil-arrays as the reconstruction pipeline implicitly decimates the data by a factor of 2 and uses parallel MRI to reconstruct two fully sampled datasets. However, this limitation is not significant given the widespread usage of coil-arrays in clinical practice. It is important to notice that as the reconstruction pipeline implicitly undersamples the data in the phase-encode direction, the selection of phase and slice-encode directions should be carefully performed even in the unaccelerated acquisitions, in order to minimize the residual aliasing of the parallel MRI reconstruction. Another drawback of the proposed technique is that an additional acquisition of the center of k-space is required for the reconstruction, which increases the total acquisition time. Nevertheless, a further improvement in the SNR is also obtained as the additional lines are included in the reconstruction process. Also the total scan time is still less than the unipolar acquisition. Finally, we noticed that residual phase errors might remain after the complex summation step at the locations of low signal; this has only occurred at the edges of the coil where typically low signal is received.

4.6 Conclusion

A new bipolar acquisition strategy that provides accurate fat quantification in shorter scan time has been demonstrated. The interleaved bipolar sequence is shown to be more efficient for fat quantification as it benefits from the advantages of bipolar readouts, while producing fat measurements as accurate as the well-established unipolar acquisitions. The proposed acquisition and reconstruction technique compensates for the alternating phase and amplitude errors without requiring correction algorithms. Phantoms and *in vivo* experiments were conducted and accurate fat fraction maps with higher SNR efficiency were demonstrated.

المنارة للاستشارات
www.manaraa.com

Acknowledgments

We thank Ann Shimakawa from GE Healthcare for valuable discussions. We acknowledge funding from the NSERC Computer-Assisted Medical Intervention (CAMI) program. C.A. McKenzie holds the Canada Research Chair in Translational Magnetic Resonance Imaging at Western University. This research was undertaken, in part, thanks to funding from the Canada Research Chairs Program and GE Healthcare.

المنارة للاستشارات
www.manaraa.com

References

[1] Glover, G. H. and Schneider, E., "Three-point dixon technique for true water/fat decomposition with B0 inhomogeneity correction," *Magnetic resonance in medicine,* vol. 18, pp. 371-383, 1991.

[2] Reeder, S. B., Pineda, A. R., Wen, Z., Shimakawa, A., Yu, H., Brittain, J. H.*, et al.*, "Iterative decomposition of water and fat with echo asymmetry and least-squares estimation (IDEAL): Application with fast spin-echo imaging," *Magn Reson Med,* vol. 54, pp. 636-644, 2005.

[3] Tsao, J. and Jiang, Y., "Hierarchical IDEAL: Fast, robust, and multiresolution separation of multiple chemical species from multiple echo times," *Magn Reson Med,* vol. 70, pp. 155-159, 2013.

[4] Soliman, A. S., Yuan, J., White, J. A., Peters, T. M., and McKenzie, C. A., "A Convex Relaxation Approach to Fat/Water Separation with Minimum Label Description," in *Lecture Notes in Computer Science*. vol. 7511 N. Ayache, H. Delingette, P. Golland, and K. Mori, Eds., ed: Springer Berlin Heidelberg, 2012, pp. 519-526.

[5] Hernando, D., Kellman, P., Haldar, J. P., and Liang, Z. P., "Robust water/fat separation in the presence of large field inhomogeneities using a graph cut algorithm," *Magn Reson Med,* vol. 63, pp. 79-90, 2010.

[6] Reeder, S. B., Wen, Z., Yu, H., Pineda, A. R., Gold, G. E., Markl, M.*, et al.*, "Multicoil Dixon chemical species separation with an iterative least-squares estimation method," *Magn Reson Med,* vol. 51, pp. 35-45, 2004.

[7] Soliman, A. S., Yuan, J., Vigen, K. K., White, J. A., Peters, T. M., and McKenzie, C. A., "Max-IDEAL: A max-flow based approach for IDEAL water/fat separation," *Magnetic Resonance in Medicine,* vol. 72, pp. 510-521, 2014.

المنارة للاستشارات

www.manaraa.com

[8] Berglund, J. and Kullberg, J., "Three-dimensional water/fat separation and T2* estimation based on whole-image optimization - Application in breathhold liver imaging at 1.5 T," *Magn Reson Med,* vol. 67, pp. 1684-1693, 2012.

[9] Yu, H., Reeder, S. B., Shimakawa, A., McKenzie, C. A., and Brittain, J. H., "Robust multipoint water-fat separation using fat likelihood analysis," *Magn Reson Med,* vol. 67, pp. 1065-1076, 2012.

[10] Yu, H., McKenzie, C. A., Shimakawa, A., Vu, A. T., Brau, A., Beatty, P. J.*, et al.*, "Multiecho reconstruction for simultaneous water-fat decomposition and T2* estimation," *J Magn Reson Imaging,* vol. 26, pp. 1153-1161, 2007.

[11] Liu, C. Y., McKenzie, C. A., Yu, H., Brittain, J. H., and Reeder, S. B., "Fat quantification with IDEAL gradient echo imaging: correction of bias from T1 and noise," *Magn Reson Med,* vol. 58, pp. 354-364, 2007.

[12] Hernando, D., Sharma, S. D., Kramer, H., and Reeder, S. B., "On the confounding effect of temperature on chemical shift-encoded fat quantification," *Magn Reson Med,* 2013. doi:10.1002/mrm.24951.

[13] Yu, H., Shimakawa, A., McKenzie, C. A., Brodsky, E., Brittain, J. H., and Reeder, S. B., "Multiecho water-fat separation and simultaneous R2* estimation with multifrequency fat spectrum modeling," *Magn Reson Med,* vol. 60, pp. 1122-1134, 2008.

[14] Hines, C. D. G., Frydrychowicz, A., Hamilton, G., Tudorascu, D. L., Vigen, K. K., Yu, H.*, et al.*, "T1 independent, T2* corrected chemical shift based fat-water separation with multi-peak fat spectral modeling is an accurate and precise measure of hepatic steatosis," *J Magn Reson Imaging,* vol. 33, pp. 873-881, 2011.

[15] Chebrolu, V. V., Yu, H., Pineda, A. R., McKenzie, C. A., Brittain, J. H., and Reeder, S. B., "Noise analysis for 3-point chemical shift-based water-fat separation with spectral modeling of fat," *J Magn Reson Imaging,* vol. 32, pp. 493-500, 2010.

المنارة للاستشارات
www.manaraa.com

[16] Hernando, D., Hines, C. D. G., Yu, H., and Reeder, S. B., "Addressing phase errors in fat-water imaging using a mixed magnitude/complex fitting method," *Magn Reson Med,* vol. 67, pp. 638–644, 2012.

[17] Lu, W., Yu, H., Shimakawa, A., Alley, M., Reeder, S. B., and Hargreaves, B. A., "Water-fat separation with bipolar multiecho sequences," *Magn Reson Med,* vol. 60, pp. 198-209, 2008.

[18] Yu, H., Shimakawa, A., McKenzie, C. A., Lu, W., Reeder, S. B., Hinks, R. S.*, et al.*, "Phase and amplitude correction for multi-echo water--fat separation with bipolar acquisitions," *J Magn Reson Imaging,* vol. 31, pp. 1264-1271, 2010.

[19] Delakis, I., Petala, K., and De Wilde, J. P., "MRI receiver frequency response as a contributor to Nyquist ghosting in echo planar imaging," *Journal of Magnetic Resonance Imaging,* vol. 22, pp. 324-328, 2005.

[20] Peterson, P. and Månsson, S., "Fat quantification using multiecho sequences with bipolar gradients: Investigation of accuracy and noise performance," *Magn Reson Med,* vol. 71, pp. 219-229, 2014.

[21] Hines, C. D. G., Yu, H., Shimakawa, A., McKenzie, C. A., Brittain, J. H., and Reeder, S. B., "T1 independent, T2* corrected MRI with accurate spectral modeling for quantification of fat: Validation in a fat-water-SPIO phantom," *J Magn Reson Imaging,* vol. 30, pp. 1215-1222, 2009.

[22] Pruessmann, K. P., Weiger, M., Börnert, P., and Boesiger, P., "Advances in sensitivity encoding with arbitrary k-space trajectories," *Magn Reson Med,* vol. 46, pp. 638-651, 2001.

[23] Wiens, C. N., Kisch, S. J., Willig-Onwuachi, J. D., and McKenzie, C. A., "Computationally rapid method of estimating signal-to-noise ratio for phased array image reconstructions," *Magn Reson Med,* vol. 66, pp. 1192-1197, 2011.

المنارة للاستشارات
www.manaraa.com

[24] Kellman, P. and McVeigh, E. R., "Image reconstruction in SNR units: A general method for SNR measurement," *Magnetic resonance in medicine,* vol. 54, pp. 1439-1447, 2005.

[25] Xiang, Q.-S. and Ye, F. Q., "Correction for geometric distortion and N/2 ghosting in EPI by phase labeling for additional coordinate encoding (PLACE)," *Magn Reson Med,* vol. 57, pp. 731-741, 2007.

المنارة للاستشارات

www.manaraa.com

"Do what you can, with what you have, where you are"
- Theodore Roosevelt

Chapter 5

An Efficient Chemical-shift Encoded Acquisition for *in-vivo* Applications[1]

5.1 Introduction

Obesity represents a huge burden on the healthcare system in Canada and worldwide. Measuring and localizing the distribution of fat in the human body is important for obesity-related research. For example, it was shown that the visceral fat in the body is a better and independent predictor for obesity-related diseases than total the Body Mass Index (BMI) [1]. Chemical-shift imaging has been therefore employed in this task for its ability to separate the fat component from the water. It has been used to visualize and quantify the distribution of fat in various human organs [2-12]. Applications include measuring the total body fat [13] and separating

[1] This chapter is adapted from an article currently in submission: Soliman, A.S., Friesen-Waldner, L.J., Sinclair, K.J., Regnault, T.R.H., Peters, T.M., and McKenzie, C.A. An Efficient Chemical-shift Encoded Acquisition for in-vivo Applications. *Journal of Magnetic Resonance Imaging* (2014).

المنارة للاستشارات
www.manaraa.com

different abdominal fat compartments such as visceral and subcutaneous fat depots [14].

Animal models are extensively used to research human obesity for ethical and practical reasons. For example, animals can be regulated on specific diets while monitoring the accompanying anatomical and physiological changes over time on different organs. Animal models allow better regulated observation of the effects of obesity with fewer barriers to research than in humans. Furthermore, they have short generation time, which allows studying the effect of obesity over several generations. Mice, rats hamsters, rabbits and guinea pigs can be used as experimental models, where the disease to be investigated is experimentally induced in the healthy animal for further study.

Guinea pigs models are used in obesity research due to their similarity to humans in regard to metabolic aspects [15, 16]. For example, they show evidences of similar hepatic cholesterol concentrations and synthesis as humans. Guinea pigs models are used to study the effect of different dietary fat and cholesterol on hepatic metabolism [17-19], lipid accumulation [20], lipoprotein metabolism [15], whole body and hepatic cholesterol synthesis [21], atherosclerosis [15, 16], metabolic syndrome [17] and type-II diabetes mellitus [16]. They accumulate adipose tissue during intrauterine life similar to human fetuses [22], and hence they become a suitable model to explore human adiposity, particularly in early stages of life.

Chemical-shift encoded water/fat imaging has been previously utilized for fat quantification in the animal model [23-28]. Multi-echo gradient echo sequences are usually used, where 6 echoes are acquired as recommended for fat quantification [23, 27, 29]. As discussed in Chapter 4 these acquisitions often employ unipolar readout gradients, which are less efficient than bipolar acquisitions.

المنارة للاستشارات
www.manaraa.com

In Chapter 4, a new bipolar acquisition/reconstruction strategy for water/fat imaging was proposed. The technique demonstrated its efficiency and its accuracy in phantom and human experiments. In this chapter we will utilize our new bipolar sequence in animal experiments, allowing the acquisition of all the echoes within approximately half the acquisition time of the unipolar sequence. Additionally, we show that the interleaved bipolar sequence can acquire the data with higher resolution (approximately half the voxel size) within the same time frame as conventional unipolar sequences. Moreover, we compare the SNR maps of both sequences, demonstrating the efficiency of the interleaved bipolar sequence. Alternatively, the number of echoes can be doubled using the proposed bipolar sequence, benefiting from the short acquisition time. This chapter widens the scope through which we can benefit from the proposed bipolar sequence, by proving its efficiency in animal models.

5.2 Methods and Experiments

5.2.1 MRI Acquisition

The experiments were carried out under ethical approval granted by the Animal Use Subcommittee of the Office of Research Ethics at Western University, Canada. Four guinea pigs, born in our facility, were fed a normal chow diet since birth. MRI scanning was performed on the animals at approximately 3 months of age. In preparation for scanning, the guinea pigs were anesthetized with isoflurane (4% initially and maintained at 1.5 to 2% isoflurane with oxygen) and a catheter was inserted into a vein in the foot. Breathing rate and temperature were monitored and held constant throughout the experiment. All experiments were performed on a 3T MR system (Discovery MR 750, GE Healthcare, Waukesha, WI). Both unipolar and interleaved bipolar acquisitions were performed on all the animals using a cardiac receive-only 32 coil array. An investigational version of multi-echo 3D IDEAL-SPGR was modified to acquire data in an interleaved bipolar readout scheme, as shown in

المنارة للاستشارات
www.manaraa.com

Chapter 4. We used a unipolar sequence adapted from a protocol employed in measuring hepatic fat fraction in guinea pigs [27]. Similar echo spacings were targeted in all comparisons in order to achieve same noise performance [30-33]. Consequently, all interleaved bipolar acquisitions were obtained in a single shot (echo-train-length =6), while 2 shots (echo-train length = 3) were used in all unipolar acquisitions. The size of the additional calibration lines of all the interleaved bipolar acquisitions was fixed to ky x kz = 28 x 28 lines. T_1-related bias was minimized in all acquisitions by using low flip angle (= 3°). Four acquisitions were performed on each guinea pig as follows:

A. A 6-echo unipolar acquisition with ETL=3, TR/TE1/ΔTE = ~13.0/1.22/1.02 ms, FOV = 26 cm x 15.6 cm, flip angle = 3 °, slice thickness = 0.9 mm, bandwidth = ± 142.86 KHz, number of excitations (NEX) = 3. Whole animal coverage was achieved using an acquisition matrix = 276 x 182 x 84 for guinea pigs 1 and 2, and 276 x 182 x 88 for guinea pigs 3 and 4. Therefore the voxel dimensions were 0.94 x 0.86 x 0.9 mm^3 (voxel size = 0.728 mm^3). Parallel imaging acceleration was not used. Total acquisition time was approximately 20 mins.

B. A 6-echo interleaved bipolar acquisition with ETL = 6, TR/TE1/ΔTE = ~13.0/1.25/1.29 ms. All other acquisition parameters are the same as the unipolar sequence in (A). Parallel imaging acceleration was not used. Total acquisition time was approximately 10 mins.

C. A 6-echo unipolar acquisition with an outer acceleration factor of 1.42 x 1.42 to achieve similar acquisition time as the interleaved bipolar in (B). All other acquisition parameters were kept the same as in (A).

D. A high resolution 6-echo interleaved bipolar acquisition, where the spatial resolution of the bipolar sequence (B) was increased till the acquisition time equals the unipolar sequence (A) (i.e. ~20 mins). Here we considered the acquisition time of the unipolar sequence in (A) as the baseline, and we

المنارة للاستشارات
www.manaraa.com

therefore utilized the short acquisition time of the bipolar sequence in (B) to obtain higher spatial resolution. Whole animal coverage was achieved using acquisition matrix = 276 x 278 x 108 for guinea pigs 1 and 2, and = 276 x 278 x 112 for guinea pigs 3 and 4, with slice thickness of 0.7 mm for all 4 guinea pigs. The voxel dimensions were 0.94 x 0.56 x 0.7 mm^3 (voxel size = 0.368 mm^3). All other acquisition parameters were kept the same as in (B).

As noted, the resolution is doubled in (D) as the voxel volume is approximately half the size of that in (A). It is important to notice that in order to preserve similar echo-spacing as the unipolar sequence in (A), the resolution was only increased in the phase- and slice-encode directions. This will preserve similar noise performance between the sequences in comparisons (i.e. A and D) [30-33].

We found that the size of the acquired data from the high resolution interleaved bipolar sequence in (D) was too large to be handled by the current available processing unit. Hence, only half the number of slices prescribed in (D) was acquired for each guinea pig, while the number of excitations (NEX) was set to 6 (instead of 3 originally) to compensate for the loss of SNR resulting from acquiring half the prescribed slice-encodes. Consequently the acquisition time was kept at ~20 mins as prescribed. In all experiments, noise-only scans were acquired at the same bandwidths and amplitude gains as the corresponding unipolar and interleaved bipolar sequences, in order to correctly calculate and scale the noise covariance matrix [34, 35].

المنارة للاستشارات
www.manaraa.com

5.2.2 Water/Fat Reconstruction

The acquired raw data were processed on an Intel i7 CPU with 6-cores @ 3.2 GHz and 48 GB of RAM. The interleaved bipolar acquisitions were reconstructed as described in Chapter 4. Positive and negative lines were separately processed using Conjugate-gradient SENSE reconstruction [36]. The resulting positive and negative datasets were complex-added and then fed into Max-IDEAL [37, 38] to generate water and fat components. T_2^* decay and accurate fat spectrum were both included in the reconstruction to minimize the related-bias [11, 29, 39, 40], as well as to avoid water/fat swaps [37]. A pre-calibrated fat spectrum was used with the frequency and amplitude values described in [37]. The inclusion of T_2^* effect in the Max-IDEAL labeling stage was done using 4 initial T_2^* values: 5, 10, 50 and 60 ms. The smoothing parameter β was set to 1.5 in all unipolar and bipolar experiments. All other parameters of MAX-IDEAL were kept at the default values described in [37]. The Potts labeling stage in Max-IDEAL was accelerated on a graphics processing unit (GPU) NVIDIA GeForce GTX 660 with 960 CUDA cores. SNR maps were calculated using the generalized pseudo-replica method [35]. Normalized SNR efficiency maps were calculated by normalizing for the acquisition time and for the voxel dimensions.

المنارة للاستشارات
www.manaraa.com

5.3 Results

Water and fat components were successfully reconstructed from all unipolar and interleaved bipolar sequences from the 4 guinea pigs. In the first experiment the scan was interrupted to double-check the vital signs of the guinea pig; the MR table was moved out and the animal was re-located. The noise scan was not employed in the SNR calculation of this experiment. In the same experiment, we found that the high resolution sequence described in (D) produced a raw-data file with a size that exceeded the maximum available storage disk mounted on the MR console machine. Hence, sequence (D) for the first guinea pig was repeated in a separate day after replacing the hard drive, and its SNR measure was excluded from the comparisons. SNR efficiency maps of all 4 sequences were calculated for the other 3 animals using the noise covariance matrix. To compare the high resolution sequence (D) with the other sequences, we manually selected the closest slice with similar anatomy to the other sequences.

In all comparisons, the interleaved bipolar sequences (B and D) have consistently demonstrated higher SNR efficiency for water and fat components compared to the unipolar sequences (A and C). An exception to that is around the diaphragm where the respiratory motion artifacts cause noticeable SNR drop (See Discussion section).

A typical example is presented in Figures 5.1-5.3. The water component with corresponding SNR efficiency maps from each of the 4 sequences are shown in Figure 5.1. Similarly, the fat component and its SNR efficiency are shown in Figure 5.2. In all comparisons, the accelerated unipolar sequence has the lowest SNR efficiency (sequence C) while the high resolution interleaved bipolar (sequence D) shows the highest efficiency. As shown in Figures 5.3, accurate fat fraction maps from the interleaved bipolar sequences were also obtained. Phase and magnitude errors were completely negligible in all the bipolar acquisitions.

المنارة للاستشارات
www.manaraa.com

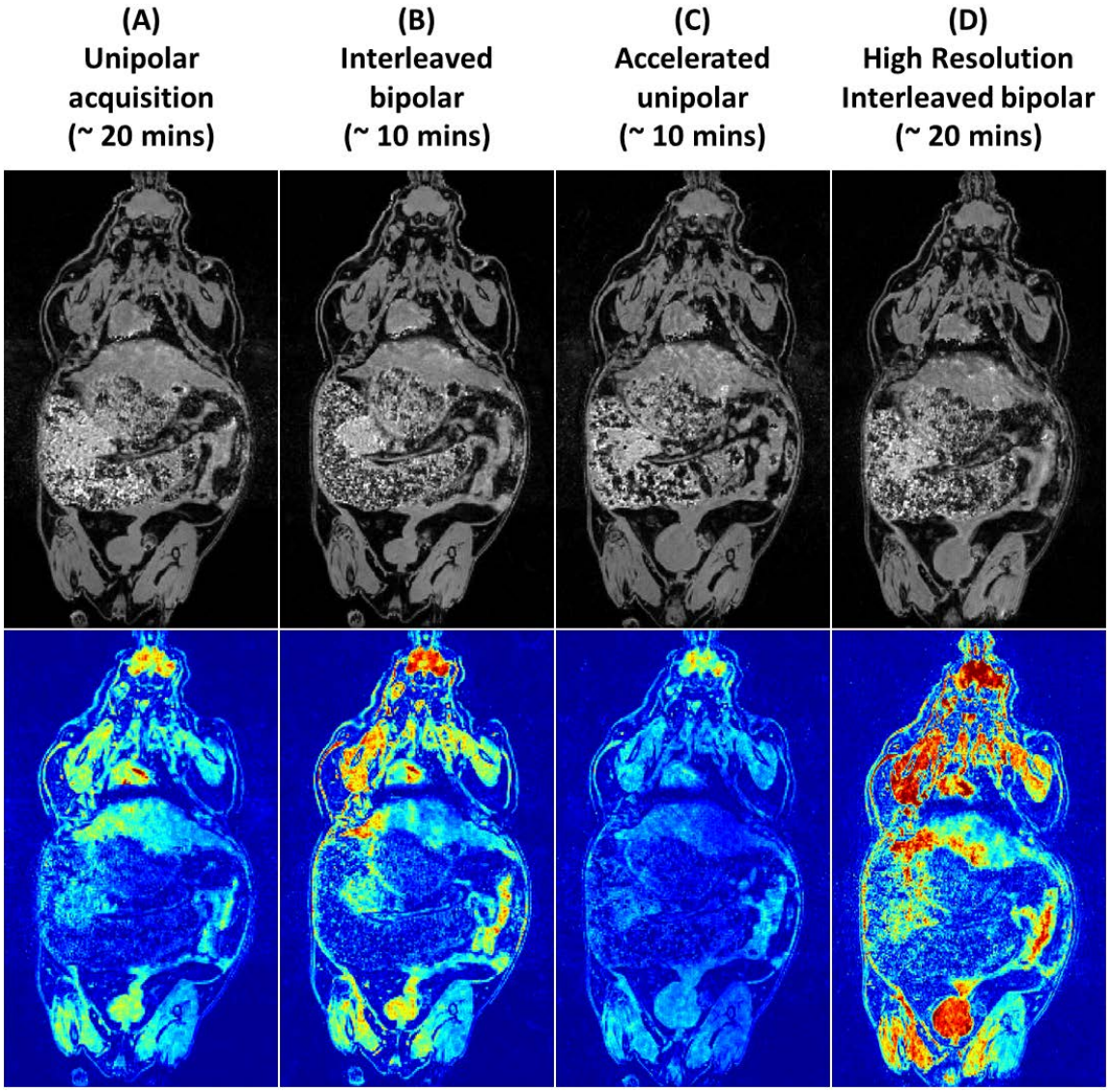

Figure 5.1: The water component (upper row) and its corresponding SNR efficiency map (lower row) from the four sequences. The interleaved bipolar sequences (B and D) demonstrate higher SNR efficiency compared to the corresponding unipolar sequences (A and C)

المنارة للاستشارات
www.manaraa.com

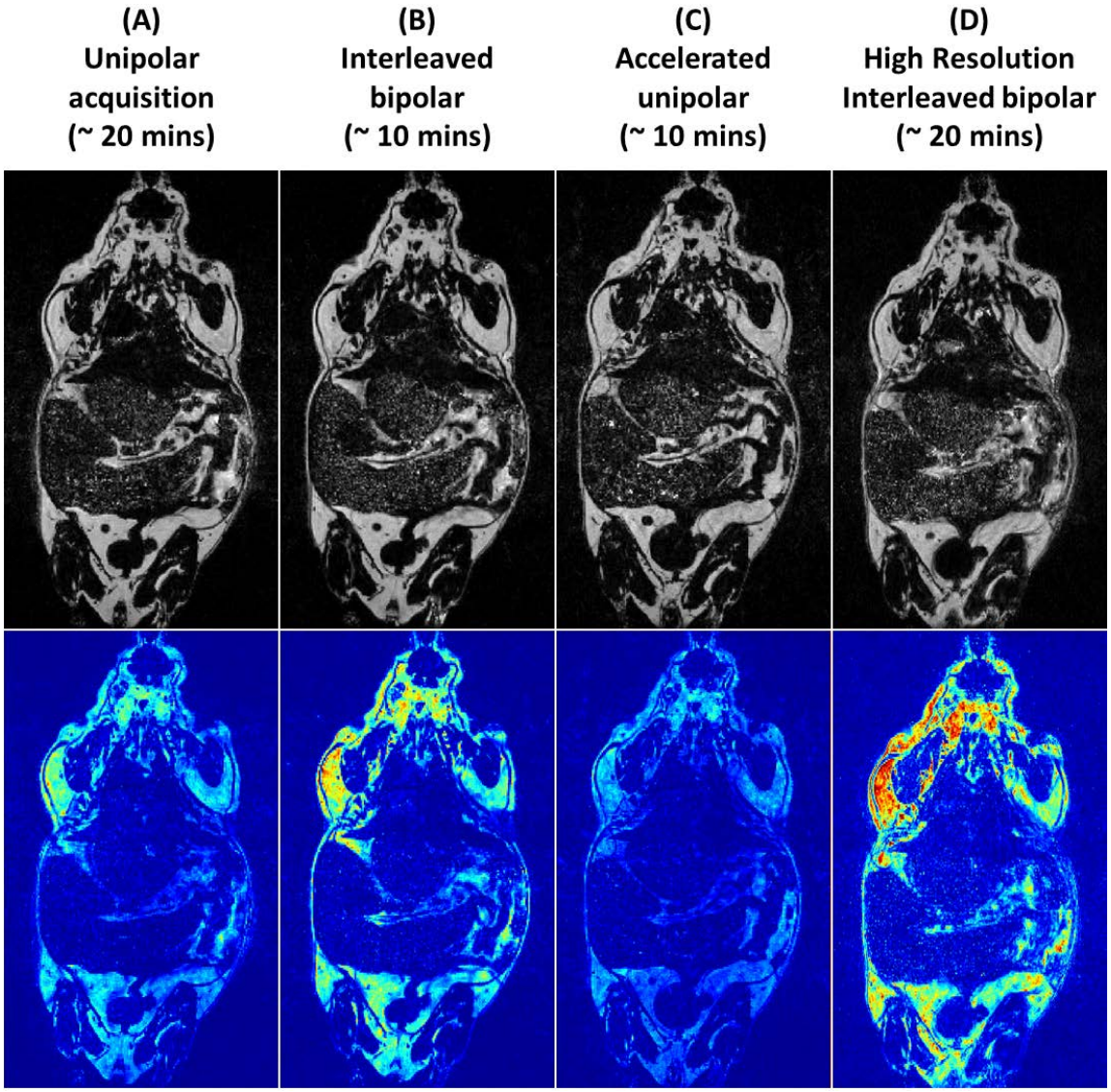

Figure 5.2: The fat component (upper row) and its corresponding SNR efficiency map (lower row) from the four sequences. The interleaved bipolar sequences (B and D) demonstrate higher SNR efficiency compared to the corresponding unipolar sequences (A and C)

المنارة للاستشارات
www.manaraa.com

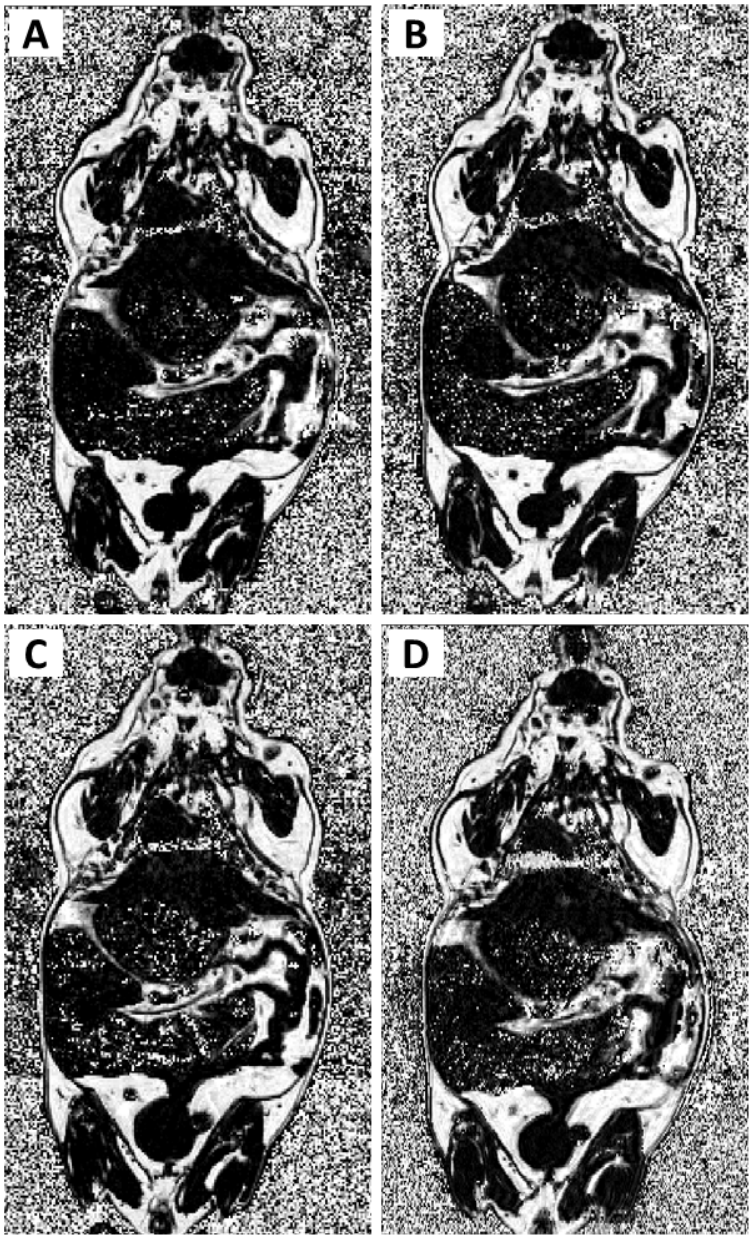

Figure 5.3: The fat fraction images from the four sequences. (A) Unipolar, (B) Interleaved bipolar, (C) Accelerated unipolar, (D) High resolution interleaved bipolar. Accurate fat fraction was obtained with the interleaved bipolar sequences compared to their corresponding unipolar sequences.

المنارة للاستشارات
www.manaraa.com

Figure 5.4 demonstrates the ability of the high resolution interleaved bipolar sequence (D) to clearly depict adipose tissue structures that cannot be identified using the unipolar sequence (A), without further increase in the acquisition time. Subcutaneous and intra-abdominal adipose tissue structures can be identified using the interleaved bipolar sequence (D), while partial volume effects prevent the clear depiction of the same structures in the unipolar sequence (A).

المنارة للاستشارات
www.manaraa.com

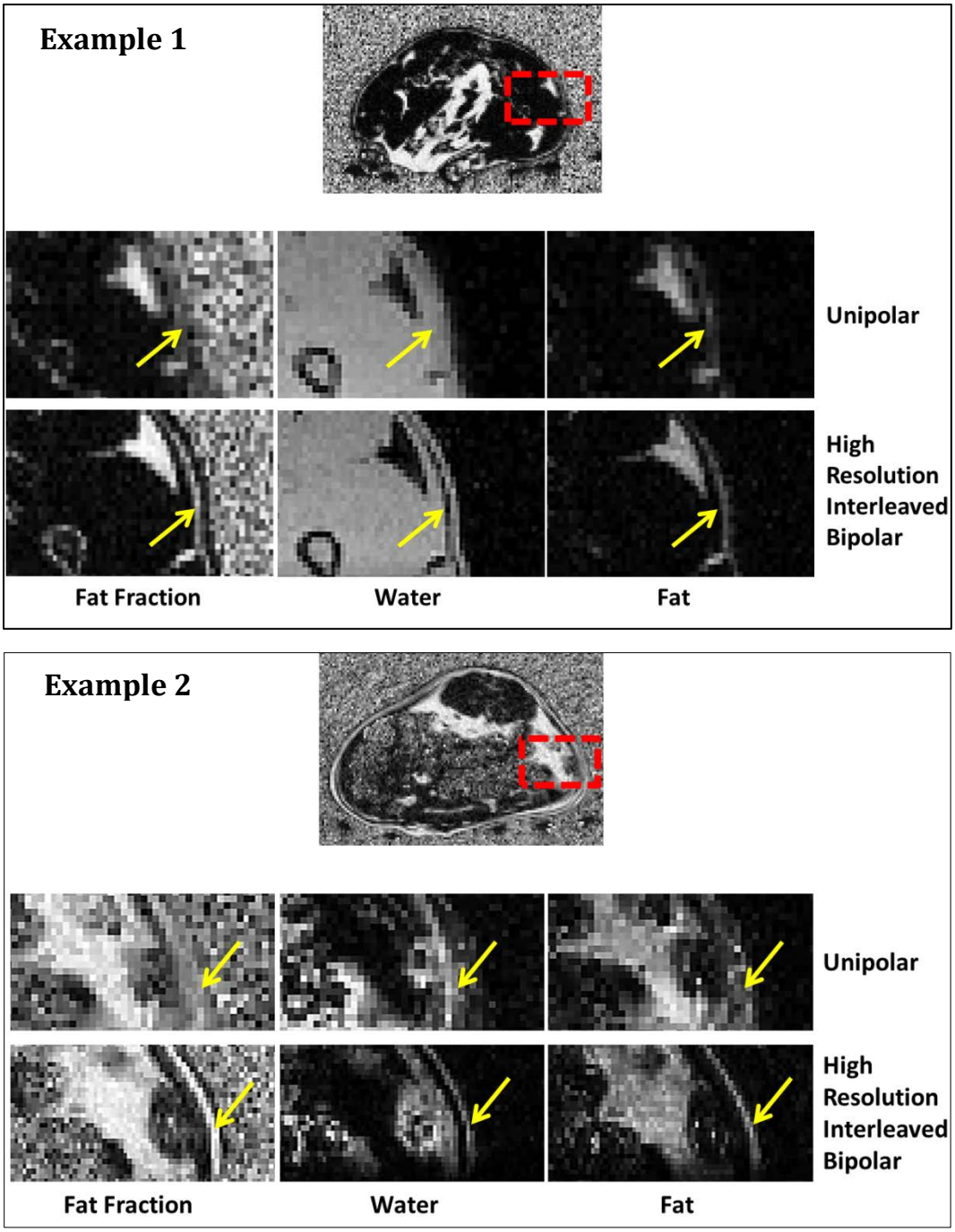

Figure 5.4: Fat fraction, water and fat images from 2 different slices are shown. For each example, the top image is an axial reformat of a fat fraction map from the unipolar sequence. A zoomed view of the region highlighted inside the red box is shown. The arrows indicate the anatomical structures that were clearly identified in the high resolution interleaved bipolar images, while they are not clearly depicted in the unipolar results.

المنارة للاستشارات
www.manaraa.com

5.4 Discussion

In this chapter we demonstrated the efficiency of the interleaved bipolar technique for in-vivo applications in animal models using 4 different sequence protocols:

Unipolar sequence (A) vs. interleaved bipolar sequence (B):
The bipolar acquisition scheme does not employ flyback gradients and hence optimal echo-spacing for a 6-echo acquisition was achieved in one TR (ETL = 6). This has significantly shortened the total acquisition time: ~10 mins using (B) compared to ~20 mins using (A), while providing accurate fat fraction maps. This suggested that the interleaved bipolar technique (B) is a more efficient alternative to the unipolar sequence (A).

Accelerated unipolar sequence (C) vs. interleaved bipolar sequence (B):
Remarkable SNR loss of both water and fat can be noticed using parallel imaging acceleration in (C) compared (B), confirming that the interleaved bipolar is a better option for faster acquisition.

Unipolar sequence (A) vs. high resolution bipolar sequence (D):
The resolution was doubled using the interleaved bipolar sequence within the same scan time as the unipolar sequence. Accurate fat fraction and higher SNR efficiency were also achieved.

Taking the unipolar sequence (A) as a baseline for our comparisons, there are several ways to benefit from the short acquisition time of the interleaved bipolar scheme. One straightforward way is to double the number of excitations (NEX) to enhance the SNR. A second alternative is to double the number of echoes, which can potentially enhance the noise performance of the resultant species. Here we chose to double the spatial resolution by increasing the number of phase and slice encodes. For comparisons, however, the frequency resolution was not altered in order to preserve similar echo-spacing as the unipolar sequence (A) and therefore similar noise performance [30-33]. For a single-shot acquisition, higher spatial resolution in the frequency-encode direction will result in larger echo-spacing in

المنارة للاستشارات
www.manaraa.com

sequence (D) and hence degraded image quality [30-33]. On the other hand, multiple shots in (D) can achieve better echo-spacing (and hence better noise performance) than its corresponding in (A). In practice it is possible to acquire the interleaved bipolar sequence on multiple shots, which will enhance the noise performance (better echo-spacing) but will increase the total acquisition time.

We noticed in some cases that there is a more significant SNR loss around the diaphragm in the interleaved bipolar (B) than its corresponding unipolar sequence (A). We also found more significant breathing motion artifacts in 2 out of 4 animals in the interleaved bipolar (B) than unipolar (A). We concluded that the interleaved bipolar technique is potentially more sensitive to motion artifacts, as it acquires two k-space centres (with positive and negative readout gradients) at two different time frames. The resultant complex-added images therefore might exhibit significant motion artifacts. For respiratory motion particularly, this problem can be easily addressed by using respiratory-gated imaging. Furthermore, in human applications, abdominal and thoracic water/fat imaging is often combined with either respiratory-gating or performed during breath-holds, which will prevent possible breathing motion. The interleaved bipolar might be, however, more sensitive to other non-gated/unexpected sources of motions (e.g. physical motion of patient). However, faster acquisitions (~ half scan time) are always achieved with the interleaved bipolar sequence compared to the unipolar one. Hence it is a trade-off between the acquisition speed and the potential reduction of motion artifacts.

المنارة للاستشارات
www.manaraa.com

5.5 Conclusion

In this work, we demonstrated that the interleaved bipolar sequence is more efficient than its counterpart unipolar sequence for *in-vivo* applications. An imaging protocol previously used for guinea pig fat quantification [27] was adopted and used as the baseline of the comparisons. The interleaved bipolar technique produced accurate fat fraction map in half the acquisition time of the unipolar and achieved double the resolution of the unipolar sequence within the same scan time. Higher SNR efficiency with accurate fat fraction maps were achieved in all experiments, suggesting that the interleaved bipolar is a better alternative for *in-vivo* applications than the current unipolar sequence employed in clinical practice.

المنارة للاستشارات
www.manaraa.com

References

[1] Kuk, J. L., Katzmarzyk, P. T., Nichaman, M. Z., Church, T. S., Blair, S. N., and Ross, R., "Visceral Fat Is an Independent Predictor of All-cause Mortality in Men," *Obesity,* vol. 14, pp. 336-341, 2006.

[2] Börnert, P., Keupp, J., Eggers, H., and Aldefeld, B., "Whole-body 3D water/fat resolved continuously moving table imaging," *Journal of Magnetic Resonance Imaging,* vol. 25, pp. 660-665, 2007.

[3] Bornert, P., Koken, P., Nehrke, K., Eggers, H., and Ostendorf, P., "Water/fat-resolved whole-heart Dixon coronary MRA: An initial comparison," *Magnetic Resonance in Medicine,* pp. n/a-n/a, 2013.

[4] Bornert, P. N. K. E. H. and Koken, P., "Whole-Heart Water/Fat resolved Spiral Imaging for Coronary MRA and Fatty Myocardial Infiltrations," in *Proceedings of the 18th Annual Meeting of ISMRM, Stockholm, Sweden*, 2010.

[5] Deng, J., Fishbein, M., Rigsby, C., Zhang, G., Schoeneman, S., and Donaldson, J., "Quantitative MRI for hepatic fat fraction and T2* measurement in pediatric patients with non-alcoholic fatty liver disease," *Pediatric Radiology,* pp. 1-9, 2014.

[6] Karampinos, D. C. Y. H. S. A. L. T. M. and S. Majumdar, S., "Quantification of susceptibility-induced fat resonance shift on chemical shift-based water/fat separation of skeletal muscle," in *Proceedings of the 19th Annual Meeting of ISMRM, Montreal, Canada*, 2011.

[7] Kellman, P., Hernando, D., and Arai, A. E., "Myocardial Fat Imaging," *Current Cardiovascular Imaging Reports,* vol. 3, pp. 83-91, 2010.

[8] Reeder, S. B., Cruite, I., Hamilton, G., and Sirlin, C. B., "Quantitative assessment of liver fat with magnetic resonance imaging and spectroscopy," *Journal of Magnetic Resonance Imaging,* vol. 34, pp. 729-749, 2011.

المنارة للاستشارات
www.manaraa.com

[9] Triplett, W. T., Baligand, C., Forbes, S. C., Willcocks, R. J., Lott, D. J., DeVos, S.*, et al.*, "Chemical shift-based MRI to measure fat fractions in dystrophic skeletal muscle," *Magnetic Resonance in Medicine,* vol. 72, pp. 8-19, 2014.

[10] Gold, G. E., Reeder, S. B., Yu, H. Brittain, J. H., Hargreaves, B. A., "Multi-Echo IDEAL Water-Fat Separation for Rapid Imaging of Cartilage," in *Proceedings of the 14th Annual Meeting of ISMRM, Seattle, WA, USA*, 2006.

[11] Hines, C. D. G., Frydrychowicz, A., Hamilton, G., Tudorascu, D. L., Vigen, K. K., Yu, H.*, et al.*, "T1 independent, T2* corrected chemical shift based fat--water separation with multi-peak fat spectral modeling is an accurate and precise measure of hepatic steatosis," *Journal of Magnetic Resonance Imaging,* vol. 33, pp. 873-881, 2011.

[12] Reeder, S. B., Markl, M., Yu, H., Hellinger, J. C., Herfkens, R. J., and Pelc, N. J., "Cardiac CINE imaging with IDEAL water-fat separation and steady-state free precession," *Journal of Magnetic Resonance Imaging,* vol. 22, pp. 44-52, 2005.

[13] Berglund, J., Johansson, L., Ahlstrom, H., and Kullberg, J., "Three-point dixon method enables whole-body water and fat imaging of obese subjects," *Magnetic Resonance in Medicine,* vol. 63, pp. 1659-1668, 2010.

[14] Addeman, B. T., Kutty, S., Perkins, T. G., Soliman, A. S., Wiens, C. N., McCurdy, C. M.*, et al.*, "Validation of volumetric and single-slice MRI adipose analysis using a novel fully automated segmentation method," *Journal of Magnetic Resonance Imaging,* 2014. DOI:10.1002/jmri.24526.

[15] Fernandez, M. L. and Volek, J. S., "Guinea pigs: a suitable animal model to study lipoprotein metabolism, atherosclerosis and inflammation," *Nutr Metab (Lond),* vol. 3, p. 17, 2006.

[16] Karimi, I., "Animal models as tools for translational research: focus on atherosclerosis, metabolic syndrome and type-II diabetes mellitus," *Lipoproteins—role in health and diseases. InTech. doi,* vol. 10, p. 47769, 2012.

المنارة للاستشارات
www.manaraa.com

[17] Fernandez, M. L., "Guinea pigs as models for cholesterol and lipoprotein metabolism," *The Journal of nutrition,* vol. 131, pp. 10-20, 2001.

[18] Lin, E., Fernandez, M. L., Tosca, M. A., and McNamara, D. J., "Regulation of hepatic LDL metabolism in the guinea pig by dietary fat and cholesterol," *Journal of lipid research,* vol. 35, pp. 446-457, 1994.

[19] Fernandez, M. L., Roy, S., and Vergara-Jimenez, M., "Resistant starch and cholestyramine have distinct effects on hepatic cholesterol metabolism in guinea pigs fed a hypercholesterolemic diet," *Nutrition research,* vol. 20, pp. 837-849, 2000.

[20] Leite, J. O., DeOgburn, R., Ratliff, J., Su, R., Smyth, J. A., Volek, J. S.*, et al.*, "Low-carbohydrate diets reduce lipid accumulation and arterial inflammation in guinea pigs fed a high-cholesterol diet," *Atherosclerosis,* vol. 209, pp. 442-448, 2010.

[21] Fernandez, M. L., Yount, N. Y., and McNamara, D. J., "Whole body and hepatic cholesterol synthesis rates in the guinea-pig: effect of dietary fat quality," *Biochimica et Biophysica Acta (BBA)-Lipids and Lipid Metabolism,* vol. 1044, pp. 340-348, 1990.

[22] Castañeda-Gutiérrez, E., Pouteau, E., Pescia, G., Moulin, J., Aprikian, O., and Macé, K., "The guinea pig as a model for metabolic programming of adiposity," *The American journal of clinical nutrition,* vol. 94, pp. 1838S-1845S, 2011.

[23] Hines, C. D., Agni, R., Roen, C., Rowland, I., Hernando, D., Bultman, E.*, et al.*, "Validation of MRI biomarkers of hepatic steatosis in the presence of iron overload in the ob/ob mouse," *Journal of Magnetic Resonance Imaging,* vol. 35, pp. 844-851, 2012.

المنارة للاستشارات
www.manaraa.com

[24] Hines, C. D., Yu, H., Shimakawa, A., McKenzie, C. A., Warner, T. F., Brittain, J. H., *et al.*, "Quantification of hepatic steatosis with 3-T MR imaging: validation in ob/ob mice," *Radiology,* vol. 254, pp. 119-128, 2009.

[25] Hu, H. H., Smith, D. L., Nayak, K. S., Goran, M. I., and Nagy, T. R., "Identification of brown adipose tissue in mice with fat–water IDEAL-MRI," *Journal of Magnetic Resonance Imaging,* vol. 31, pp. 1195-1202, 2010.

[26] Peng, X.-G., Ju, S., Qin, Y., Fang, F., Cui, X., Liu, G., *et al.*, "Quantification of liver fat in mice: comparing dual-echo Dixon imaging, chemical shift imaging, and 1H-MR spectroscopy," *Journal of lipid research,* vol. 52, pp. 1847-1855, 2011.

[27] Sinclair, K. J., Friesen-Waldner, L. J., McCurdy, C. M., Wiens, C. N., Wade, T. P., de Vrijer, B., *et al.*, "Quantification of total adipose tissue in fetal guinea pigs subjected to suboptimal in utero conditions using water-fat MR," in *In Proceedings of the 22nd Annual Meeting of ISMRM*, Milan, Italy, 2014, p. 3031.

[28] Wu, E. X., Tang, H., Tong, C., Heymsfield, S. B., and Vasselli, J. R., "In vivo MRI quantification of individual muscle and organ volumes for assessment of anabolic steroid growth effects," *Steroids,* vol. 73, pp. 430-440, 2008.

[29] Yu, H., Shimakawa, A., McKenzie, C. A., Brodsky, E., Brittain, J. H., and Reeder, S. B., "Multiecho water-fat separation and simultaneous R2* estimation with multifrequency fat spectrum modeling," *Magnetic Resonance in Medicine,* vol. 60, pp. 1122-1134, 2008.

[30] Hernando, D., Hines, C. D. G., Yu, H., and Reeder, S. B., "Addressing phase errors in fat-water imaging using a mixed magnitude/complex fitting method," *Magnetic Resonance in Medicine,* vol. 67, pp. 638–644-638–644, 2012.

[31] Pineda, A. R., Reeder, S. B., Wen, Z., and Pelc, N. J., "Cramer--Rao bounds for three-point decomposition of water and fat," *Magnetic resonance in medicine,* vol. 54, pp. 625-635, 2005.

المنارة للاستشارات
www.manaraa.com

[32] Yu, H., Shimakawa, A., Hines, C. D., McKenzie, C. A., Hamilton, G., Sirlin, C. B., *et al.*, "Combination of complex-based and magnitude-based multiecho water-fat separation for accurate quantification of fat-fraction," *Magnetic resonance in medicine,* vol. 66, pp. 199-199, 2011.

[33] Chebrolu, V. V., Yu, H., Pineda, A. R., McKenzie, C. A., Brittain, J. H., and Reeder, S. B., "Noise analysis for 3-point chemical shift-based water-fat separation with spectral modeling of fat," *J Magn Reson Imaging,* vol. 32, pp. 493-500, 2010.

[34] Kellman, P. and McVeigh, E. R., "Image reconstruction in SNR units: A general method for SNR measurement†," *Magnetic resonance in medicine,* vol. 54, pp. 1439-1447, 2005.

[35] Wiens, C. N., Kisch, S. J., Willig-Onwuachi, J. D., and McKenzie, C. A., "Computationally rapid method of estimating signal-to-noise ratio for phased array image reconstructions," *Magn Reson Med,* vol. 66, pp. 1192-1197, 2011.

[36] Pruessmann, K. P., Weiger, M., Börnert, P., and Boesiger, P., "Advances in sensitivity encoding with arbitrary k-space trajectories," *Magn Reson Med,* vol. 46, pp. 638-651, 2001.

[37] Soliman, A. S., Yuan, J., Vigen, K. K., White, J. A., Peters, T. M., and McKenzie, C. A., "Max-IDEAL: A max-flow based approach for IDEAL water/fat separation," *Magnetic Resonance in Medicine,* vol. 72, pp. 510-521, 2014.

[38] Soliman, A. S., Yuan, J., White, J. A., Peters, T. M., and McKenzie, C. A., "A Convex Relaxation Approach to Fat/Water Separation with Minimum Label Description," in *Lecture Notes in Computer Science*, N. Ayache, H. Delingette, P. Golland, and K. Mori, Eds., ed: Springer Berlin Heidelberg, 2012, pp. 519-526.

المنارة للاستشارات
www.manaraa.com

[39] Reeder, S. B., Hu, H. H., and Sirlin, C. B., "Proton density fat-fraction: A standardized mr-based biomarker of tissue fat concentration," *Journal of Magnetic Resonance Imaging,* vol. 36, pp. 1011-1014, 2012.

[40] Yu, H., McKenzie, C. A., Shimakawa, A., Vu, A. T., Brau, A., Beatty, P. J.*, et al.*, "Multiecho reconstruction for simultaneous water-fat decomposition and T2* estimation," *J Magn Reson Imaging,* vol. 26, pp. 1153-1161, 2007.

المنارة للاستشارات

www.manaraa.com

"Science is a wonderful thing if one does not have to earn one's living at it"
- Einstein

Chapter 6

Conclusion and Future Work

6.1 Summary

Clinical and scientific interest in fat quantification using MRI has grown remarkably in the last decade. Quantifying the tissue fat concentration is important for several diseases in various organs including liver [1], heart [2], skeletal muscle [3, 4] and kidney [5] as well as quantifying white and brown adipose tissue [6, 7]. The growing of clinical need for fat quantification is accompanied by the need to establish accurate biomarkers for quantification [8]. Proton Density Fat Fraction (PDFF) is currently, by consensus, the most appropriate and practical MR-based biomarker for measuring tissue fat concentration [8]. It is the ratio of density of mobile protons from fat to the total density of mobile protons from both fat and water. PDFF can be generated by either spectroscopy (MRS)-based or imaging-based methods. Both techniques rely on the chemical-shift between water and fat. However, MRS-based methods generate single-voxel measurements, while imaging-based methods are capable of producing fat concentration maps for the entire organ(s) under

المنارة للاستشارات
www.manaraa.com

examination. Chemical-shift encoded imaging acquires several images at different echo-times where water and fat exhibit different phase shifts [9]. Post-processing techniques are then applied to separate both water and fat components. PDFF is consequently calculated by dividing the ratio of the fat signal by the total signal from both species, obtaining fat fraction map. In order to obtain an accurate PDFF map, several confounding factors must be considered, such as the magnetic field inhomogeneities [10], T_1^*-related bias [11], T_2^* decay [12] and the complex frequency spectrum of fat [13], noise-related bias [11] and eddy currents [14, 15]. Once all the factors are considered, the PDFF will reflect the underlying fat concentration, which is a characteristic property of the tissue. While several techniques were proposed to address the confounding factors, there is extensive ongoing research to improve the precision and the reproducibility of the PDFF measurements for clinical use.

In this dissertation we proposed new acquisition and reconstruction techniques to address several challenges to accurate MRI fat quantification. Chapter 2 and 3 proposed new reconstruction techniques, while Chapter 4 and 5 demonstrated a new acquisition scheme with its *in-vivo* applications.

6.1.1 A Convex Relaxation Approach to Water/Fat Separation with Minimum Label Description (Chapter 2)

In Chapter 2 a novel technique to estimate magnetic field inhomogeneities is proposed [16]. Resolving the local frequency variations in the main magnetic field represents the main obstacle for water/fat separation process. Previous work relied on spatial smoothness constraints; while the presented method employed a multi-labeling model to resolve the ambiguity of the estimation. The field map is generated using a convex-relaxed multi-labeling model, where each label represents a frequency offset. To reduce the vulnerability of converging to local minima an additional cost is added to penalize the number of employed labels. This will enforce fewer labels to be used in the minimization process, and hence improves the

المنارة للاستشارات
www.manaraa.com

performance of the field map estimate. The estimate is subsequently refined using an iterative gradient-descent based IDEAL process. The signal model incorporates the complex multi-peak fat spectrum. Experiments were performed using low flip angle to minimize the T_1-related bias. T_2^* was not considered in this model. In-vivo experiments were performed on cardiac and abdominal datasets demonstrating correct water/fat separation. The results were compared against the widely-used region-growing method and have demonstrated significantly better performance in cases of abrupt changes in the magnetic field.

6.1.2 Max-IDEAL: A Max-Flow Based Approach to IDEAL Water/Fat Separation (Chapter 3)

In Chapter 3 the convex relaxation method employed in Chapter 2 is optimized to improve the robustness of the water/fat estimation [17]. A new inclusive approach was employed to integrate the T2* decay in the estimation process, where few T_2^* values are summed up at each label during the labeling process. The resultant field map estimate becomes therefore more representative of the signal model and more robust to local minima. In addition, an adaptive spatial filtering was introduced after the labeling procedure to enhance the performance of the method. A continuous max-flow approach was employed to address the labeling model, while T2*-IDEAL is applied in the second stage; the technique is therefore called Max-IDEAL. Data provided by the ISMRM challenge 2012 on water/fat separation were used to demonstrate the robustness of the technique. The accuracy of water/fat separation was calculated by taking the ratio of voxels with correct separation to the total number of voxels (excluding background noise). Max-IDEAL scored 98.44% success rates from all processed cases. Comparisons against recent robust techniques such as the graph-cut and FLAME methods were also performed on *in-vivo* data, demonstrating successful water/fat separation while the other methods failed.

المنارة للاستشارات
www.manaraa.com

6.1.3 Fat Quantification Using an Interleaved Bipolar Acquisition (Chapter 4)

In Chapter 4 we propose a novel acquisition scheme for fat quantification using bipolar readout gradients. The proposed bipolar sequence is more efficient than the current unipolar sequence currently employed in clinical practice. A multi-echo bipolar acquisition is employed such that the even echoes have opposite polarity to the odd echoes. The readout gradients alternate their polarities every other phase-encode line. Each echo, therefore, consists of phase-encode lines with both positive and negative polarities. Phase-encodes acquired with the same polarity are grouped together, and parallel imaging reconstruction is used to obtain two full k-space maps with opposite readout polarities at all the echoes. By complex averaging, the inconsistent phase errors between odd and even echoes are removed and water/fat separation techniques employed with conventional unipolar sequences can be performed. The acquisition and reconstruction pipeline overcomes the bipolar artefacts known to corrupt the water/fat separation procedure. Phantoms and in-vivo experiments demonstrated accurate fat fraction and increased SNR efficiency compared to the established unipolar acquisition. Phase and magnitude artefacts from the bipolar acquisition were eliminated in all experiments.

6.1.4 An Efficient Chemical-shift Encoded Acquisition for *in-vivo* Applications (Chapter 5)

In Chapter 5 we demonstrated the efficiency of the interleaved bipolar sequence proposed in the previous chapter over the conventional unipolar acquisition in animal experiments. Chemical-shift encoded water/fat imaging is utilized in the animal model to visualize the fat distribution as well as to quantify the fat concentration. Fat and water images with high spatial resolution are required. Four guinea pigs were scanned using the unipolar and the interleaved bipolar acquisitions. A unipolar imaging protocol previously used for guinea pig fat

المنارة للاستشارات
www.manaraa.com

quantification was adopted and used as the baseline of the comparisons. The interleaved bipolar acquisition produced accurate fat fraction maps in half the acquisition time of its corresponding unipolar sequences (~10 mins vs. ~20 mins, respectively). Similar TE1 and echo-spacing were preserved to achieve similar noise performance in all comparisons. Using the interleaved bipolar sequence, the spatial resolution was doubled while keeping the same acquisition time as the standard unipolar sequence. Higher SNR efficiency with accurate fat fraction maps were achieved in all the interleaved bipolar compared to the unipolar sequences, suggesting that the interleaved bipolar is a better alternative for *in-vivo* applications than the current unipolar sequence employed in clinical practice.

6.2 Future Directions

6.2.1 Combining Multiple Smoothness Constraints To Improve The Robustness of The Field Map Estimation

In Chapter 2 and 3 we have presented two field map estimation techniques based on the multi-label Potts model, where each frequency offset is represented by a label in an initial estimate of the field map. The continuous max-flow algorithm minimizes the total perimeter of all labels [18]. As shown in chapter 3, this unique smoothness constraint was capable of resolving abrupt magnetic field inhomogeneities, while other techniques fail. However, Potts model does not impose any constraints on the spatial smoothness of the field map. From our experience on a wide variety of datasets including phantoms, animals (e.g. rats, mice and guinea pigs) as well as various human organs (abdomen, thorax, knee ankle and brain), both smoothness constraints might be needed. The graph-cut method [19] and its variant proposed by Berglund *et al.* [20] are two typical examples of robust spatial-smoothness-based techniques, while Max-IDEAL is the first technique that demonstrated the usage of total perimeter smoothness.

المنارة للاستشارات
www.manaraa.com

Techniques that solely rely on spatial smoothness might fail to resolve the ambiguity of abrupt magnetic field variations. On the other hand, total perimeter smoothness employed in the Max-IDEAL might fail to estimate the gradual change of magnetic inhomogeneities as no spatial constraints are assumed. The Adaptive Spatial Filter (ASF), described in Chapter 3, incorporates spatial information into Max-IDEAL before the labeling stage. However, it only uses morphological image processing operations which might not be sufficient when sophisticated variations in the magnetic field occur.

It is feasible to integrate the total perimeter smoothness constraint of Max-IDEAL with the spatial smoothness of graph-cut-based methods in the cost function to be minimized. Weighting these 2 different smoothness constraints, however, will play an important role in the robustness of the resultant technique. Fortuitously, the energy minimization stage employed in both graph-cut-based methods and the Max-IDEAL are based on the max-flow/min-cut theory. Therefore, we think it is feasible to derive a combined optimization approach that combines the 2 smoothness terms of the 2 approaches. However, Max-IDEAL uses the continuous max-flow algorithm that is easily parallelized/accelerated on general-purpose graphics processing units (GPGPU), while the graph-cut algorithm cannot be efficiently parallelized. It is worth noting that Max-IDEAL employs a multi-label approach that can be significantly slower than binary labeling used in graph-cut-based methods, in case parallel computation hardware (GPGPU) is not used. Nevertheless, employing GPGPU renders the Max-IDEAL a faster field map estimation approach than its corresponding graph-cut method.

The spatial smoothness used in Berglund *et al.* [20] considers the periodicity of the cost function, while Hernando's graph-cut method does not consider it. Max-IDEAL, on the other hand, is not influenced by the periodicity of the cost function as shown in Chapter 3. It is important to consider this periodicity phenomenon when spatial smoothness is employed, particularly for the cases where severe abrupt changes exist in magnetic field [17].

المنارة للاستشارات
www.manaraa.com

6.2.2 Integrating Prior Knowledge of Anatomy into Max-IDEAL

One of the main challenges for any field map estimation algorithm is that it is required to be robust over a wide variety of applications and anatomies. The level of inhomogeneities in cardiac imaging, for example, can be more challenging than some skeletal muscle applications as knee imaging, due to the presence of air/tissue interfaces in the thorax. Few techniques benefit from the knowledge of the underlying anatomy in order to enhance the performance of the estimation. Inspired from recent techniques, we hypothesized that two anatomy-oriented concepts can be combined with the Max-IDEAL: 1) the Fat Likelihood Analysis for Multi-echo Signals (FLAME) [21] and 2) the prior estimation of susceptibility-induced field map [22].

FLAME [21] introduced an interesting perspective to "highlight" the locations of fat by generating a fat likelihood map of the underlying anatomy. Water-dominant pixels will have lower likelihood value while fat-dominant pixels will possess higher values. The map is produced by exploiting the spectral differences between water and fat using single-peak and multi-peak fat spectrum. The residuals of a cost function, R, are calculated at certain pixel using single-peak (sp) and multi-peak (mp) models, and then a fat likelihood map [21] is generated as follows:

$$Fat\ Likelihood\ map = \frac{R_{sp} - R_{mp}}{\max\left(R_{sp} - R_{mp}\right)}$$

This map can be incorporated into Max-IDEAL as a weighing function to highlight the type of species at each pixel. However, this map can guide the field map estimation only at locations of low (<20%) or high (>80%) fat fractions, while its values will be undefined for locations with considerable mixtures of water and fat.

Another approach has been recently proposed by Sharma *et al.* [22] where a susceptibility map is estimated first before performing the water/fat separation. This method assumes that the field map is mainly caused by two factors: 1) the background shimming and magnet imperfections, 2) the susceptibility differences

المنارة للاستشارات
www.manaraa.com

between air and various types of tissues. Therefore they estimate the magnetic field variations caused by the susceptibility difference first then use it to demodulate the source images. Any water/fat separation technique can be subsequently performed using the demodulated source images, to estimate the final field map. Although this method can be applied prior to any field map estimation technique, however Max-IDEAL has the advantage of employing a non-spatial smoothness constraint which therefore will overcome erroneous estimation occurred from the spatial distribution of the susceptibility map.

6.2.3 A Standardized Accuracy Metric of Field Map

A standard measure of the field map accuracy does not exist. Visual inspection of water/fat swaps is the only approximate method to evaluate the accuracy of any estimate. An attempt to develop an image-based metric for field map was introduced by Smith *et al*. [23] in the first phase of ISMRM challenge 2012 for water/fat separation. However, they concluded that their metric-based strategy cannot be reliably used to select the best resultant field map, and this strategy was abandoned. First, a straightforward benefit of a standard metric is to automatically detect any potential water/fat swaps in the output. Although a 'swaps-free' result is desired, water/fat swaps located outside the area of interest will also be acceptable. Hence, the metric can be anatomy-specific, where the evaluation is only performed at the region of interest. Second, the effect of the exact field map values on the accuracy of the quantification is still unknown. One might find two techniques that generate 'swaps-free' field maps, while the exact values of the maps do not match. The reason is that water/fat swaps can be avoided once the estimated local frequency is within 3.5 ppm of the correct value, but the accurate value might not be achieved yet [10, 24].

المنارة للاستشارات
www.manaraa.com

6.2.4 Reduce The Vulnerability of the Interleaved Bipolar Sequence to Motion Artifacts

Motion artefacts can interrupt any acquisition, whether unipolar or interleaved bipolar, particularly if it occurs during the acquisition of the k-space centre. However, the interleaved bipolar requires the acquisition of 2 k-space centres, with the second centre acquired at the end of the scan. If motion occurred at one of the 2 centres, the motion artefacts will distort the contrast of the corresponding dataset (positive or negative), leading to more significant artefacts in the final result than its corresponding unipolar acquisition. This makes the interleaved bipolar acquisition more vulnerable to motion, particularly in breath-hold acquisitions if, for example, the patient breathed in the last few seconds. Respiratory, cardiac and the physical motion of patient are all potential sources of motion artefacts. One approach is to use cardiac- or respiratory- gating, which is frequently employed during abdominal/thoracic scans. In fact, the interleaved bipolar has the advantage of being more efficient than the unipolar in gated acquisitions, given its short acquisition time (~ half) compared to the conventional unipolar. Another approach to reduce the vulnerability to motion is to acquire the second k-space centre directly following the first one, or employ a centre-out acquisition strategy, where both centres are acquired at the beginning followed by the high frequency fraction of the k-space.

6.2.5 Calibration-less Interleaved Bipolar Acquisition

One of the limitations of the interleaved bipolar sequence is that it requires 2 acquisitions of the k-space centre. The main purpose of the second acquisition of the centre is to use as a calibration set for parallel imaging reconstruction. Compared to conventional bipolar sequence, the additional acquisition of k-space centre prolongs the acquisition time and hence reduces the expected SNR efficiency. Calibration data-free parallel imaging reconstruction has been recently proposed by Shin *et al.* [25], where the reconstruction does not require a separate calibration step to

المنارة للاستشارات
www.manaraa.com

estimate coil sensitivity information. The multi-channel coils are structured into a single data matrix and then single value decomposition (SVD) analysis is performed in an iterative algorithm to decompose the signal from the noise subspaces. Employing this technique in the interleaved bipolar reconstruction will have two advantages: 1) It will shorten the acquisition time as no calibration centres are required, 2) it will reduce the vulnerability to motion artefacts as discussed in 6.2.4. However, a main challenge here is to preserve the correct phase of the signal after the reconstruction to guarantee a complete cancellation of phase and magnitude errors; otherwise erroneous fat fraction measures will be produced [26, 27].

6.3 Conclusion

In this dissertation we presented a complete framework for fat quantification using MRI. We presented novel acquisition and reconstruction techniques for fat quantification with *in-vivo* applications in animals and various human organs. The proposed reconstruction techniques addressed the confounding factors that hinder accurate quantification of tissue fat concentration, while the proposed acquisition technique enhances the efficiency of the acquisition compared to the sequences that currently used in clinical practice.

المنارة للاستشارات
www.manaraa.com

References

[1] Reeder, S. B., Cruite, I., Hamilton, G., and Sirlin, C. B., "Quantitative assessment of liver fat with magnetic resonance imaging and spectroscopy," *Journal of Magnetic Resonance Imaging,* vol. 34, pp. 729-749, 2011.

[2] Reeder, S. B., Markl, M., Yu, H., Hellinger, J. C., Herfkens, R. J., and Pelc, N. J., "Cardiac CINE imaging with IDEAL water-fat separation and steady-state free precession," *Journal of Magnetic Resonance Imaging,* vol. 22, pp. 44-52, 2005.

[3] Chen, C. A., Lu, W., John, C. T., Hargreaves, B. A., Reeder, S. B., Delp, S. L.*, et al.*, "Multiecho IDEAL Gradient-Echo Water-Fat Separation for Rapid Assessment of Cartilage Volume at 1.5 T: Initial Experience 1," *Radiology,* vol. 252, pp. 561-567, 2009.

[4] Siepmann, D. B., McGovern, J., Brittain, J. H., and Reeder, S. B., "High-resolution 3D cartilage imaging with IDEAL–SPGR at 3 T," *American Journal of Roentgenology,* vol. 189, pp. 1510-1515, 2007.

[5] Israel, G. M., Hindman, N., Hecht, E., and Krinsky, G., "The use of opposed-phase chemical shift MRI in the diagnosis of renal angiomyolipomas," *American Journal of Roentgenology,* vol. 184, pp. 1868-1872, 2005.

[6] Hu, H. H., Smith, D. L., Nayak, K. S., Goran, M. I., and Nagy, T. R., "Identification of brown adipose tissue in mice with fat–water IDEAL-MRI," *Journal of Magnetic Resonance Imaging,* vol. 31, pp. 1195-1202, 2010.

[7] Hu, H. H., Yin, L., Aggabao, P. C., Perkins, T. G., Chia, J. M., and Gilsanz, V., "Comparison of brown and white adipose tissues in infants and children with chemical-shift-encoded water-fat MRI," *Journal of Magnetic Resonance Imaging,* 2013.

المنارة للاستشارات
www.manaraa.com

[8] Reeder, S. B., Hu, H. H., and Sirlin, C. B., "Proton density fat-fraction: A standardized mr-based biomarker of tissue fat concentration," *Journal of Magnetic Resonance Imaging,* vol. 36, pp. 1011-1014, 2012.

[9] Ma, J., "Dixon techniques for water and fat imaging," *Journal of Magnetic Resonance Imaging,* vol. 28, pp. 543-558, 2008.

[10] Reeder, S. B., Wen, Z., Yu, H., Pineda, A. R., Gold, G. E., Markl, M., *et al.*, "Multicoil Dixon chemical species separation with an iterative least-squares estimation method," *Magnetic Resonance in Medicine,* vol. 51, pp. 35-45, 2004.

[11] Liu, C. Y., McKenzie, C. A., Yu, H., Brittain, J. H., and Reeder, S. B., "Fat quantification with IDEAL gradient echo imaging: correction of bias from T1 and noise," *Magnetic Resonance in Medicine,* vol. 58, pp. 354-364, 2007.

[12] Yu, H., McKenzie, C. A., Shimakawa, A., Vu, A. T., Brau, A., Beatty, P. J., *et al.*, "Multiecho reconstruction for simultaneous water-fat decomposition and T2* estimation," *Journal of Magnetic Resonance Imaging,* vol. 26, pp. 1153-1161, 2007.

[13] Yu, H., Shimakawa, A., McKenzie, C. A., Brodsky, E., Brittain, J. H., and Reeder, S. B., "Multiecho water-fat separation and simultaneous R 2* estimation with multifrequency fat spectrum modeling," *Magnetic Resonance in Medicine,* vol. 60, pp. 1122-1134, 2008.

[14] Yu, H., Shimakawa, A., Hines, C. D., McKenzie, C. A., Hamilton, G., Sirlin, C. B., *et al.*, "Combination of complex-based and magnitude-based multiecho water-fat separation for accurate quantification of fat-fraction," *Magnetic resonance in medicine,* vol. 66, pp. 199-199, 2011.

[15] Wade, T. P., Wiens, C. N., and McKenzie, C. A., "Eddy Current Compensated IDEAL," in *Proc. Intl. Soc. Mag. Reson. Med*, 2013, p. 549.

المنارة للاستشارات
www.manaraa.com

[16] Soliman, A. S., Yuan, J., White, J. A., Peters, T. M., and McKenzie, C. A., "A Convex Relaxation Approach to Fat/Water Separation with Minimum Label Description," *Medical Image Computing and Computer-Assisted Intervention – MICCAI,* pp. 519-526, 2012/01/01 2012.

[17] Soliman, A. S., Yuan, J., Vigen, K. K., White, J. A., Peters, T. M., and McKenzie, C. A., "Max-IDEAL: A max-flow based approach for IDEAL water/fat separation," *Magnetic Resonance in Medicine,* vol. 72, pp. 510-521, 2014.

[18] Yuan, J., Bae, E., Tai, X. C., and Boykov, Y., "A continuous max-flow approach to potts model," presented at the In Proceedings of the 11th European Conference on Computer Vision (ECCV), Crete, Greece, 2010.

[19] Hernando, D., Kellman, P., Haldar, J. P., and Liang, Z. P., "Robust water/fat separation in the presence of large field inhomogeneities using a graph cut algorithm," *Magnetic Resonance in Medicine,* vol. 63, pp. 79-90, 2010.

[20] Berglund, J. and Kullberg, J., "Three-dimensional water/fat separation and T2* estimation based on whole-image optimization - Application in breathhold liver imaging at 1.5 T," *Magnetic Resonance in Medicine,* vol. 67, pp. 1684-1693, 2012.

[21] Yu, H., Reeder, S. B., Shimakawa, A., McKenzie, C. A., and Brittain, J. H., "Robust multipoint water-fat separation using fat likelihood analysis," *Magnetic Resonance in Medicine,* vol. 67, pp. 1065-1076, 2012.

[22] Sharma, S. D., Artz, N. S., Hernando, D., Horng, D. E., and Reeder, S. B., "Improving chemical shift encoded water–fat separation using object-based information of the magnetic field inhomogeneity," *Magnetic Resonance in Medicine,* 2014. doi:10.1002/mrm.25163.

[23] Smith, D., Berglund, J., Kullberg, J., Ahlström, H., Avison, M., and Welch, E., "Optimization of Fat-Water Separation Algorithm Selection and Options Using Image-based Metrics with Validation by ISMRM Fat-Water Challenge

المنارة للاستشارات
www.manaraa.com

Datasets," in *In Proceedings of the 21st Annual Meeting of ISMRM*, Salt Lake City, UT, 2013, p. 2413.

[24] Glover, G. H. and Schneider, E., "Three-point dixon technique for true water/fat decomposition with B0 inhomogeneity correction," *Magnetic resonance in medicine,* vol. 18, pp. 371-383, 1991.

[25] Shin, P. J., Larson, P. E. Z., Ohliger, M. A., Elad, M., Pauly, J. M., Vigneron, D. B., *et al.*, "Calibrationless parallel imaging reconstruction based on structured low-rank matrix completion," *Magnetic Resonance in Medicine,* vol. 72, pp. 959-970, 2014.

[26] Yu, H., Shimakawa, A., McKenzie, C. A., Lu, W., Reeder, S. B., Hinks, R. S., *et al.*, "Phase and amplitude correction for multi-echo water--fat separation with bipolar acquisitions," *Journal of Magnetic Resonance Imaging,* vol. 31, pp. 1264-1271, 2010.

[27] Lu, W., Yu, H., Shimakawa, A., Alley, M., Reeder, S. B., and Hargreaves, B. A., "Water-fat separation with bipolar multiecho sequences," *Magnetic Resonance in Medicine,* vol. 60, pp. 198-209, 2008.

المنارة للاستشارات

www.manaraa.com

Ethics Approval

Research Western

Use of Human Participants - Ethics Approval Notice

Principal Investigator: Dr. Giles Santyr
Review Number: 10854E
Review Level: Delegated
Approved Local Adult Participants: 500
Approved Local Minor Participants: 0
Protocol Title: 3.0T MRI Software and RF Hardware Development
Department & Institution: Radiology, Robarts Research Institute
Sponsor:
Ethics Approval Date: January 27, 2011 **Expiry Date:** December 31, 2016
Documents Reviewed & Approved & Documents Received for Information:

Document Name	Comments	Version Date
Revised Study End Date	The new study end date is set to December 31, 2016 to allow for study completion.	
Change in Study Personnel	Cyndi Harper-Little is on leave and therefore the new contact is Trevor Szekeres.	

This is to notify you that The University of Western Ontario Research Ethics Board for Health Sciences Research Involving Human Subjects (HSREB) which is organized and operates according to the Tri-Council Policy Statement: Ethical Conduct of Research Involving Humans and the Health Canada/ICH Good Clinical Practice Practices: Consolidated Guidelines; and the applicable laws and regulations of Ontario has reviewed and granted approval to the above referenced revision(s) or amendment(s) on the approval date noted above. The membership of this REB also complies with the membership requirements for REB's as defined in Division 5 of the Food and Drug Regulations.

The ethics approval for this study shall remain valid until the expiry date noted above assuming timely and acceptable responses to the HSREB's periodic requests for surveillance and monitoring information. If you require an updated approval notice prior to that time you must request it using the UWO Updated Approval Request Form.

Members of the HSREB who are named as investigators in research studies, or declare a conflict of interest, do not participate in discussion related to, nor vote on, such studies when they are presented to the HSREB.

The Chair of the HSREB is Dr. Joseph Gilbert. The UWO HSREB is registered with the U.S. Department of Health & Human Services under the IRB registration number IRB 00000940.

[redacted]

Signature

Ethics Officer to Contact for Further Information

Janice Sutherland	Grace Kelly	Shantel Walcott
[redacted]	[redacted]	[redacted]

This is an official document. Please retain the original in your files.

The University *of* Western Ontario
Office of Research Ethics
Support Services Building Room 5150 • London, Ontario • CANADA – N6G 1G9
PH: 519-661-3036 • F: 519-850-2466 • ethics@uwo.ca • www.uwo.ca/research/ethics

المنارة للاستشارات
www.manaraa.com

Western

AUP Number: 2010-229
PI Name: Regnault, Timothy
AUP Title: In Utero Origins Of Adult Insulin Resistance
Approval Date: 09/08/2014

Official Notice of Animal Use Subcommittee (AUS) Approval: Your new Animal Use Protocol (AUP) entitled "In Utero Origins Of Adult Insulin Resistance" has been APPROVED by the Animal Use Subcommittee of the University Council on Animal Care. This approval, although valid for four years, and is subject to annual Protocol Renewal.2010-229::5

1. This AUP number must be indicated when ordering animals for this project.
2. Animals for other projects may not be ordered under this AUP number.
3. Purchases of animals other than through this system must be cleared through the ACVS office. Health certificates will be required.

The holder of this Animal Use Protocol is responsible to ensure that all associated safety components (biosafety, radiation safety, general laboratory safety) comply with institutional safety standards and have received all necessary approvals. Please consult directly with your institutional safety officers.

Submitted by: Copeman, Laura
on behalf of the Animal Use Subcommittee
University Council on Animal Care

[redacted]

The University *of* Western Ontario
Animal Use Subcommittee / University Council on Animal Care
Health Sciences Centre, • London, Ontario • CANADA – N6A 5C1
PH: 519-661-2111 ext. 86768 • FL 519-661-2028
Email: auspc@uwo.ca • http://www.uwo.ca/animal/website/

المنارة للاستشارات
www.manaraa.com

Letters of Permissions

SPRINGER LICENSE
TERMS AND CONDITIONS

Oct 28, 2014

This is a License Agreement between Abraam S Soliman ("You") and Springer ("Springer") provided by Copyright Clearance Center ("CCC"). The license consists of your order details, the terms and conditions provided by Springer, and the payment terms and conditions.

All payments must be made in full to CCC. For payment instructions, please see information listed at the bottom of this form.

License Number	3474340073517
License date	Sep 22, 2014
Licensed content publisher	Springer
Licensed content publication	Springer eBook
Licensed content title	A Convex Relaxation Approach to Fat/Water Separation with Minimum Label Description
Licensed content author	Abraam S. Soliman
Licensed content date	Jan 1, 2012
Type of Use	Thesis/Dissertation
Portion	Full text
Number of copies	1
Author of this Springer article	Yes and you are the sole author of the new work
Order reference number	None
Title of your thesis / dissertation	Acquisition and Reconstruction Techniques for Fat Quantification using Magnetic Resonance Imaging
Expected completion date	Nov 2014
Estimated size(pages)	150
Total	0.00 CAD
Terms and Conditions	

المنارة للاستشارات
www.manaraa.com

Introduction
The publisher for this copyrighted material is Springer Science + Business Media. By clicking "accept" in connection with completing this licensing transaction, you agree that the following terms and conditions apply to this transaction (along with the Billing and Payment terms and conditions established by Copyright Clearance Center, Inc. ("CCC"), at the time that you opened your Rightslink account and that are available at any time athttp://myaccount.copyright.com).

Limited License
With reference to your request to reprint in your thesis material on which Springer Science and Business Media control the copyright, permission is granted, free of charge, for the use indicated in your enquiry.

Licenses are for one-time use only with a maximum distribution equal to the number that you identified in the licensing process.

This License includes use in an electronic form, provided its password protected or on the university's intranet or repository, including UMI (according to the definition at the Sherpa website: http://www.sherpa.ac.uk/romeo/). For any other electronic use, please contact Springer at (permissions.dordrecht@springer.com or permissions.heidelberg@springer.com).

The material can only be used for the purpose of defending your thesis limited to university-use only. If the thesis is going to be published, permission needs to be re-obtained (selecting "book/textbook" as the type of use).

Although Springer holds copyright to the material and is entitled to negotiate on rights, this license is only valid, subject to a courtesy information to the author (address is given with the article/chapter) and provided it concerns original material which does not carry references to other sources (if material in question appears with credit to another source, authorization from that source is required as well).

Permission free of charge on this occasion does not prejudice any rights we might have to charge for reproduction of our copyrighted material in the future.

Altering/Modifying Material: Not Permitted
You may not alter or modify the material in any manner. Abbreviations, additions, deletions and/or any other alterations shall be made only with prior written authorization of the author(s) and/or Springer Science + Business Media. (Please contact Springer at (permissions.dordrecht@springer.com or permissions.heidelberg@springer.com)

Reservation of Rights
Springer Science + Business Media reserves all rights not specifically granted in the combination of (i) the license details provided by you and accepted in the course of this

المنارة للاستشارات
www.manaraa.com

licensing transaction, (ii) these terms and conditions and (iii) CCC's Billing and Payment terms and conditions.

Copyright Notice:Disclaimer
You must include the following copyright and permission notice in connection with any reproduction of the licensed material: "Springer and the original publisher /journal title, volume, year of publication, page, chapter/article title, name(s) of author(s), figure number(s), original copyright notice) is given to the publication in which the material was originally published, by adding; with kind permission from Springer Science and Business Media"

Warranties: None

Example 1: Springer Science + Business Media makes no representations or warranties with respect to the licensed material.

Example 2: Springer Science + Business Media makes no representations or warranties with respect to the licensed material and adopts on its own behalf the limitations and disclaimers established by CCC on its behalf in its Billing and Payment terms and conditions for this licensing transaction.

Indemnity
You hereby indemnify and agree to hold harmless Springer Science + Business Media and CCC, and their respective officers, directors, employees and agents, from and against any and all claims arising out of your use of the licensed material other than as specifically authorized pursuant to this license.

No Transfer of License
This license is personal to you and may not be sublicensed, assigned, or transferred by you to any other person without Springer Science + Business Media's written permission.

No Amendment Except in Writing
This license may not be amended except in a writing signed by both parties (or, in the case of Springer Science + Business Media, by CCC on Springer Science + Business Media's behalf).

Objection to Contrary Terms
Springer Science + Business Media hereby objects to any terms contained in any purchase order, acknowledgment, check endorsement or other writing prepared by you, which terms are inconsistent with these terms and conditions or CCC's Billing and Payment terms and conditions. These terms and conditions, together with CCC's Billing and Payment terms and conditions (which are incorporated herein), comprise the entire agreement between you and Springer Science + Business Media (and CCC) concerning this licensing transaction. In the event of any conflict between your obligations established by these terms and conditions and those established by CCC's Billing and Payment terms and conditions, these terms and

المنارة للاستشارات
www.manaraa.com

conditions shall control.

Jurisdiction
All disputes that may arise in connection with this present License, or the breach thereof, shall be settled exclusively by arbitration, to be held in The Netherlands, in accordance with Dutch law, and to be conducted under the Rules of the 'Netherlands Arbitrage Instituut' (Netherlands Institute of Arbitration).***OR:***

All disputes that may arise in connection with this present License, or the breach thereof, shall be settled exclusively by arbitration, to be held in the Federal Republic of Germany, in accordance with German law.

Other terms and conditions:

v1.3

Questions? customercare@copyright.com or +1-855-239-3415 (toll free in the US) or +1-978-646-2777.

Gratis licenses (referencing $0 in the Total field) are free. Please retain this printable license for your reference. No payment is required.

المنارة للاستشارات
www.manaraa.com

JOHN WILEY AND SONS LICENSE
TERMS AND CONDITIONS

Oct 28, 2014

This is a License Agreement between Abraam S Soliman ("You") and John Wiley and Sons ("John Wiley and Sons") provided by Copyright Clearance Center ("CCC"). The license consists of your order details, the terms and conditions provided by John Wiley and Sons, and the payment terms and conditions.

All payments must be made in full to CCC. For payment instructions, please see information listed at the bottom of this form.

License Number	3474341019199
License date	Sep 22, 2014
Licensed content publisher	John Wiley and Sons
Licensed content publication	Magnetic Resonance in Medicine
Licensed content title	Max-IDEAL: A max-flow based approach for IDEAL water/fat separation
Licensed copyright line	Copyright © 2013 Wiley Periodicals, Inc.
Licensed content author	Abraam S. Soliman,Jing Yuan,Karl K. Vigen,James A. White,Terry M. Peters,Charles A. McKenzie
Licensed content date	Sep 4, 2013
Start page	510
End page	521
Type of use	Dissertation/Thesis
Requestor type	Author of this Wiley article
Format	Print and electronic
Portion	Full article
Will you be translating?	No
Title of your thesis / dissertation	Acquisition and Reconstruction Techniques for Fat Quantification using Magnetic Resonance Imaging
Expected completion date	Nov 2014
Expected size (number of pages)	150
Total	0.00 USD

Terms and Conditions

المنارة للاستشارات

www.manaraa.com

TERMS AND CONDITIONS

This copyrighted material is owned by or exclusively licensed to John Wiley & Sons, Inc. or one of its group companies (each a"Wiley Company") or handled on behalf of a society with which a Wiley Company has exclusive publishing rights in relation to a particular work (collectively "WILEY"). By clicking ﾐaccept ﾐ in connection with completing this licensing transaction, you agree that the following terms and conditions apply to this transaction (along with the billing and payment terms and conditions established by the Copyright Clearance Center Inc., ("CCC's Billing and Payment terms and conditions"), at the time that you opened your Rightslink account (these are available at any time athttp://myaccount.copyright.com).

Terms and Conditions

- The materials you have requested permission to reproduce or reuse (the "Wiley Materials") are protected by copyright.

- You are hereby granted a personal, non-exclusive, non-sub licensable (on a stand-alone basis), non-transferable, worldwide, limited license to reproduce the Wiley Materials for the purpose specified in the licensing process. This license is for a one-time use only and limited to any maximum distribution number specified in the license. The first instance of republication or reuse granted by this licence must be completed within two years of the date of the grant of this licence (although copies prepared before the end date may be distributed thereafter). The Wiley Materials shall not be used in any other manner or for any other purpose, beyond what is granted in the license. Permission is granted subject to an appropriate acknowledgement given to the author, title of the material/book/journal and the publisher. You shall also duplicate the copyright notice that appears in the Wiley publication in your use of the Wiley Material. Permission is also granted on the understanding that nowhere in the text is a previously published source acknowledged for all or part of this Wiley Material. Any third party content is expressly excluded from this permission.

- With respect to the Wiley Materials, all rights are reserved. Except as expressly granted by the terms of the license, no part of the Wiley Materials may be copied, modified, adapted (except for minor reformatting required by the new Publication), translated, reproduced, transferred or distributed, in any form or by any means, and no derivative works may be made based on the Wiley Materials without the prior permission of the respective copyright owner. You may not alter, remove or suppress in any manner any copyright, trademark or other notices displayed by the Wiley Materials. You may not license, rent, sell, loan, lease, pledge, offer as security, transfer or assign the Wiley Materials on a stand-alone basis, or any of the rights granted to you hereunder to any other person.

- The Wiley Materials and all of the intellectual property rights therein shall at all times remain the exclusive property of John Wiley & Sons Inc, the Wiley Companies, or their respective licensors, and your interest therein is only that of having possession of and the right to reproduce the Wiley Materials pursuant to Section 2 herein during the

المنارة للاستشارات

www.manaraa.com

continuance of this Agreement. You agree that you own no right, title or interest in or to the Wiley Materials or any of the intellectual property rights therein. You shall have no rights hereunder other than the license as provided for above in Section 2. No right, license or interest to any trademark, trade name, service mark or other branding ("Marks") of WILEY or its licensors is granted hereunder, and you agree that you shall not assert any such right, license or interest with respect thereto.

- NEITHER WILEY NOR ITS LICENSORS MAKES ANY WARRANTY OR REPRESENTATION OF ANY KIND TO YOU OR ANY THIRD PARTY, EXPRESS, IMPLIED OR STATUTORY, WITH RESPECT TO THE MATERIALS OR THE ACCURACY OF ANY INFORMATION CONTAINED IN THE MATERIALS, INCLUDING, WITHOUT LIMITATION, ANY IMPLIED WARRANTY OF MERCHANTABILITY, ACCURACY, SATISFACTORY QUALITY, FITNESS FOR A PARTICULAR PURPOSE, USABILITY, INTEGRATION OR NON-INFRINGEMENT AND ALL SUCH WARRANTIES ARE HEREBY EXCLUDED BY WILEY AND ITS LICENSORS AND WAIVED BY YOU

- WILEY shall have the right to terminate this Agreement immediately upon breach of this Agreement by you.
- You shall indemnify, defend and hold harmless WILEY, its Licensors and their respective directors, officers, agents and employees, from and against any actual or threatened claims, demands, causes of action or proceedings arising from any breach of this Agreement by you.

- IN NO EVENT SHALL WILEY OR ITS LICENSORS BE LIABLE TO YOU OR ANY OTHER PARTY OR ANY OTHER PERSON OR ENTITY FOR ANY SPECIAL, CONSEQUENTIAL, INCIDENTAL, INDIRECT, EXEMPLARY OR PUNITIVE DAMAGES, HOWEVER CAUSED, ARISING OUT OF OR IN CONNECTION WITH THE DOWNLOADING, PROVISIONING, VIEWING OR USE OF THE MATERIALS REGARDLESS OF THE FORM OF ACTION, WHETHER FOR BREACH OF CONTRACT, BREACH OF WARRANTY, TORT, NEGLIGENCE, INFRINGEMENT OR OTHERWISE (INCLUDING, WITHOUT LIMITATION, DAMAGES BASED ON LOSS OF PROFITS, DATA, FILES, USE, BUSINESS OPPORTUNITY OR CLAIMS OF THIRD PARTIES), AND WHETHER OR NOT THE PARTY HAS BEEN ADVISED OF THE POSSIBILITY OF SUCH DAMAGES. THIS LIMITATION SHALL APPLY NOTWITHSTANDING ANY FAILURE OF ESSENTIAL PURPOSE OF ANY LIMITED REMEDY PROVIDED HEREIN.

- Should any provision of this Agreement be held by a court of competent jurisdiction to be illegal, invalid, or unenforceable, that provision shall be deemed amended to achieve as nearly as possible the same economic effect as the original provision, and the legality, validity and enforceability of the remaining provisions of this Agreement shall not be affected or impaired thereby.

- The failure of either party to enforce any term or condition of this Agreement shall not constitute a waiver of either party's right to enforce each and every term and condition of this Agreement. No breach under this agreement shall be deemed waived or excused by either party unless such waiver or consent is in writing signed by the party granting such waiver or consent. The waiver by or consent of a party to a breach of any provision of this Agreement shall not operate or be construed as a waiver of or consent to any other or subsequent breach by such other party.

المنارة للاستشارات

www.manaraa.com

- This Agreement may not be assigned (including by operation of law or otherwise) by you without WILEY's prior written consent.

- Any fee required for this permission shall be non-refundable after thirty (30) days from receipt by the CCC.

- These terms and conditions together with CCC►s Billing and Payment terms and conditions (which are incorporated herein) form the entire agreement between you and WILEY concerning this licensing transaction and (in the absence of fraud) supersedes all prior agreements and representations of the parties, oral or written. This Agreement may not be amended except in writing signed by both parties. This Agreement shall be binding upon and inure to the benefit of the parties' successors, legal representatives, and authorized assigns.

- In the event of any conflict between your obligations established by these terms and conditions and those established by CCC►s Billing and Payment terms and conditions, these terms and conditions shall prevail.

- WILEY expressly reserves all rights not specifically granted in the combination of (i) the license details provided by you and accepted in the course of this licensing transaction, (ii) these terms and conditions and (iii) CCC►s Billing and Payment terms and conditions.

- This Agreement will be void if the Type of Use, Format, Circulation, or Requestor Type was misrepresented during the licensing process.

- This Agreement shall be governed by and construed in accordance with the laws of the State of New York, USA, without regards to such state►s conflict of law rules. Any legal action, suit or proceeding arising out of or relating to these Terms and Conditions or the breach thereof shall be instituted in a court of competent jurisdiction in New York County in the State of New York in the United States of America and each party hereby consents and submits to the personal jurisdiction of such court, waives any objection to venue in such court and consents to service of process by registered or certified mail, return receipt requested, at the last known address of such party.

WILEY OPEN ACCESS TERMS AND CONDITIONS

Wiley Publishes Open Access Articles in fully Open Access Journals and in Subscription journals offering Online Open. Although most of the fully Open Access journals publish open access articles under the terms of the Creative Commons Attribution (CC BY) License only, the subscription journals and a few of the Open Access Journals offer a choice of Creative Commons Licenses:: Creative Commons Attribution (CC-BY) license Creative Commons Attribution Non-Commercial (CC-BY-NC) license and Creative Commons Attribution Non-Commercial-NoDerivs (CC-BY-NC-ND) License. The license type is clearly identified on the article.

Copyright in any research article in a journal published as Open Access under a Creative Commons License is retained by the author(s). Authors grant Wiley a license to publish the

المنارة للاستشارات

www.manaraa.com

article and identify itself as the original publisher. Authors also grant any third party the right to use the article freely as long as its integrity is maintained and its original authors, citation details and publisher are identified as follows: [Title of Article/Author/Journal Title and Volume/Issue. Copyright (c) [year] [copyright owner as specified in the Journal]. Links to the final article on Wiley's website are encouraged where applicable.

The Creative Commons Attribution License

The Creative Commons Attribution License (CC-BY) allows users to copy, distribute and transmit an article, adapt the article and make commercial use of the article. The CC-BY license permits commercial and non-commercial re-use of an open access article, as long as the author is properly attributed.

The Creative Commons Attribution License does not affect the moral rights of authors, including without limitation the right not to have their work subjected to derogatory treatment. It also does not affect any other rights held by authors or third parties in the article, including without limitation the rights of privacy and publicity. Use of the article must not assert or imply, whether implicitly or explicitly, any connection with, endorsement or sponsorship of such use by the author, publisher or any other party associated with the article.

For any reuse or distribution, users must include the copyright notice and make clear to others that the article is made available under a Creative Commons Attribution license, linking to the relevant Creative Commons web page.

To the fullest extent permitted by applicable law, the article is made available as is and without representation or warranties of any kind whether express, implied, statutory or otherwise and including, without limitation, warranties of title, merchantability, fitness for a particular purpose, non-infringement, absence of defects, accuracy, or the presence or absence of errors.

Creative Commons Attribution Non-Commercial License

The Creative Commons Attribution Non-Commercial (CC-BY-NC) License permits use, distribution and reproduction in any medium, provided the original work is properly cited and is not used for commercial purposes.(see below)

Creative Commons Attribution-Non-Commercial-NoDerivs License

The Creative Commons Attribution Non-Commercial-NoDerivs License (CC-BY-NC-ND) permits use, distribution and reproduction in any medium, provided the original work is properly cited, is not used for commercial purposes and no modifications or adaptations are made. (see below)

Use by non-commercial users

المنارة للاستشارات

www.manaraa.com

For non-commercial and non-promotional purposes, individual users may access, download, copy, display and redistribute to colleagues Wiley Open Access articles, as well as adapt, translate, text- and data-mine the content subject to the following conditions:

- The authors' moral rights are not compromised. These rights include the right of "paternity" (also known as "attribution" - the right for the author to be identified as such) and "integrity" (the right for the author not to have the work altered in such a way that the author's reputation or integrity may be impugned).

- Where content in the article is identified as belonging to a third party, it is the obligation of the user to ensure that any reuse complies with the copyright policies of the owner of that content.

- If article content is copied, downloaded or otherwise reused for non-commercial research and education purposes, a link to the appropriate bibliographic citation (authors, journal, article title, volume, issue, page numbers, DOI and the link to the definitive published version on **Wiley Online Library**) should be maintained. Copyright notices and disclaimers must not be deleted.

- Any translations, for which a prior translation agreement with Wiley has not been agreed, must prominently display the statement: "This is an unofficial translation of an article that appeared in a Wiley publication. The publisher has not endorsed this translation."

Use by commercial "for-profit" organisations

Use of Wiley Open Access articles for commercial, promotional, or marketing purposes requires further explicit permission from Wiley and will be subject to a fee. Commercial purposes include:

- Copying or downloading of articles, or linking to such articles for further redistribution, sale or licensing;

- Copying, downloading or posting by a site or service that incorporates advertising with such content;

- The inclusion or incorporation of article content in other works or services (other than normal quotations with an appropriate citation) that is then available for sale or licensing, for a fee (for example, a compilation produced for marketing purposes, inclusion in a sales pack)

- Use of article content (other than normal quotations with appropriate citation) by for-profit organisations for promotional purposes

- Linking to article content in e-mails redistributed for promotional, marketing or educational purposes;

- Use for the purposes of monetary reward by means of sale, resale, licence, loan, transfer

المنارة للاستشارات

www.manaraa.com

or other form of commercial exploitation such as marketing products

- Print reprints of Wiley Open Access articles can be purchased from:corporatesales@wiley.com

Further details can be found on Wiley Online Libraryhttp://olabout.wiley.com/WileyCDA/Section/id-410895.html

Other Terms and Conditions:

v1.9

Questions? customercare@copyright.com or +1-855-239-3415 (toll free in the US) or +1-978-646-2777.

Gratis licenses (referencing $0 in the Total field) are free. Please retain this printable license for your reference. No payment is required.

المنارة للاستشارات

www.manaraa.com

Curriculum Vitae

Name:	Abraam Soliman
Post-secondary Education and Degrees:	2003 – 2008 **B.Sc.** Cairo University Cairo, Egypt 2008 – 2010 **M.Sc.** Nile University Cairo, Egypt 2010 – 2014 **PhD** The University of Western Ontario London, ON, Canada
Honors, Awards, and Scholarships	NSERC Computer-Assisted Medical Intervention (CAMI) Training Program, The University of Western Ontario 2012 – 2014 CIHR Strategic Training Program in Vascular Research, The University of Western Ontario 2010 – 2012 Western Graduate Research Scholarship, The University of Western Ontario 2010 – 2014 Graduate Fellowship School of Communications and Information Technology, Nile University, Egypt 2008 – 2010 ISMRM Educational Stipend 2012, 2013, 2014 Nominated for "Best Graduate Student Teaching" Award The University of Western Ontario 2012

المنارة للاستشارات
www.manaraa.com

Third Best Poster,
ISMRM Workshop on Fat-Water Separation
2012

Honor Award
Faculty of Engineering, Cairo University, Egypt
2008

"Academic Outstanding" Award,
Faculty of Engineering, Cairo University, Egypt
2004 – 2008

Related Work Experience

Teaching Assistant
The University of Western Ontario
2010 – 2014

Mentoring a senior year Medical Biophysics student
The University of Western Ontario
2013

Hospital Intern
Cairo, Egypt
2005, 2006

Patents (in preparation)

An Efficient Interleaved Bipolar Magnetic Resonance Imaging Acquisition of Chemical Species

Invited Talks

Medical Image Analysis (MedIA) seminar series
Robarts Research Institute, London, ON
2013

Poster Presentations:

1. **Soliman AS**, Wiens CN, Wade T, Shimakawa A, Peters TM, McKenzie CA, "*Fat Quantification with an Interleaved Bipolar Acquisition*", 22nd ISMRM Annual Meeting, Milan, Italy, 1673 (2014)

2. **Soliman AS**, Wiens CN, Wade T, Shimakawa A, Peters TM, McKenzie CA, "*Chemical-Shift Imaging with an Interleaved Bipolar Acquisition*", Imaging Network Ontario Symp. (2014)

المنارة للاستشارات
www.manaraa.com

3. **Soliman AS**, Wiens CN, Wade T, Shimakawa A, Peters TM, McKenzie CA, "*Chemical-Shift Imaging with an Interleaved Bipolar Acquisition*", London Health Research Day (2014)

4. **Soliman AS**, Wiens CN, Wade T, Shimakawa A, Peters TM, McKenzie CA, "*Chemical-Shift Imaging with an Interleaved Bipolar Acquisition*", London Imaging Discovery Day (2014)

5. **Soliman AS**, Yuan J, Peters TM, McKenzie CA, "*3D Mapping of T2* and B0 Inhomogeneities for Water/Fat Separation*", 21st ISMRM Annual Meeting, Salt Lake City, USA (2013)

6. **Soliman AS**, Yuan J, Peters TM, McKenzie CA, "*Validation of a Convex Relaxation Approach for Field Map Estimation*", 21st ISMRM Annual Meeting, Salt Lake City, USA (2013)

7. **Soliman AS**, Yuan J, Vigen K, White JA, Peters TM and McKenzie CA, "*Robust Field Map Estimation using VARPRO and Multi-labeling Continuous Max-Flow*", 20th ISMRM Annual Meeting, Melbourne, Australia (2012)

8. **Soliman AS**, Yuan J, Vigen K, White JA, Peters TM and McKenzie CA, "*Fast Field Map Estimation with Multi-labeling Continuous Max-Flow*", ISMRM Workshop on Fat-Water Separation, Longbeach, CA (2012)

9. **Soliman AS**, Yuan J, Vigen K, White JA, Peters TM and McKenzie CA, "*Fast Water/Fat Separation for Cardiac Imaging*", Imaging Network Ontario Symp. (2012)

10. **Soliman AS**, Kerwin WS, Osman NF, "*MR Harmonic Phase Surface for Tracking Cardiac Motion*" 13th Annual SCMR Scientific Session, (2010)

11. **Soliman AS**, Osman NF, "*3D Motion Tracking of the Heart Using Harmonic Phase (HARP) Isosurfaces*", SPIE, San Diego, CA (2010)

Publications: Peer-reviewed Articles:

1. **Soliman AS**, Friesen-Waldner LJ, Sinclair KJ, Regnault TRH, Peters TM, and McKenzie CA. "*An Efficient Chemical-shift Encoded Acquisition for in-vivo Applications*", Journal of Magnetic Resonance Imaging (in preparation).

المنارة للاستشارات
www.manaraa.com

2. **Soliman AS**, Wiens CN, Wade T, Peters TM, McKenzie CA, "*Fat Quantification using an Interleaved Bipolar Acquisition*", completed for submission to Magnetic Resonance in Medicine.

3. **Soliman AS**, Yuan J, Vigen KK, White JA, Peters TM, McKenzieCA, "Max-IDEAL: A Max-Flow Based Approach for IDEAL Water/Fat Separation", Magnetic Resonance in Medicine, 2014; 72 (2): 510-521.

4. Addeman BT, Kutty S, Perkins TG, **Soliman AS**, Wiens CN, Mc-Curdy CM, Beaton MD, Hegele RA, McKenzie CA, "*Validation of Volumetric and Single Slice MRI Adipose analysis using a novel Fully Automated Segmentation method*", J Magnetic Resonance Imaging, 2013 (in press) DOI: 10.1002/jmri.24526

5. Jolly U, **Soliman AS**, McKenzie C, Peters TM, Stirrat J, Brymer M, Joy T, Drangova M, White A, "*Intra-Thoracic Fat Volume is Associated with Myocardial Infarction in Patients With Metabolic Syndrome*", J of Cardiovascular Magnetic Resonance, 2013; 15:77

6. **Soliman AS**, Yuan J, White JA, Peters TM and McKenzie CA, "*A Convex Relaxation Approach to Fat/Water Separation with Minimum Label Description*", LNCS 7511 - Medical Image Computing and Computer-Assisted Intervention (MICCAI), 2012; 519-526

Conference Proceedings:

1. **Soliman AS**, Wiens CN, Wade T, Shimakawa A, Peters TM, McKenzie CA, "*Fat Quantification with an Interleaved Bipolar Acquisition*", Proc. 22nd ISMRM, Milan, Italy, 1673 (2014)

2. McCurdy CM, Addeman BT, Wiens CN, Friesen-Waldner LJ, Wade TP, Harris JK, **Soliman AS**, Sinclair KJ, McKenzie CA, "*Automated Volumetric Fat Quantification of Adipose Tissue in Mice*", Proc. 22nd ISMRM, Milan, Italy, 2145 (2014)

3. **Soliman AS**, Wiens CN, Wade T, Shimakawa A, Peters TM, McKenzie CA, "*Chemical-Shift Imaging with an Interleaved Bipolar Acquisition*", Imaging Network Ontario Symp. (2014)

4. **Soliman AS**, Wiens CN, Wade T, Shimakawa A, Peters TM, McKenzie CA, "*Chemical-Shift Imaging with an Interleaved Bipolar Acquisition*", London Health Research Day (2014)

المنارة للاستشارات
www.manaraa.com

5. **Soliman AS**, Wiens CN, Wade T, Shimakawa A, Peters TM, McKenzie CA, "*Chemical-Shift Imaging with an Interleaved Bipolar Acquisition*", London Imaging Discovery Day (2014)

6. McCurdy CM, Addeman BT, Wiens CN, Friesen-Waldner LJ, Wade TP, Harris JK, **Soliman AS**, Sinclair KJ, McKenzie CA, "*Automated Volumetric Fat Quantification of Adipose Tissue in Mice*", Imaging Network Ontario Symp. (2014)

7. McCurdy CM, Addeman BT, Wiens CN, Friesen-Waldner LJ, Wade TP, Harris JK, **Soliman AS**, Sinclair KJ, McKenzie CA, "*Automated Volumetric Fat Quantification of Adipose Tissue in Mice*", London Health Research Day (2014)

8. **Soliman AS**, Yuan J, Peters TM, McKenzie CA, "*3D Mapping of T2* and B0 Inhomogeneities for Water/Fat Separation*", Proc. 21st ISMRM, Salt Lake City, USA, 4277 (2013)

9. **Soliman AS**, Yuan J, Peters TM, McKenzie CA, "*Validation of a Convex Relaxation Approach for Field Map Estimation*", Proc. 21st ISMRM, Salt Lake City, USA, 2418 (2013)

10. McCurdy CM, Addeman BT, Wiens CN, Friesen-Waldner LJ, Wade TP, Harris JK, **Soliman AS**, Sinclair KJ, McKenzie CA, "*Interscapular Brown Adipose Tissue and Adipose Distribution in Magnetic Resonance Images of Mice*", NIH workshop on Exploring the Role of Brown Fat in Humans, Bethesda, MD (2013)

11. **Soliman AS**, Yuan J, Vigen K, White JA, Peters TM and McKenzie CA, "*Robust Field Map Estimation using VARPRO and Multi-labeling Continuous Max-Flow*", Proc. 20th ISMRM, Melbourne, Australia, 2508 (2012)

12. Addeman BT, Beaton M, Hegele RA, **Soliman AS**, Wiens CN and McKenzie CA, "*Validation of Fully Automatic Adipose Tissue Segmentation and Volume Quantifica*tion", Proc. 20th ISMRM, Melbourne, Australia, 751 (2012)

13. Addeman BT, **Soliman AS**, Wiens CN and McKenzie CA, "*Volumetric Fat Quantification of Intra-Abdominal Adipose Tissue from a Single Breath Hold Acquisition*", Proc. 20th ISMRM, Melbourne, Australia, 4172 (2012)

14. Cui Y, Yang IY, Wade T, Wiens CN, **Soliman AS**, and McKenzie CA, "*Absolute Quantification of In Vivo Water and Fat Content*",

المنارة للاستشارات
www.manaraa.com

Proc. 20th Annual Meeting of ISMRM, Melbourne, Australia, 363 (2012)

15. **Soliman AS**, Yuan J, Vigen K, White JA, Peters TM and McKenzie CA, "*Fast Field Map Estimation with Multi-labeling Continuous Max-Flow*", ISMRM Workshop on Fat-Water Separation, Longbeach, CA (2012)

16. **Soliman AS**, Yuan J, Vigen K, White JA, Peters TM and McKenzie CA, "*Fast Water/Fat Separation for Cardiac Imaging*", Imaging Network Ontario Symp. (2012)

17. Addeman BT, Beaton M, Hegele RA, **Soliman AS**, Wiens CN and McKenzie CA, "*Validation of Fully Automatic Adipose Tissue Segmentation and Volume Quantific*ation", ISMRM Workshop on Fat-Water Separation, Longbeach, CA (2012)

18. Cui Y, Yang IY, Wade T, Wiens CN, **Soliman AS** and McKenzie CA, "*Absolute Quantification of In Vivo Water and Fat Content*", ISMRM Workshop on Fat-Water Separation, Longbeach, CA (2012)

19. Addeman BT, **Soliman AS**, Wiens CN and McKenzie CA, "*Volumetric Fat Quantification of Intra-Abdominal Adipose Tissue from a Single Breath Hold Acquisition*", ISMRM Workshop on Fat-Water Separation, Longbeach, CA (2012)

20. **Soliman AS**, Kerwin WS, Osman NF, "*MR Harmonic Phase Surface for Tracking Cardiac Motion*" Journal of Cardiovascular Magnetic Resonance, 12(Suppl 1):P245 (2010)

21. **Soliman AS**, Osman NF, "*3D Motion Tracking of the Heart Using Harmonic Phase (HARP) Isosurfaces*", Proc. SPIE 7623, 76232C (2010)

المنارة للاستشارات

www.manaraa.com